MECHANISM OF PROTEIN AGGREGATION LEADING TO AMYLOID FORMATION

BY XIANGLAN HE

A dissertation submitted to the

Graduate School—New Brunswick

Rutgers, The State University of New Jersey

In partial fulfillment of the requirements

For the degree of

Doctor of Philosophy

Graduate Program in Chemistry and Chemical Biology

Written under the direction of

David S. Talaga

And approved by

_____

_____

_____

_____

New Brunswick, New Jersey

January, 2012

ABSTRACT OF THE DISSERTATION

Mechanism of Protein Aggregation Leading to Amyloid Formation

by Xianglan He

Dissertation Director: David S. Talaga

Amyloid deposition has been observed in more than 20 diseases. Each amyloid-related disease has a particular precursor protein or peptide that converts from its native state to insoluble cross-β amyloid assemblies. Understanding the amyloid aggregation mechanism is the basis for development of a rational strategy for preventing the aggregation cascade events. This dissertation contributes to the elucidation of amyloid aggregation mechanism by characterizing the aggregation intermediates with complementary biophysical techniques and clarifying the fluorescence mechanism of a standard amyloid probe, thioflavin T (ThT).

In the first part of this dissertation, aggregation state distribution was determined at single-molecule level with atomic force microscopy (AFM), by development of a particle size analysis package for AFM images. Combining the aggregation state distribution from AFM and dynamic light scattering (DLS) measurements, a quantitative reservoir-nucleation model for β-lactoglobulin A (β-LGA) amyloid formation was proposed based on kinetic simulation. The model successfully predicted the results of 1-anilino-8-naphthalene sulfonate (ANS) fluorescence and seeding experiments. An aggregation free-energy landscape was constructed based on the simulation. A classification scheme for oligomeric species was proposed to evaluate their roles during

aggregation, based on their locations on the aggregation free-energy landscape. Different types of oligomers were related to the amyloid cascade hypothesis and the toxic oligomer hypothesis for amyloid-related diseases.

The second part of this dissertation focuses on fluorescence mechanism of ThT, which is a standard tool for amyloid fibril detection and aggregation kinetic studies. DLS was used to probe the aggregation state of ThT in solutions of different conditions. The micelle model was disproved by showing the absence of ThT micelles in solution. The exciton model was disproved by fit of the concentration dependence of ThT fluorescence intensity to a fluorescent monomer model. Enhanced quantum yield was observed for surface-bound ThT in both bulk and single-molecule fluorescence measurements, with substantial shift in the excitation spectra, compared with fibril-bound ThT. The presence of surface-bound ThT fluorescence calls for re-evaluation of reported ThT photophysical properties in solutions of low viscosity, which are likely dominated by the surface effect. Similar lifetime features were observed for surface-bound and fibril-bound ThT. These results revealed that ThT bound to amyloid fibrils rigidly as it bound to the surface. Interaction of ThT with α-Synuclein (αSyn) fibrils was studied with single-molecule fluorescence microscopy. The single-molecule fluorescence polarization images showed that ThT bound to αSyn fibrils with its long axis parallel to the fibril axis.

List of Figures

List of Tables

Dedication

To my family, who have given me a life rich with opportunities.

Table of Contents

Chapter 1

Introduction

1.1 Overview

Amyloidosis is a group of conditions, which have various clinic features but share the common feature of excessive amyloid fibril deposits in patients.[1,2,3,4] Amyloid fibrils are protein aggregates defined by following characteristics: low solubility in aqueous buffers; unbranched and fibrillar structure observed with electron microscopy (EM) and atomic force microscopy (AFM); observed apple-green birefringence with Congo Red (CR) stain; extended cross-β sheet X-ray diffraction pattern.[5,4,6] Each amyloidosis is associated with particular protein or protein fragment precursors and has its own pattern of deposition. By 2010, 27 extracellular amyloid fibrils with specific precursor proteins and 8 intracellular inclusions with amyloid-like properties had been identified in human amyloidoses.[7] Take the most frequent type of amyloidosis, Alzheimer's disease (AD) as an example, deposition of extracellular and intracellular fibrils of Amyloid-β (Aβ) protein, and intracellular neurofibrillary tangles of Tau protein are hallmarks of this condition.[8,9] Despite the structure and property similarity of all amyloid fibrils, precursors for naturally occurred amyloid fibrils share no identified structural or chemical similarity.

In all amyloidosis, the normal precursor protein or protein fragment changes its structure and begins to aggregate, and they aggregate in a special way to form amyloid fibrils. This aggregation is generally depicted as a nucleation-dependent process. In nucleation-dependent aggregations, the nucleus has the highest free energy among all species. The aggregation is energetically unfavorable before the nucleus formation, and becomes favorable once the nucleus is formed. This energy barrier for nucleus formation results in a lag phase preceding the fast growth phase in the kinetic profile,

which appears in all amyloid aggregation studies. Addition of seeds into the incubation can remove this energy barrier and thus eliminate the lag phase.[10,11] Deposition of amyloid fibrils is the hallmark for amyloidosis, but fibrils are not necessarily the primary causative factor in these diseases.[4,12,13] Species of various aggregation and structural states are formed during the conversion of precursors to amyloid fibrils. While massive deposition of amyloid plaques can interfere with normal organ functions, this multi-step conversion process can be destructive in many other ways, such as as depletion of normally functional proteins and production of toxic intermediates.[14,15,16,17,18] This dissertation focuses on the characterization of small oligomeric species formed during the pre-nucleation steps. From a disease point of view, measures should be taken before the nucleus formation and drugs should be designed to target the pre-nucleation species. Mechanistically, pre-nucleation reactions are the rate-limiting steps and the influence of solution conditions and mutations are of most importance on these steps.

The conversion of precursors to amyloid fibrils in amyloidosis can be induced *in vitro*, such as α-Synuclein (αSyn) in Parkinson's disease.[19] This conversion has also been shown for many other proteins that are not disease-related. For example, bovine β-lactoglobulin A (β-LGA), which is a main component of the whey of cow's milk and is not implicated in any amyloidosis, has been shown to form amyloid fibrils under partially denaturing conditions *in vitro*.[20,21,22,23,24,25] *In vitro* studies isolate the highly heterogeneous aggregation process from extraordinary complexity encountered in *in vivo* studies, and enable the use of a variety of biophysical techniques. This dissertation contributes to the elucidation of *in vitro* amyloid aggregation mechanism in the following aspects: 1) an AFM image analysis approach was developed to characterize aggregation state distribution during amyloid aggregation. 2) A molecular kinetic model for amyloid aggregation was constructed based on characterization of intermediates with complementary biophysical techniques. 3) A free-energy landscape was constructed as an approach to simplify multi-step, multi-species aggregation mechanism. Based on their kinetic behavior and their relationships on the free-energy landscape, a classification system was introduced for oligomers, which related the kinetic behavior of oligomers with their roles in amyloidosis pathology. 4) Single-molecule microscopy technique was

introduced as an approach to synchronous detection of aggregation and structural states during amyloid aggregation. 5) Rigid-binding was determined to be essential for amyloid probe Thioflavin T (ThT) fluorescence mechanism. ThT was shown to bind to fibrils with its long structure axis parallel to the fibril axis. 6) Hydrophobic-hydrophilic interface was identified as the major driving force for agitated αSyn aggregation *in vitro*.

1.2 Complex Amyloid Aggregation Process Requires Characterization with Multiple Biophysical Techniques

Characterization of aggregation and structural states of intermediate species in amyloid aggregation is the foundation for a molecular aggregation model. It is not a trivial task to cover the wide size and structure variety in amyloid aggregation. No single technique can handle this heterogeneity and most techniques bias toward large fibril detection.[26] The solution is to use multiple and complementary techniques to characterize the system. This approach was demonstrated with β-LGA amyloid aggregation in Chapter 2. The structure and stability of β-LGA has been well characterized.[27] It contains a 8-stranded β-barrel ligand-binding calyx, in which small fluorescence probe 1-anilino-8-naphthalene sulfonate (ANS) can bind. During amyloid aggregation, this calyx was disrupted and this process was monitored with time-resolved ANS fluorescence.

In Chapter 2, dynamic light scattering (DLS), AFM, time-resolved ANS and ThT fluorescence were used to monitor amyloid aggregation of β-LGA. The evolution of signal patterns in these techniques reflected four sequential stages experienced by the system. During the early lag phase, loosely associated aggregates, AggA, were formed. DLS showed population evolution of AggA, while AFM only captured amorphous, denatured protein layer on the substrate surface. Time-resolved ANS fluorescence indicated that the calyx was partially disrupted. During the late lag phase, AggA converted to a new class of oligomers, AggB. At this stage, further particle size increase was detected by DLS. AFM images captured globular AggB oligomers of different sizes, with well-defined features. Complete disruption of the calyx was detected by time-resolved ANS

fluorescence. The early growth phase started when AggB grew into short protofibrils, as the basic fibrillar unit of amyloid. At this stage, the increased heterogeneity of particle size and morphology prevented the resolution of species by DLS measurement. On the other hand, AFM images detected individual protofibrils, coexisting with globular particles. ThT fluorescence experienced fast increase at this stage, with distinctive lifetime pattern. The system reached late growth phase when the protofibrils finally dominated the population. A strong lifetime feature, which was quite different than that of mature amyloid fibrils, dominated the ThT signal at this stage. As we can see, the observation of these four stages could only be achieved by combining results from all these techniques.

1.3 Innovative Application of Atomic Force Microscopy in Particle Size Determination

AFM has been widely used in amyloid assembly studies to verify the fibrillar morphology of final amyloid products. Besides amyloid fibrils, small particles of various morphologies are also captured by AFM. However, this capability of AFM for oligomer detection is ignored in amyloid aggregation studies. As a single-molecule technique, AFM has unexploited advantages over many other particle sizing techniques. With other techniques, such as DLS, particle size distribution is usually resolved from an averaged signal and the data analysis suffers from increased size and morphology heterogeneity of the system.[24] On the other hand, AFM detects a great number of particles of different sizes and morphologies in one measurement. The number of particles can be counted and the particle population distribution can thus be statistically determined.

However, while the height of particles can be precisely determined, convolution of particle lateral dimensions with the AFM tip makes the size measurement less straightforward. This results in the general underestimation of AFM as a particle sizing technique. In this dissertation, an AFM image analysis package was developed to explore the particle sizing capability of AFM. Using this package, individual particles in AFM images can be automatically identified, measured, classified, and counted to establish

the particle size distribution. This technique was used to characterize the aggregation state of intermediates in β-LGA amyloid aggregation in Chapter 2.

1.4 Kinetic Simulation and Free-energy Landscape

Guided by the experimentally established qualitative model, a quantitative model was constructed for β-LGA amyloid aggregation through kinetic simulation. Unlike other kinetic simulations for amyloid aggregation, the kinetic simulation in Chapter 2 was directly based on the experimentally characterized intermediates, not averaged signals. Reaction pathways and corresponding rate coefficients were determined by fitting the intermediates population evolution obtained with DLS and AFM. The model successfully predicted the results from ANS fluorescence lifetime measurement and the seeded kinetic profile in seeding experiments. An aggregation energy landscape was constructed to summarize the aggregation pathway and energetics, in which the relative energy was calculated based on forward and reverse rate coefficients. Based on their locations on the energy landscape, four types of oligomers were identified. The nucleating oligomers have the highest free energy along the amyloid aggregation pathway. Before formation of nucleating oligomers, some oligomers sit in a free-energy valley, and are called reservoir species. Energetically favorable aggregation after nucleation leads to seeding oligomers. The dead-end oligomers are small population of species out of the amyloid aggregation pathway. The energy landscape predicted the presence of a reservoir, creating a population of stable mis-folded oligomers. Accumulation of these mis-folded oligomers can cause toxicity in amyloidosis. A detailed discussion on how an energy landscape can guide our thinking on amyloid aggregation problems can be found in Chapter 2.

1.5 Fluorescence Mechanism of Thioflavin T upon Binding to Amyloid Fibrils

ThT fluorescence is the most popular and important biophysical technique used in amyloid aggregation studies.[28] ThT was first used in 1959 as a histological stain to show

amyloid deposits in tissue sections.[29] Upon binding to amyloid fibrils, ThT experiences a dramatic increase in quantum yield. In spite of the difference in chemical compositions, amyloid fibrils induce ThT fluorescence with excitation maximum around 445 nm and emission maximum around 480 nm, with limited shifts.[30,31] Compared with other molecular probes used to study amyloid aggregation, ThT has the advantage of not interfering with the fibrillization process in most cases. It is thus convenient to monitor fibrillization kinetics with ThT fluorescence, and to evaluate how different factors affect the fibrillization kinetics.

When time-resolved ThT fluorescence measurement was taken during the β-LGA amyloid aggregation, fluorescence signal was not only observed for fibrils, but also during stages before fibril formation, with much lower intensity. Specific lifetime pattern was observed at each aggregation stage. Different species at different stages interacted differently with ThT, and resulted in different lifetimes, which could be used to distinguish different species.[24] To assign the lifetime features to specific species, two types of single-molecule fluorescence microscopy measurements, lifetime imaging and photobleaching, were combined to achieve synchronous determination of structural and aggregation states. In this method, the fluorophore was used as a structural state reporter and an aggregation state reporter at the same time. Single-molecule lifetime imaging measurement can resolve the structural hereterogenity present from species to species, and even inside the species. Single-molecule photobleaching measurement can characterize the aggregation state of species, determining the number of monomers in each aggregates.[32] The interaction of ThT with αSyn amyloid fibrils was studied with this method in Chapter 3. ThT-stained fibrils were imaged with enhanced intensity against the low-fluorescent background. No photobleaching steps could be resolved from the intensity trajectory, suggesting that ThT was not a proper dye for photobleaching counting experiment. Even so, the setups, protocols and the evaluation of observations discussed in Chapter 3 provide a general framework for application of single-molecule fluorescence microscopy in amyloid aggregation studies. Another important observation was that ThT bound to the coverslip surface with the same lifetime features as fibril-bound ThT, but with much lower intensity.

Clarification of the ThT fluorescence mechanism is essential for the interpretation of fluorescence data, and development of new molecular probes for amyloid aggregation studies.[28,33] Despite its popularity, the mechanism of characteristic ThT fluorescence is still not clear. No structure model at molecular level has been determined for amyloid fibrils, not to mention a molecular model for ThT binding. The following aspects of ThT fluorescence mechanism were clarified in Chapter 4. First, what is the molecular form of fluorescent ThT: monomer, dimer or micelle? The ThT micelle model was refuted by showing absence of nanometer sized particles in ThT solutions under different conditions, monitored with DLS. Concentration dependence of ThT fluorescence was determined by titrating ThT into amyloid fibrils. Fit of the titration curve supported ThT monomers as the fluorescent species and negated the dimer model. Second, rigid-binding was determined to be essential for ThT quantum yield increase. Dramatic enhancement in ThT quantum yield was observed for surface-bound ThT, but with different spectral maxima than fibril-bound ThT. In many studies, spectral properties of surface-bound ThT were mistaken as signals from solution-phase ThT, for solutions of low viscosity. This lead to misinterpretation of ThT fluorescence mechanism.[31,34] The discrepancy between ThT absorption and excitation maximum in many solutions was thus determined to be an artifact caused by surface-bound ThT. This finding called for re-evaluation of spectral shifts of ThT reported for different solutions. Third, ThT was found to be held rigidly on αSyn amyloid fibrils with its structural long axis parallel to the fibril axis, as indicated by single-molecule fluorescence polarization imaging.

1.6 Acceleration of α-Synuclein Amyloid Aggregation by Hydrophobic-water Interfaces

αSyn is the major component of amyloid fibrils found in Parkinson's disease, and its aggregation mechanism is under intensive study.[3,4] Through *in vitro* incubation, αSyn can form amyloid fibrils, which resemble those found in Parkinson's disease. Typical nucleation-dependent kinetics were observed for this process, as in all amyloid aggregations.[35] However, the reported lag times varied from several hour to several months.

Through literature review, agitation was identified as the major factor among incubation conditions that caused this inconsistency: whether the incubation was performed with or without agitation, the way of agitation, and the speed of the agitation. Amyloidogenic αSyn incubations were made with careful control over the agitation factor, and monitored with steady-state ThT fluorescence and AFM in Chapter 5. Polytetrafluoroethylene (PTFE) balls were added to air-free samples to replace the uncontrollable air-water interface during agitation with quantifiable PTFE-water interface. Refuting the widely accepted mixing and/or fibril fragmentation model, this study identified hydrophobic-hydrophilic interface as the major driving force for αSyn amyloid aggregation with agitation.

Bibliography

[1] M. B. Pepys. Pathogenesis, diagnosis and treatment of systemic amyloidosis. *Philos. Trans. R. Soc. Ser. B*, 356:203–211, 2001.

[2] M. Stefani. Protein misfolding and aggregation: new examples in medicine and biology of the dark side of the protein world. *Biochim. Biophys. Acta.*, 1739(1):5–25, 2004.

[3] M. B. Pepys. Amyloidosis. *Annu. Rev. Med.*, 57:223–241, 2006.

[4] F. Chiti and C. M. Dobson. Protein misfolding, functional amyloid, and human disease. *Annu. Rev. Biochem.*, 75:333–366, 2006.

[5] S. Ohnishi and K. Takano. Amyloid fibrils from the viewpoint of protein folding. *Cell Mol. Life Sci.*, 61(5):511–524, 2004.

[6] M. Fndrich. On the structural definition of amyloid fibrils and other polypeptide aggregates. *Cell Mol. Life Sci.*, 64(16):2066–2078, 2007.

[7] J. D. Sipe, M. D. Benson, J. N. Buxbaum, S. Ikeda, G. Merlini, M. J. M. Saraiva, and P. Westermark. Amyloid fibril protein nomenclature: 2010 recommendations from the nomenclature committee of the International Society of Amyloidosis. *Amyloid*, 17(3-4):101–104, 2010.

[8] R. E. Tanzi and L. Bertram. Twenty years of the Alzheimer's disease amyloid hypothesis: a genetic perspective. *Cell*, 120(4):545–555, 2005.

[9] F. M. LaFerla, K. N. Green, and S. Oddo. Intracellular amyloid-β in Alzheimer's disease. *Nat. Rev. Neurosci.*, 8(7):499–509, 2007.

[10] J. T. Jarrett and P. T. J. Lansbury. Seeding "one-dimensional crystallization" of amyloid: A pathogenic mechanism in Alzheimer's disease and scrapie? *Cell*, 73:1055–1058, 1993.

[11] I. V. Baskakov and O. V. Bocharova. In vitro conversion of mammalian prion protein into amyloid fibrils displays unusual features. *Biochemistry*, 44(7):2339–2348, 2005.

[12] J. C. Dodart, K. R. Bales, K. S. Gannon, S. J. Greene, R. B. DeMattos, C. Mathis, C. A. DeLong, S. Wu, X. Wu, D. M. Holtzman, and S. M. Paul. Immunization reverses memory deficits without reducing brain Aβ burden in Alzheimer's disease model. *Nat. Neurosci.*, 5(5):452–457, 2002.

[13] J. J. Meier, R. Kayed, C. Lin, T. Gurlo, L. Haataja, S. Jayasinghe, R. Langen, C. G. Glabe, and P. C. Butler. Inhibition of human IAPP fibril formation does not prevent β-cell death: evidence for distinct actions of oligomers and fibrils of human IAPP. *Am. J. Physiol. Endocrinol. Metab.*, 291(6):E1317–E1324, 2006.

[14] B. Caughey and P. T. Lansbury. Protofibrils, pores, fibrils, and neurodegeneration: separating the responsible protein aggregates from the innocent bystanders. *Annu. Rev. Neurosci.*, 26:267–298, 2003.

[15] A. Demuro, E. Mina, R. Kayed, S. C. Milton, I. Parker, and C. G. Glabe. Calcium dysregulation and membrane disruption as a ubiquitous neurotoxic mechanism of soluble amyloid oligomers. *J. Biol. Chem.*, 280(17):17294–17300, 2005.

[16] S. T. Ferreira, M. N. N. Vieira, and F. G. D. Felice. Soluble protein oligomers as emerging toxins in Alzheimer's and other amyloid diseases. *IUBMB Life*, 59(4-5):332–345, 2007.

[17] J. Laurn, D. A. Gimbel, H. B. Nygaard, J. W. Gilbert, and S. M. Strittmatter. Cellular prion protein mediates impairment of synaptic plasticity by amyloid-β oligomers. *Nature*, 457(7233):1128–1132, 2009.

[18] M. Stefani. Protein aggregation diseases: toxicity of soluble prefibrillar aggregates and their clinical significance. *Methods. Mol. Biol.*, 648:25–41, 2010.

[19] J. Pronchik, X. He, J. T. Giurleo, and D. S. Talaga. In vitro formation of amyloid from α-synuclein is dominated by reactions at hydrophobic interfaces. *J. Am. Chem. Soc.*, 132:9797–9803, 2010.

[20] R. Carrotta, R. Bauer, R. Waninge, and C. Rischel. Conformational characterization of oligomeric intermediates and aggregates in β-lactoglobulin heat aggregation. *Protein Sci.*, 10(7):1312–1318, 2001.

[21] D. Hamada and C. M. Dobson. A kinetic study of β-lactoglobulin amyloid fibril formation promoted by urea. *Protein Sci.*, 11:2417–2426, 2002.

[22] W. S. Gosal, A. H. Clark, and S. B. Ross-Murphy. Fibrillar β-lactoglobulin Gels: part 1. fibril formation and structure. *Biomacromolecules*, 5:2408–2419, 2004.

[23] L. M. C. Sagis, C. Veerman, and E. Linden. Mesoscopic properties of semiflexible amyloid fibrils. *Langmuir*, 20(3):924–927, 2004.

[24] J. T. Giurleo, X. He, and D. S. Talaga. β-Lactoglobulin assembles into amyloid through sequential aggregated intermediates. *J. Mol. Biol.*, 381:1332–1348, 2008.

[25] D. Hamada, T. Tanaka, G. G. Tartaglia, A. Pawar, M. Vendruscolo, M. Kawamura, A. Tamura, N. Tanaka, and C. M. Dobson. Competition between folding, native-state dimerisation and amyloid aggregation in β-lactoglobulin. *J. Mol. Biol.*, 386(3):878–890, 2009.

[26] X. He, J. T. Giurleo, and D. S. Talaga. Role of small oligomers on the amyloidogenic aggregation free-energy landscape. *J. Mol. Biol.*, 395:134–154, 2010.

[27] L. Sawyer and G. Kontopidis. The core lipocalin, bovine β-lactoglobulin. *Biochim. Biophys. Acta*, 1482(1-2):136–148, 2000.

[28] M. Groenning. Binding mode of thioflavin T and other molecular probes in the context of amyloid fibrils-current status. *J. Chem. Biol.*, 3(1):1–18, 2010.

[29] P. S. Vassar and C. F. Culling. Fluorescent stains, with special reference to amyloid and connective tissues. *Arch. Pathol.*, 68:487–498, 1959.

[30] H. LeVine. Thioflavine T interaction with synthetic Alzheimer's disease β-amyloid peptides: detection of amyloid aggregation in solution. *Protein Sci.*, 2(3):404–410, 1993.

[31] E. S. Voropai, M. P. Samtsov, K. N. Kaplevskii, A. A. Maskevich, V. I. Stepuro, O. I. Povarova, I. M. Kuznetsova, K. K. Toroverov, A. L. Fink, and V. N. Uverskii. Spectral properties of thioflavin T and its complexes with amyloid fibrils. *J. Appl. Spectrosc.*, 70:868–874, 2003.

[32] T. C. Messina, H. Kim, J. T. Giurleo, and D. S. Talaga. Hidden Markov model analysis of multichromophore photobleaching. *J. Phys. Chem. B*, 110(33):16366–16376, 2006.

[33] M. Biancalana and S. Koide. Molecular mechanism of thioflavin T binding to amyloid fibrils. *Biochim. Biophys. Acta.*, 1804(7):1405–1412, 2010.

[34] A. A. Maskevich, V. I. Stsiapura, V. A. Kuzmitsky, I. M. Kuznetsova, O. I. Povarova, V. N. Uversky, and K. K. Turoverov. Spectral properties of thioflavin T in solvents with different dielectric properties and in a fibril-incorporated form. *J. Proteome Res.*, 6(4):1392–1401, 2007.

[35] A. L. Fink. Factors affecting the fibrilliztion of α-synuclein, a natively unfolded protein. *Misbehaving proteins : protein (mis)folding, aggregation, and stability.*, pages 265–286, 2006.

Chapter 2

Role of Small Oligomers on the Amyloidogenic Aggregation Free-energy Landscape

2.1 Introduction

Proposed mechanisms of amyloid growth remain idiosyncratic to the precursor, conditions, and methods used. Our aim is to directly observe oligomeric intermediates and develop a detailed molecular model of amyloidogenesis. Such a model allows construction of an amyloidogenic aggregation free-energy landscape and enables a more universal approach to evaluating the roles of different amyloid-related species.

Amyloid deposition is observed in more than 20 diseases, including Alzheimer's disease, Creutzfeldt-Jakob's disease and Parkinson's disease. Each amyloid-related disease has a particular precursor protein or peptide that converts from its soluble native state to insoluble cross-β amyloid assemblies.[1,2,3,4] These diseases typically show a symptom-free latency period that is significantly shortened in the case of certain single amino acid familial mutations of the relevant precursor,[5,6,7,8] or gene triplication.[9] *in vitro* aggregation studies tend to show correlation between the amyloidogenic properties of different mutants and disease severity.[10,11,12,13] However, how this protein accumulation participates in the etiology of many of these diseases is still not fully understood.[3,14,1] We discuss the role of oligomers in amyloid-related diseases based on two hypothesis that differ in the identity of the pathogenic species.

The amyloid cascade hypothesis suggests that amyloid is the major causative agent in amyloid-related diseases.[15,16] Formation of amyloid is often explained by a nucleation-dependent kinetic mechanism. Once a critical nucleus is formed. the protein in question rapidly aggregates into amyloid fibrils and plaques. Massive fibril deposits can interfere with normal organ function. Amyloid lesions can induce an inflammatory response.[17,18]

Mature amyloid fibrils were also found to induce cell death *in vitro*.[19,20] However, other studies have shown amyloid fibrils to be relatively innocuous, leaving doubt as to their significance.[21,22,23]

To explain the poor correlation between amyloid load with disease progression, the toxic oligomer hypothesis has emerged. Evidence is mounting that soluble oligomeric intermediates have significant cytotoxic.[24,25,26,27,28,14,29,30,31,32,33] The toxic oligomer hypothesis states that the inherent toxicity of small oligomers of the amyloidogenic protein causes cellular dysfunction and that the presence of amyloid in amyloid-related diseases is coincidental, not causative. Cytotoxic has been observed for oligomers of both disease-related[34,35,36,37,38,39] and non–disease-related[40] proteins, suggesting that misfolded aggregates in general are pathological and calling into question the specific nature of the proteins associated with each disease.

Toxicity assays often involve cells and conditions different than those specific to the progression of amyloid-related diseases. Oligomers for toxicity assays are usually prepared under extreme conditions that are not physiological or amyloidogenic. The stability of such small oligomers is difficult to assay under cell culture conditions. Toxicity studies typically do not differentiate between the types of oligomers present.[34,28,36,37] Characterization of the oligomers varies widely and often involves low-resolution and/or unreliable methods.[41] As a result, it is not clear which species are actually present in the different studies. Where they have been characterized, oligomer toxicity appears to depend on size and structure.[35,38,39] The thermodynamic and kinetic properties of different oligomeric species will dictate their stability and physiological relevance. Therefore, an understanding of these properties is vital.

The toxic oligomer hypothesis does not account for the relationship between the toxic oligomer and amyloid; the proteins in amyloid diseases all form amyloid *in vivo*. Moreover, single amino acid mutations that increase rate of disease progression can also increase the rate of amyloid formation *in vitro*.[10,42,43] Under the toxic oligomer hypothesis, toxic oligomer and amyloid fibril formation is a coincidence that spans many diseases.

The ubiquitous presence of amyloid in amyloid-related diseases is often rationalized by invoking a protective role for amyloid fibril formation as a sink for the toxic oligomers.[14,44] However, no cellular machinery for producing amyloid from misfolded aggregates has been identified. Indeed, cellular action is not required for amyloid formation, as all amyloid-related disease precursors readily form amyloid *in vitro*. Nevertheless the conditions that are required to form amyloid *in vitro* are usually not at all physiological. In particular, rapid agitation in the presence of air-water interfaces is usually required *in vitro* suggesting that strong perturbation may be necessary for similar aggregation rates to occur *in vivo*.

In both hypotheses small aggregates play important but different roles. In the amyloid cascade hypothesis, the small aggregates are an intermediate state between the functional form and amyloid;[45,46,47,48,49,50,51] above a critical size they seed fibril formation.[52,53,54] Thus, oligomers that can seed amyloid formation are at the heart of the autocatalytic cycle. In the toxic oligomer hypothesis the pathology is more direct. The aggregates could trigger the unfolded protein response,[55] increase cell membrane permeability,[56,36,57,37,39] interfere with long-term potentiation,[34,33] or otherwise produce cytotoxicity.[58]

Distinguishing the type and role of oligomers is therefore important for understanding amyloid-related disease mechanisms. Toxic oligomers and the critical nucleus for amyloidosis have different free-energy landscape requirements. The free energy of the critical nucleus is at a maximum, whereas toxicity would require accumulation of appreciable populations — implying a free energy minimum. Thus, the relationship between these species can be defined in terms of their relative positions on the aggregation free-energy landscape.

Multiple techniques have observed sigmoidal kinetics for amyloid assembly. There is a lag phase, during which no amyloid aggregates are detected. A growth phase follows, in which proteins rapidly convert into amyloid with a fast increase in aggregate size and β-sheet rich structure. The lag phase can be shortened or removed by the addition of preformed fibril seeds. Kinetic results are extremely sensitive to the details of sample handling. Pre-existing seeds,[54] surfaces,[59,60,61,62] air-water interfaces,[63,64,62]

and agitation[65,66] can all strongly perturb the kinetics. These results suggest that amyloidogenesis is kinetically controlled.

Several methods have been commonly used to characterize amyloid intermediates. Static light scattering (SLS) and DLS provide size distributions,[53,67,48,68] but size and morphological heterogeneity prevent resolution of individual species.[69] Photo-induced cross-linking followed by SDS-PAGE has been used to study the size distribution of low–molecular-weight Aβ oligomers but is limited to differentiating small species. Cross-linking can skew the overall size distribution to smaller aggregate number.[47,67] AFM during amyloidogenic incubation shows the presence of different-sized globular particles,[70,71,72,73,74,75,76,77,35] worm-like beaded protofibrils,[78,75] and rare annular structures.[79]

Structural and spectroscopic methods are often used in parallel to correlate aggregation and conformational states. Increased β-sheet structure was detected by Raman spectroscopy for αSyn amyloid formation in tandem with AFM imaging of the aggregate assembly.[49] Fourier transform infrared spectroscopy was combined with AFM and EM to study human prion peptide PrP82-146 aggregation under different conditions.[51] Circular dichroism, intrinsic fluorescence,[80] and thioflavin T (ThT) luminescence[69] can also monitor structural changes. Intermediates may also be detected by oligomer-specific antibodies.[81]

Proposed mechanisms of amyloidogenesis vary greatly in spite of common kinetic features. A nucleation-dependent polymerization model for prion protein (PrP) and Aβ was proposed by a one-dimensional analogy to protein crystallization. The critical nucleus forms from and elongates by association of monomers with a specific structure.[52] Off-pathway species have also been added.[82] Acid-induced Aβ assembly was modeled by micelle-facilitated formation of nuclei. Only the moments of the fibril size distribution were compared with DLS data.[53,83] In all cases, no direct evidence for intermediates was offered and only the accumulation of amyloid was modeled.

A nucleated conformational conversion (NCC) model was proposed for Sup35. This model was based on the detection of an oligomeric lag phase intermediate that mediated nucleation and elongation. Monomers first associate into a fluid micelle-like oligomer,

which then rearranges to form an energetically unfavorable amyloidogenic nucleus. The nucleus grows by inducing conformational rearrangement in the oligomers.[54] A Lumry-Eyring step has been added to the nucleated polymerization model to account for pre-equilibrated monomer unfolding and increase fitting function flexibility. Again, averaged quantities were treated.[84] Phosphoglyceratekinase assembly kinetics has been modeled by Smoluchowski coagulation theory. Critical oligomers form by collision of smaller intermediates. Filaments grow linearly by the fusion of critical oligomers.[48]

Some studies find that amyloid assembly deviates from the nucleation-dependent mechanism. Transthyretin aggregation followed nucleation-independent downhill polymerization that was insensitive to seeding.[68] The ThT assay for amyloid may have registered a false positive as no fibrils were observed.

Understanding the molecular amyloid assembly mechanism is critical for developing a rational strategy to prevent the aggregation cascade events. A comprehensive molecular model of amyloidogenesis will have many features that are missing from current models. A molecular mechanism of amyloidogenesis must define the reactivity and roles of the oligomeric intermediates in order to evaluate their contribution in disease-progress hypotheses. This level of detail requires measuring both the conformational changes and the distribution of aggregate sizes through the aggregation processes. Intermediate species must be explicitly measured and included. The aggregates before and after nucleation should be distinguished. Linkage must be established between aggregation events and conformational changes. For example, if a hydrophobic core is present the point at which it is disrupted in favor of an aggregated form should be identified. Different types of aggregation events and conformational changes should have different barriers. The critical nucleus must be identified for nucleated processes. The mechanism should allow prediction of sequence and condition determinants of amyloid formation propensity. Representation of the amyloidogenic aggregation mechanism by a free-energy landscape allows a unified and intuitive presentation of these ideas.

The present study treats the bovine milk lipocalin β-LGA. Extensive studies of the stability, folding, and aggregation of β-LGA have been driven by basic science and the dairy and food processing industries.[85] Its biological role, beyond providing a source

of protein in milk, is unknown. It may enhance solubility of fat and fat-soluble nutrients through binding to the calyx.[86,87] Hydrophobic and amphiphilic fluorophores bound to the β-LGA calyx and other hydrophobic sites can be distinguished using fluorescence lifetime measurements.[88,89,69] β-LGA forms amyloid under various conditions.[90,91,76,92,69,93]

To follow the assembly of β-LGA into amyloid, we used time-resolved fluorescence of 1-anilino-8-naphthalene sulfonate (ANS) and ThT to monitor the conformational changes and used DLS and AFM to monitor the degree of aggregation.[69] Several ANS binding locations and β-LGA calyx were modified and disrupted during amyloid assembly.[69] A three-stage qualitative mechanism was proposed for β-LGA amyloidogenesis with two different classes of oligomer preceding amyloid protofibril formation. During the early lag phase, denatured monomers associated to form loosely bounded oligomers, AggA, in which the hydrophobic calyx was partially disrupted. During the late lag phase, AggA converted to a globular intermediate, AggB, in which the hydrophobic calyx was completely disrupted. Conversion of AggB to amyloid gave rise to abundant protofibrils in the growth phase. ANS and ThT luminescence for monomer, AggA, AggB and amyloid showed distinct lifetime distribution patterns.[69] The present study develops a quantitative kinetic model of the amyloidogenic aggregation of β-LGA by combining AFM oligomer size distributions with ANS, ThT and DLS measurements.[69] The kinetic model is based on oligomeric intermediates that were directly observed. An amyloidogenic aggregation free-energy surface is constructed from the details of the kinetic model.

2.2 Material and Methods

2.2.1 Incubation of β-Lactoglobulin a

β-LGA from bovine milk (Sigma product number: L-7880, Lot number: 026K7000) was found to contain salt impurities at a level of approximately 50% by mass and was therefore dialyzed against 100 mM pH 7.0 phosphate buffer to remove salt prior to use. Stock urea (Sigma) and phosphate (Sigma) buffer solutions were filtered with 0.02

and 0.22 μm filters, respectively. No filtration was done after protein solution dialysis. The final solution for incubation was approximately 0.95 mg/ml β-LGA in 13.7 mM, pH 7 phosphate buffer with 5.0 M urea. Concentration was verified by UV absorption. This sample was incubated in an Eppendorf tube at 37°C without agitation for over 30 days. Incubations were done on 3 separate occasions and produced consistent DLS and luminescence results each time. AFM measurements were performed in parallel from replicate samples and gave consistent results for three different incubations.

2.2.2 Atomic Force Microscopy Sample Preparation and Imaging

Each day, after inverting the tube once, 20 μL of the incubated solution was aliquoted for AFM imaging on modified mica. To modify the mica surface, 30 μL of 0.1% (v/v) APTES (Acros catalog number: 151081000) was applied evenly on freshly cleaved 9.9 mm diameter muscovite mica disk (Ted Pella product number: 50) and allowed to react for 10 minutes.[94] Unreacted APTES was rinsed away with 15 mL Millipore water. The surface was dried with HPLC grade compressed nitrogen gas. Incubated sample was applied evenly on this freshly prepared surface and allowed to adsorb for 10 minutes. Unbound species were rinsed away with Millipore water. Residual water was blown away with nitrogen gas. The sample was imaged by a MultiMode Scanning Probe Microscope with a Nanoscope IIIa controller (Veeco), with a tapping-mode etched silicon probe (TESP, Veeco) in tapping mode in air. The scan speed was 1 Hz with an image size of 512×512 pixels. Samples were stored in disk carriers when further imaging was required.

2.2.3 Image Analysis

Image analysis was performed using a custom protocol developed to identify, classify and measure all the particles in the many images taken throughout the incubation. We classified the detected particles as globular, protofibrillar and long fibrillar based on size and morphology. Models were used to deconvolute tip effects from the image lateral dimensions. The aggregation number, j, was calculated based on the deconvoluted size of particles.

Particle Identification

The tilt in raw AFM images was removed by fitting scan lines to a polynomial to yield flattened images. A dynamic threshold method was used to distinguish particles from the background.[95] Each non-border pixel in the flattened AFM image was assigned a local background level, $M(x, y)$, by averaging the values of $n \times n$ pixels around it. A user-defined threshold ϕ was assigned for each image according to its background and noise. Pixels with value $P(x, y) \geqslant M(x, y) + \phi$ were retained in a binary image mask to identify particles. Next, position of the pixels with maximum value in each particle in the masked image was determined. Using these peak pixels as centers, small $\rho \times \rho$ sub-images containing only one detected particle were extracted from the flattened image. These sub-images were used in the next particle classification and measurement steps.

Particle Classification

We classified the particles based on a few simple features. The rarely observed long fibrillar species needed a much greater number of pixels to describe them and were easily distinguished from globular and short protofibrils. Such long fibrils were manually characterized by their height profiles. The globular and protofibrillar classes were abundant, so we automated the classification and measurement protocol. The globular particles were distinguished from short protofibrils by circularity, or the ratio of the square of the particle perimeter to 4π times particle area. A perfectly circular particle consequently would have a circularity of 1. A value of 1.2 was used to distinguish globular and protofibrillar particle classes.

Particle Measurements

To automate the dimensional measurements of large numbers of globular and protofibrillar particles in the image, particles were fit to 2D functions. These functions were solely designed to capture the observed shape and size of particles on surface as in the AFM images. Sub-images containing globular particles were fitted to 2D Gaussian

function as in Eq. 2.1. The elliptical Gaussian function included deviation from circular geometry. Other functions were used to characterize the geometry. However, none offered improvements in reliability over the simple 2D Gaussian:

$$P_{\mathrm{g}}(x,y) = P_0 + \alpha \ \exp\left(-\frac{1}{2}\left[\left(\frac{\mathcal{X}}{\sigma_x}\right)^2 + \left(\frac{\mathcal{Y}}{\sigma_y}\right)^2\right]\right) \tag{2.1}$$

where,

$$\mathcal{X} = (y - y_0)\sin(\theta) + (x - x_0)\cos(\theta)$$
$$\mathcal{Y} = (y - y_0)\cos(\theta) - (x - x_0)\sin(\theta)$$

The fit parameters x_0 and y_0 gave the position of globular particles in the subimage and θ described their orientation. The background P_0, the amplitude α, and the standard deviation along major and minor axis of the 2D Gaussian, σ_x and σ_y, were related with particle dimensions. The fit parameter α systematically overestimated the height of globular particles in a width-dependent way. Therefore, we calculated the observed globular particle height on surface, H_{g}, by subtracting the local background P_0 from the maximum pixel value of the particle. The observed globular particle radius on surface, R_{g}, is calculated as the average of the half lengths at half maximum of the major and minor axes,

$$R_{\mathrm{g}} = \frac{\sqrt{2\ln 2}\ (\sigma_x + \sigma_y)}{2} \tag{2.2}$$

To model the morphology of protofibrils on surface, we used a box with a height H_{f}, length L_{f} and width W_{f}, convoluted with a symmetric 2D Gaussian with standard deviation σ_{c}. The resulting function was used to fit the subimages containing protofibrils (Eq.2.3.):

$$P_{\mathrm{f}}(x,y) = P_0 + H_{\mathrm{f}} \times$$

$$\frac{\left[\mathrm{erf}(\frac{\mathcal{X}-W_{\mathrm{f}}}{\sigma_{\mathrm{c}}\sqrt{2}}) - \mathrm{erf}(\frac{\mathcal{X}+W_{\mathrm{f}}}{\sigma_{\mathrm{c}}\sqrt{2}})\right]\left[\mathrm{erf}(\frac{\mathcal{Y}-L_{\mathrm{f}}}{\sigma_{\mathrm{c}}\sqrt{2}}) - \mathrm{erf}(\frac{\mathcal{Y}+L_{\mathrm{f}}}{\sigma_{\mathrm{c}}\sqrt{2}})\right]}{4\,\mathrm{erf}(\frac{W_{\mathrm{f}}}{\sigma_{\mathrm{c}}\sqrt{2}})\mathrm{erf}(\frac{L_{\mathrm{f}}}{\sigma_{\mathrm{c}}\sqrt{2}})} \tag{2.3}$$

The fit parameters H_{f}, L_{f} and W_{f} were used directly as the observed height, half length and half width of protofibrils on surface, respectively. σ_{c} accounted for both the edge shape of the protofibril and the tip.

Tip Deconvolution and Calculation of Aggregation Number

The molecular volume of each species observed is proportional to the aggregation number, j.

$$j = V_j/V_1 \tag{2.4}$$

The volume of the folded monomer, V_1 is approximately the maximum density achievable for the protein. Because of sample drying and soft sample tip compression, we assumed all the species on the surface had the same density as the folded monomer. With a molecular weight 18.4 kDa and a radius of ∼1.76 nm, the density of folded monomer was calculated to be 1.34×10^{-21} g/nm^3. To determine the aggregation number, j, for each species, we converted the fit dimensions of globular particles on surface to real particle dimensions and volume.

Particles in an AFM image are flattened by the interaction with the surface and by compression from the tip. We modeled the particles as a disc of thickness h_{g} with radius of r_{m} and $r_{\mathrm{m}} + h_{\mathrm{g}}$ for top and bottom surface, respectively (Fig. 2.1). Its volume V_{g} can be calculated as in Eq. 2.5.

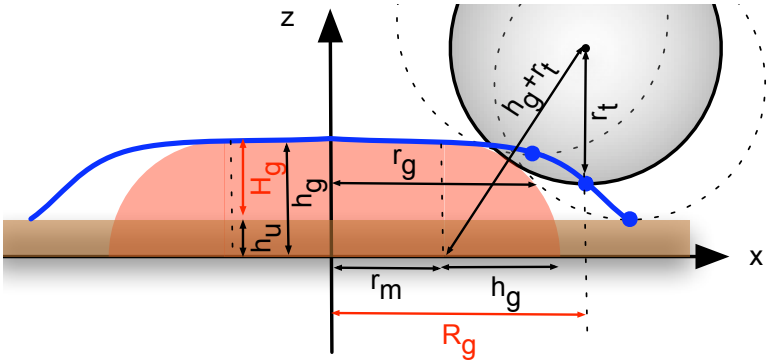

Figure 2.1: Schematic of tip scanning globular particles deposited on surface during AFM imaging. Globular particles are modelled as disc (shown in red) partially embedded in a layer of deformed protein of r_u thick (in brown). The tip is modelled as a sphere with radius r_t. The size of tip prevents it from exactly tracing the particles on surface. The trace (shown in blue) of the last atom on tip (blue spot) is recorded as particle profile during imaging. The height of particle (h_g) is underestimated to be H_g(=h_g-h_r) and the radius (r_g) is overestimated as R_g during measurement. Based on this model, with observed height H_g and radius R_g, we calculated the real dimension of globular particles on surface.

$$V_g = \int_0^{h_g} \pi \left(r_m + \sqrt{(h_g^2 - z^2)} \right)^2 dz$$

$$= \frac{1}{6} h_g \pi \left(4h_g^2 + 3\pi h_g r_m + 6r_m^2 \right) \tag{2.5}$$

Two experimental phenomena must be taken into account in the model. First, particles were partially embedded in a amorphous protein layer on the surface of thickness h_u, resulting in a smaller observed height, H_g:

$$H_g = h_g - h_u \tag{2.6}$$

Second, the lateral dimension of particles are overestimated by the effect of the AFM tip. We modeled the tip as a sphere with radius r_t. The blue trace in Fig. 2.1 illustrates the path recorded by the AFM tip under this geometry.

This observed profile, $z(x)$, can be represent analytically by a piecewise function:

$$z(x) = \begin{cases} h_{\mathrm{u}} & x < -\mathbb{X} \\ \sqrt{(h_{\mathrm{g}} + r_{\mathrm{t}})^2 - (x + r_{\mathrm{m}})^2} - r_{\mathrm{t}} & -\mathbb{X} \leq x \leq -r_{\mathrm{m}} \\ h_{\mathrm{g}} & -r_{\mathrm{m}} \leq x \leq r_{\mathrm{m}} \\ \sqrt{(h_{\mathrm{g}} + r_{\mathrm{t}})^2 - (x - r_{\mathrm{m}})^2} - r_{\mathrm{t}} & r_{\mathrm{m}} \leq x \leq \mathbb{X} \\ h_{\mathrm{u}} & \mathbb{X} \leq x \end{cases} \tag{2.7}$$

Where,

$$\mathbb{X} \equiv \sqrt{(h_{\mathrm{g}} + r_{\mathrm{t}})^{\,2} - (h_{\mathrm{u}} + r_{\mathrm{t}})^{\,2}} + r_{\mathrm{m}} \tag{2.8}$$

is the x position where the tip first contacts the particle.

R_{g} is the radius measured at the half-height and includes both an effect from the tip, r_t and the surface layer, h_u. The true radius of the particle at half-height above the layer is r_{g} and can be expressed by:

$$r_{\mathrm{g}} = r_{\mathrm{m}} + \frac{1}{2}\sqrt{(h_{\mathrm{g}} - h_{\mathrm{u}})\,(3h_{\mathrm{g}} + h_{\mathrm{u}})} \tag{2.9}$$

To convert the observed width R_{g} to the globular particle radius r_{g}, we use Eq. 2.9 and set Eq. 2.7 to its value at the experimentally observed, R_{g}, or $z(R_{\mathrm{g}}) = H_{\mathrm{g}}/2 + h_{\mathrm{u}}$. Solving for r_{g} while eliminating r_{m} and h_{g} gives,

$$r_{\mathrm{g}} = R_{\mathrm{g}} - \left(\sqrt{H_{\mathrm{g}}\left(h_{\mathrm{u}} + \frac{3}{4}H_{\mathrm{g}} + r_{\mathrm{t}}\right)} - \sqrt{H_{\mathrm{g}}\left(h_{\mathrm{u}} + \frac{3}{4}H_{\mathrm{g}}\right)}\right) \tag{2.10}$$

The parameter r_{m} is given by

$$r_{\mathrm{m}} = R_{\mathrm{g}} - \sqrt{H_{\mathrm{g}}\left(h_{\mathrm{u}} + \frac{3}{4}H_{\mathrm{g}} + r_{\mathrm{t}}\right)} \tag{2.11}$$

The volume of particle can be calculated from the experimental quantities substituting Eq. 2.6 and Eq. 2.11 into Eq. 2.5 giving:

$$\begin{aligned} V_{\mathrm{g}} = & \frac{1}{6}\pi\Bigg[4\,(H_{\mathrm{g}} + h_{\mathrm{u}})^3 \\ & + 3\pi\,(H_{\mathrm{g}} + h_{\mathrm{u}})^2\left(R_{\mathrm{g}} - \sqrt{H_{\mathrm{g}}\,(3H_{\mathrm{g}}/4 + h_{\mathrm{u}} + r_{\mathrm{t}})}\right) \\ & + 6\,(H_{\mathrm{g}} + h_{\mathrm{u}})\left(R_{\mathrm{g}} - \sqrt{H_{\mathrm{g}}\,(3H_{\mathrm{g}}/4 + h_{\mathrm{u}} + r_{\mathrm{t}})}\right)^2\Bigg] \end{aligned} \tag{2.12}$$

Using Eq. 2.12 requires the observed dimensions (H_{g}, R_{g}) for each particle and estimates for the tip radius, r_{t}, and thickness of the surface layer, h_{u} for the entire image. The amorphous protein layer on clean mica surfaces was observed to be 0.6 to 0.8 nm thick. Therefore, the surface layer thickness was taken to be h_{u}=0.7 nm for all images. Globular particles of the same volume and shape from different images should have the same height, h_g and lateral dimension, r_{g}. During imaging, tip wear and contamination from the sample resulted in deviation from its nominal ∼10 nm radius. Although the distribution of heights is relatively unaffected by the tip shape, the distribution of lateral dimensions is strongly perturbed by it. Images with slightly different tip radii were pooled by adjusting the tip radius parameter for each related image such that the overall height-lateral-dimension distribution was matched. We matched the H_{g} and real length ($2\times r_{\mathrm{g}}$) 2D histogram profiles for 50 images taken during the 32 days by adjusting the tip radius of each image. The tip radius was typically ∼20 nm, though this parameter ranged between 5 and 80 nm. The resulting total histogram, shown in Fig. 2.2, provided an empirical relationship between H_{g} and r_{g}:

$$H_{\mathrm{g}} = 0.50\sqrt{4r_{\mathrm{g}}^2 - 7.8^2} + 0.3 \tag{2.13}$$

shown as the dotted line in Fig. 2.2. This empirical function also allowed us to use Eq. 2.12 and Eq. 2.4 to correlate the heights of globular particles to their volumes and aggregation number, as shown by the numbered circles in Fig. 2.2. This relationship is used to convert kinetic simulation data, which returns the aggregation number, j, to particle dimensions that we compare with our data.

To determine the aggregation number of protofibrils, the same protein density was used as the globular particle on surface. We used the observed lateral dimension W_{f} and L_{f} directly to calculate the volume of protofibril on surface, V_{f}, assuming the tip effect for protofibrils was small because of their big size. Protofibrils were considered as an ellipsoid to estimate their volume as in Eq.2.14.

$$V_{\mathrm{f}} = \frac{\pi}{4} L_{\mathrm{f}} W_{\mathrm{f}} (H_{\mathrm{f}} + h_{\mathrm{u}}) \tag{2.14}$$

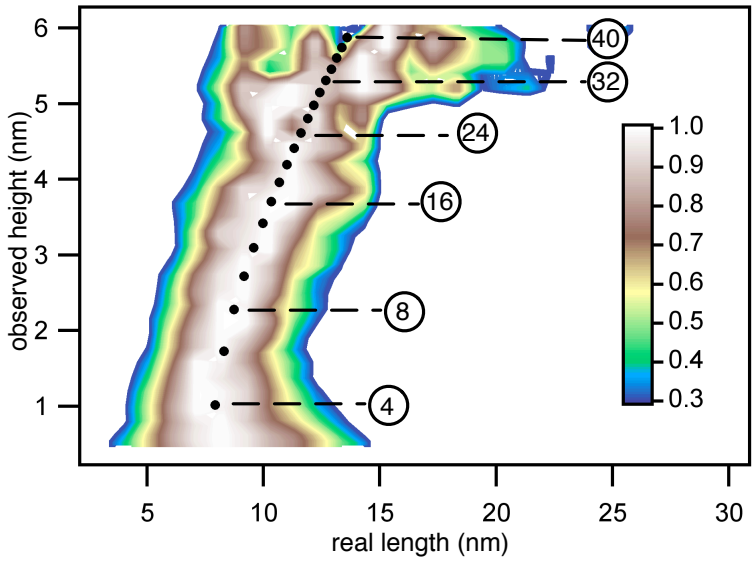

Figure 2.2: Observed height, real length ($2\times r_g$) profile of globular β-LGA aggregates on surface measured by AFM. Globular particles of a given size will be observed with same height in different images but with different lengths because of varying tip sizes. After removing the tip effect using Eq. 2.10, with different tip radii for each image, globular particles from 50 images taken through the incubation gave a unified observed height, real length profile. An empirical relationship between H_g and r_g was derived according to this profile. With known height and radius, the volume of globular particles were calculated with Eq. 2.12. The circled numbers indicate number of monomers in globular particles with corresponding observed height, calculated based on particle volume and density on the surface.

Image Analysis Protocol Performance

We applied this image analysis protocol to images from the first 32 incubation days. Every image had different noise level associated with imaging conditions, such as image size, tip, temperature, etc. We chose a local threshold (ϕ) to include all globular species and fibrils while rejecting the background from noise and the amorphous protein layer. Some small features of the background were unavoidably included. However, these features did not have a well-defined shape and were too small for the fitting algorithm to give accurate, converged fits. Whether a particle can be successfully fitted depended on how many pixels in the images were used to define the particle and the noise level in that

image. For images of the same size, fits of small particles defined by just several pixels were more likely to be compromised by noise than bigger particles. The higher resolution images allowed more pixels to define a particle of a given size, making it more likely to be successfully fitted. As a result, the population of smallest particles around 1 nm high was determined with high accuracy in the 2 μm images but was underestimated in 5 μm images. Other than this uncertainty, enough particles of different heights of interest were successfully fitted (more than 85%) to gave us a reliable estimation on the species present and their population distribution.

Even though we carefully controlled the sample deposition process, we observed small variations of particle coverage between samples. We attribute this variability to different degrees of APTES surface functionalization and to variation during the Millipore water rinsing step used to remove salt and any loose material. Though the particle coverage on surface varied between images, the relative populations appeared not to change for a given point in the incubation. Therefore to allow comparison between different days of the incubation, we normalized the two-dimensional height-length distribution for each day to the most populated species detected on that day.

2.2.4 Kinetic Simulations

All kinetic simulations were accomplished in Mathematica 6.0. Kinetic models (as discussed in the results section) were formulated based on the observation of different intermediates. We numerically solved the resulting coupled differential equations to get the population evolution for each species. These populations were compared to DLS and AFM results to determine kinetic rate constants and to discard kinetic models that could not be made consistent with observations.

Comparison of Simulations to Experiments

To directly compare with our DLS measurements, we simulated evolution of the correlation decay time distribution based on evolution of the population of different species given by the kinetic simulation, $a_j(t)$ (Eq. 2.15). We modeled the contribution of each species as a Gaussian distribution positioned at the decay time corresponding to its size

with a standard deviation of 0.004 ms.

$$I_{\mathrm{s}}(\tau,t)=\sum_j j^2 a_j(t)\exp\left(-\frac{1}{2}\left(\frac{\tau-\omega\sqrt[3]{j}}{0.004}\right)^2\right) \tag{2.15}$$

ω is the scale factor between particle size and decay time which was determined by our DLS experiments to be 0.02.[69]

To convert simulated population on each day, $a_j(t)$, to height, length 2D histogram as in AFM measurement, we used Eq. 2.16.

$$\psi_{\mathrm{s}}(l,H)=\sum_j a_j e^{-\frac{1}{2}\left(\frac{H-H_j}{\sigma_H}\right)^2} e^{-\frac{1}{2}\left(\frac{l-l_j}{\sigma_l}\right)^2} \tag{2.16}$$

where for globular particles the observed height, $H_{\mathrm{g},j}$, and real width $l_{\mathrm{g},j}$ (as $2r_{\mathrm{g},j}$) on surface can be calculated according to aggregation number as discussed above (Fig. 2.2). For protofibrils, an averaged observed height was used for $H_{\mathrm{f,g}}$. The length $l_{\mathrm{f},j}$ can be calculated (as L_{f}) with Eq. 2.14. σ_H and σ_l are the standard deviation in height and width measurement, respectively. They were estimated to be 0.37 nm and 2 nm, based on the dispersion of height and length signal in the experimental height-length 2D histogram.

To generate the ANS fluorescence lifetime fingerprint evolution based on population evolution from kinetic simulation, we assumed that the fluorescence intensity was proportional to aggregation number, j, in each species. The total fluorescence $C_a(t)$ for a given class of oligomer was obtained by the weighted sum:

$$C_a(t)\propto\sum_j j a_j(t) \tag{2.17}$$

where $a_j(t)$ is the time evolution of species concentration, a_j, where $a\in\{A,B,F\}$ and j was summed over the range of relevant oligomer sizes. The same proportionality constant was used for all species.

Determination of Rate Coefficients

The early lag phase contained several rate coefficients that we fit by minimizing the Kullback-Leibler (K-L) divergence[96] between the simulated correlation decay time distribution evolution and experimental data:

$$\sum_{\tau,t}\left(I_{\mathrm{s}}(\tau,t)^{\dagger}-I_{\mathrm{e}}(\tau,t)^{\dagger}-I_{\mathrm{s}}(\tau,t)^{\dagger}\mathrm{Log}\frac{I_{\mathrm{s}}(\tau,t)^{\dagger}}{I_{\mathrm{e}}(\tau,t)^{\dagger}}\right) \tag{2.18}$$

where $I_{\mathrm{s}}(\tau,t)^{\dagger}$ and $I_{\mathrm{e}}(\tau,t)^{\dagger}$ are the DLS correlation decay time distributions normalized by maximum intensity of each incubation time point, from simulation (Eq. 2.15) and experiment, respectively. After finding the minimum divergence, we perturbed each parameter to evaluate the sensitivity of the fit.

To account for the many related association reactions present in the late lag phase and the growth phase, we began from a basic encounter-theory approach, assuming diffusion-limited collisions with a free energy of activation that accounts for both entropic and energetic barriers to aggregation.[97] The rate constant for association steps during these phases, k_{j+}, can thus be expressed as in Eq. 2.19.

$$k_{j+}=k_{j}^{\mathrm{d}}\times e^{-\frac{\Delta G^{\ddagger}}{k_{\mathrm{B}}T}} \tag{2.19}$$

where k_j^{d} is the diffusion limited rate constant for species with aggregation number, j, reacting with the the assembly unit. k_B is the Boltzmann constant. $\Delta G^{\ddagger}$ is the free energy barrier for that association step.

The diffusion-limited rate coefficients for globular particle growth by addition of globular assembly unit, A_δ, were calculated with

$$k_{\mathrm{g},j}^{\mathrm{d}}=4\pi(D_{\delta}+D_{\mathrm{g},j})(r_{\mathrm{sol},\delta}+r_{\mathrm{sol},j}) \tag{2.20}$$

where D_δ and $D_{\mathrm{g},j}$ are the diffusion constants for globular assembly unit and globular particles, respectively, which can be calculated with Einstein-Stokes-Debye equation. The globular particle radius in solution, $r_{\mathrm{sol},j}$, was calculated assuming all the globular species have the same density $4.67\times10^{-22}\mathrm{g/nm}^3$, which was calculated with a partially unfolded monomer radius ~2.5 nm from DLS measurements.[69]

$$D_{\mathrm{g},j} = \frac{k_{\mathrm{B}}T}{6\pi\eta r_{\mathrm{sol},j}} \tag{2.21}$$

where η is the viscosity of protein solution, 0.876 centipoise in our case (measured for 5 M urea in buffer at 37°C).

For protofibril elongation, fibril-fibril interaction was not included in the simulation. Protofibrils elongated by adding globular assembly units to the end. We assumed that protofibrils had the same density and dimension in solution and on surface. The protofibrils were treated as a string of imaginary touching spheres whose diameter equalled to protofibril height.[98] The diffusion-limited rate coefficient in this case is

$$k^{\mathrm{d}}_{\mathrm{f},j} = 4\pi(D_{\mathrm{f},j} + D_{\delta})(r_{\mathrm{sol},\delta} + r_{\mathrm{is}}) \tag{2.22}$$

where $D_{\mathrm{f},j}$ and D_{δ} are the diffusion constants for fibril and the globular assembly unit, respectively. r_{is} is the radius of the imaginary sphere, which equals half the height of protofibrils, $H_{\mathrm{f}} + h_{\mathrm{u}}$. Again, an averaged height on surface was used.

The diffusion constants were calculated using:

$$D_{\mathrm{f},j} = \frac{D_{\mathrm{is}} \ln N}{N} \tag{2.23}$$

where D_{is} is the diffusion constant for the imaginary sphere and N is the number of spheres along the protofibril, calculated as the protofibril length divided by protofibril height.[98]

Calculation of Free Energy Difference

The free energy difference was calculated as

$$\Delta G^{\circ}_{j} = -k_B T \ln \frac{k_{j+}}{k_{(j+\delta)-}} \tag{2.24}$$

δ is the number of monomers in the association unit and $k_{(j+\delta)-}$ is the reverse rate for association steps.

2.3 Results

2.3.1 Aggregate Morphology Shows Two Growth Pathways

On each of the 32 days of incubation, we imaged samples deposited on aminopropyltetratheoxysilane (APTES)-modified mica using tapping mode AFM. The images showed five phases of aggregate growth.

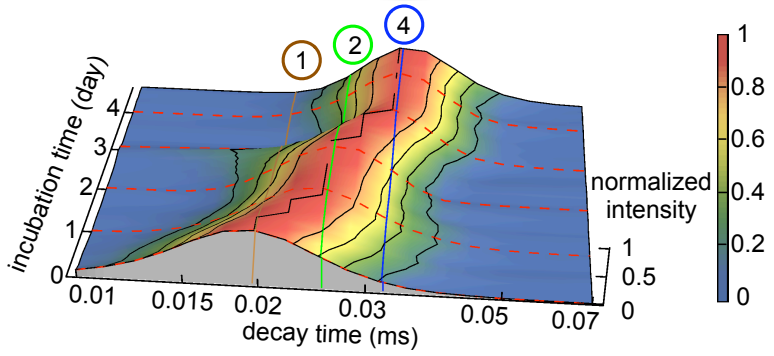

Figure 2.3: The evolution of the correlation decay time distribution monitored by continuous DLS during first 4.7 days of incubation. We related the particle decay time to spherical hydrodynamic radius using the Stokes-Einstein relation. The characteristic density of the partially unfolded monomer determined from assignment of a urea titration DLS experiment at 5 M was used to scale the oligomer sizes. The brown, green, and blue lines correspond to the correlation decay times of globular monomer, dimer and tetramer, respectively. The correlation decay time distributions were renormalized to the maximum intensity at each incubation time point. The peak shifted from monomer at the beginning of incubation, to dimer by day 2 and tetramer by day 4. Based on this data, a sequential assembly pathway, monomer→dimer→tetramer, ($A_1 \rightarrow A_2 \rightarrow A_4$) is proposed for AggA aggregation.

Incubation days 0 through 9 showed amorphous protein layer, with no sign of stable well-defined particles in the AFM images. However, DLS measurements showed a dramatic decrease in monomer population and an accumulation of dimers and tetramers during this period (Fig. 2.3).[69] Accompanying this increase in particle size, time-resolved fluorescence lifetime analysis of intercalated ANS showed a change in accessibility to the calyx site, indicative of a conformation change. Moreover, the change persisted upon dilution to native conditions.[69] The AFM images suggest that surface dissociation into the amorphous protein layer prevented detection of the early lag

phase oligomers. Thus the early lag phase oligomers are lower in free energy than the folded-state monomers and higher in free energy than surface-dissociated monomers. We designate this class of oligomers as AggA and the period, from days 0 to 9, during which they accumulated as the early lag phase.

Late Lag Phase (Days 10 to 21)

After day 10, individual globular particles of different sizes were imaged by AFM as in Fig. 2.4a, indicating the formation of oligomers that were stable with respect to dissociation on the APTES surface. The AFM image coverage by resolvable particles varied and was typically about 5%, providing a good balance between particle differentiation and statistics. From day 10 to 21, most particles imaged by AFM were globular, with heights between ∼1 nm and ∼2 nm above the amorphous protein layer, which was also observed in the early lag phase (Fig. 2.4a,b). According to our derived relationship between height and number of monomers in globular particles (Fig. 2.2), this range of heights corresponds to globular oligomers containing 4 to 8 monomers, with the majority species being tetrameric, as shown in Fig.2.4 a, e and Fig. 2.4b, f. Particles with heights between ∼2 nm and ∼4 nm were observed less often. This range of heights corresponds to globular oligomers with up to 16 monomers.

The wing that appears in the DLS correlation decay time distribution during this period is consistent with growth of particle to sizes between 8 and 40 monomers (Fig. 2.5). This size increase coincided with loss of the structured calyx site as detected by ANS fluorescence,[69] suggesting a structural rearrangement of the monomers within the oligomer. This set of observations led us to designate this larger and structurally distinct class of oligomers as AggB. The formation and growth of AggB preceding the conversion to amyloid protofibrils defines the late lag phase, *i.e.*, days 10 to 21. Short fibrillar species could occasionally be detected (Fig. 2.4b), foretelling the beginning of the growth phase.

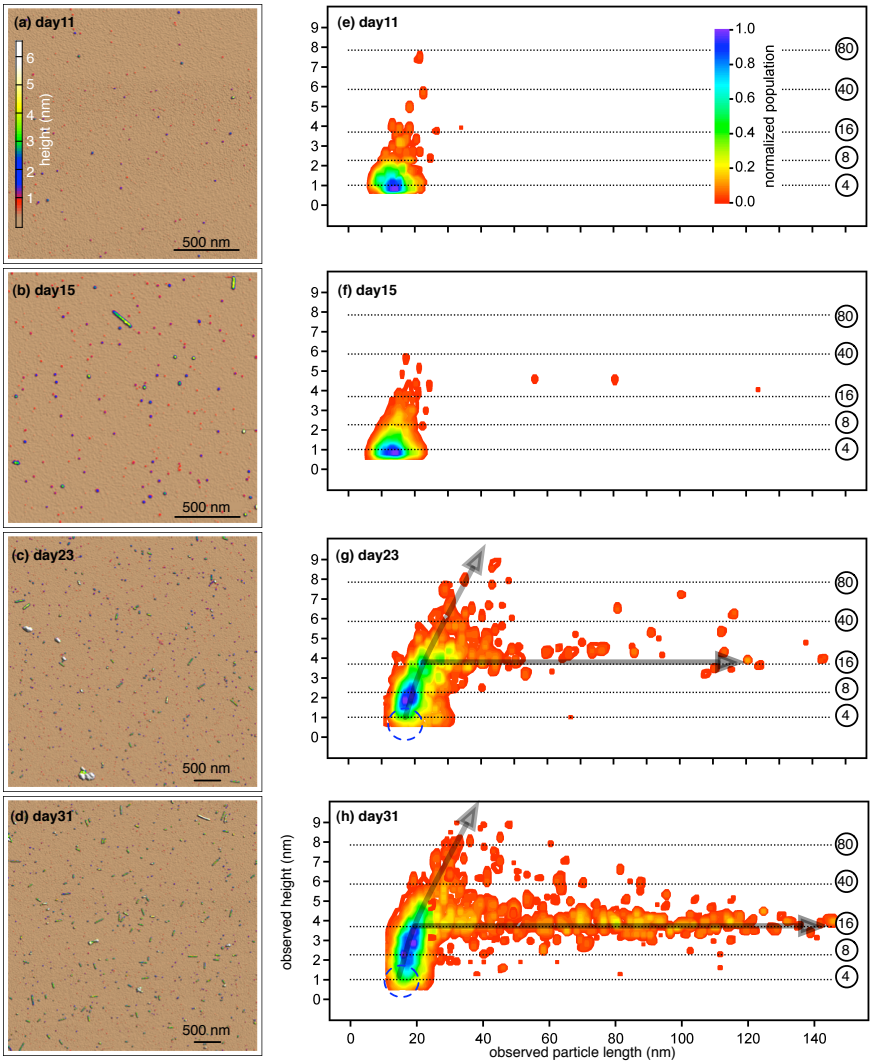

Figure 2.4: Particles were imaged with AFM from late lag phase through late growth phase. The left panels are typical AFM images taken during (a) late lag phase (day 11), (b) transition to growth phase (day 15), (c) early growth phase (day 23), and (d) late growth phase (day 31). Particles were identified, measured and assembled into the two-dimensional histograms of the observed height and length that appear on the right (e-h). The population distribution was normalized by most populated species on that day. (e) Day 11: 533 particles from five 2×2 μm images. Small globular particles dominated. (f) Day 15: 2471 particles from ten 2×2 μm images. Larger globular particles appeared. (g) Day 23: 801 particles from two $5\times5\,\mu$m images. Short protofibrils appeared. (h) Day 31: 1179 globular particles and 291 short protofibrils from four $5\times5\,\mu$m images. Many protofibrils appeared. The circled number on the right of two-dimensional histogram are the estimated number of monomers in globular particles of corresponding height, referring to Fig. 2.2. The growth phase showed two growth trends (arrows in (g,f)): globular assembly and fibrillar elongation. The small particles with height around 1 nm were more reliably resolved in the lag phase $2\times2\,\mu$m images than in the growth phase $5\times5\,\mu$m images. As a result, the population of such particles is underestimated in the region indicated by the blue circles in (g) and (h).

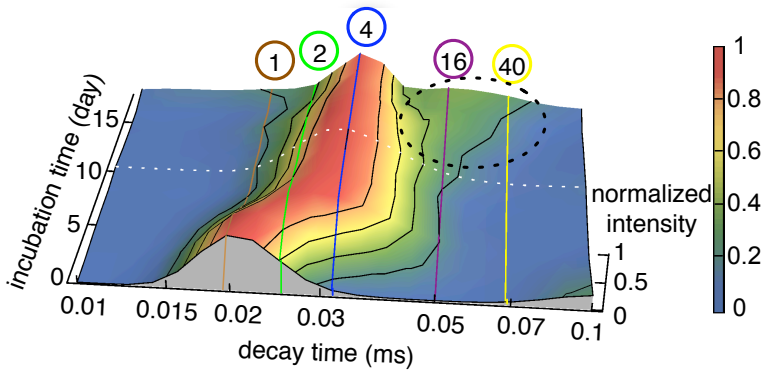

Figure 2.5: The evolution of the correlation decay time distribution monitored by continuous DLS during the first 18 days of incubation. The brown, green, blue, purple and yellow lines correspond to the correlation decay times of globular monomer, dimer, tetramer, hexadecamer, and 40-mer, respectively. The intensity was normalized by maximum intensity of each incubation time point. The tetramer remained the dominant peak from days 4 to 18. After day 10, a wing appeared to longer decay times indicating aggregate growth up to approximately 40-mers. Because spherical particles contribute to homodyne-detected DLS in proportion to the square of their volumes, the relative population of aggregates contained in this wing was even smaller than their small amplitude with respect to the tetramer peak might suggest. The appearance of this wing coincided with AFM detection of globular particles on the surface. These observations put together suggest that growth of a conformationally distinct species, AggB, defines the late lag phase.

Early Growth Phase (Days 22 to 28)

By day 22, it became common to observe short rod-like fibrillar structures of different lengths, coexisting with globular particles (Fig. 2.4c). Most fibrillar particles were approximately 3 to 5 nm thick. We assigned this thinnest class of rod-like fibrillar particles as protofibrils. Protofibrils present at this stage gave a specific ThT lifetime distribution that was different from mature fibrils.[69] Thicker fibrillar species did appear at this stage but were very rare. Protofibril population increased rapidly for the 9 days following day 22, consistent with designating this stage of assembly as the early growth phase.

Overall, the size of globular AggB increased during this phase. The low resolution of 5 μm images used for analysis in this stage hindered the precise determination of population for smallest ($\sim$1 nm) species. However, there was a clear increase in population

of particles ∼2 nm to ∼4.5 nm high, corresponding to species ranging from octamer (B_8) to 24-mer (B_{24}). A small population of particles larger than 4.5 nm, which were absent in the lag phase, were detected during the early growth phase.

Two trends of self-assembly emerged in the height-length two-dimensional histograms (Fig. 2.4g). One trend continued to follow the globular growth pattern from the late lag phase, resulting in a relatively small population of round particles with heights ranging from ∼4 nm to ∼8 nm. The second trend led to rod-like protofibrils.

Late Growth Phase (Days 29+)

Late growth phase AFM images (Fig. 2.4d) showed globular particles as well as a dramatic increase in protofibril number and length. Analysis of more than 200 of these protofibrils gave an average height of ∼3.8 nm and width of ∼11 nm. The protofibrils were straight, unbranched and usually had a small variation in height along their length. Some longer protofibrils showed periodic variation in height. The longest protofibrils we detected were ∼150 nm. Assuming that the protofibrils on surface have the same density as fully folded monomer, we estimated about 250 monomers for the longest protofibrils. The protofibril length distribution showed contributions across all lengths from 20 to 150 nm, suggesting a relatively small growth unit. However, a modest dip in population from 40 to 60 nm was also observed.

The bifurcation of the two aggregation trends became quite clear during this stage (Fig. 2.4h). The juncture at which globular particles appear to choose between the two modes of assembly occurs at 3.8 nm, roughly corresponding to B_{16}. Along the globular growth pathway, after the bifurcation point, further growth of AggB resulted in a small population of AggB larger than hexadecamers. The population of globular particles between ∼3 nm and ∼4 nm, corresponding to B_{12} and B_{16}, increased and became comparable to that of B_8. The population of AggB larger than the bifurcation point was clearly lower than that of smaller AggB (Fig. 2.4h).

AFM images after more than 60 days of incubation dominated by mature fibrils, indicating that much of the protein had been incorporated into mature fibrils as shown in Fig. 2.6. The fibril profiles showed different heights and height periodicities along

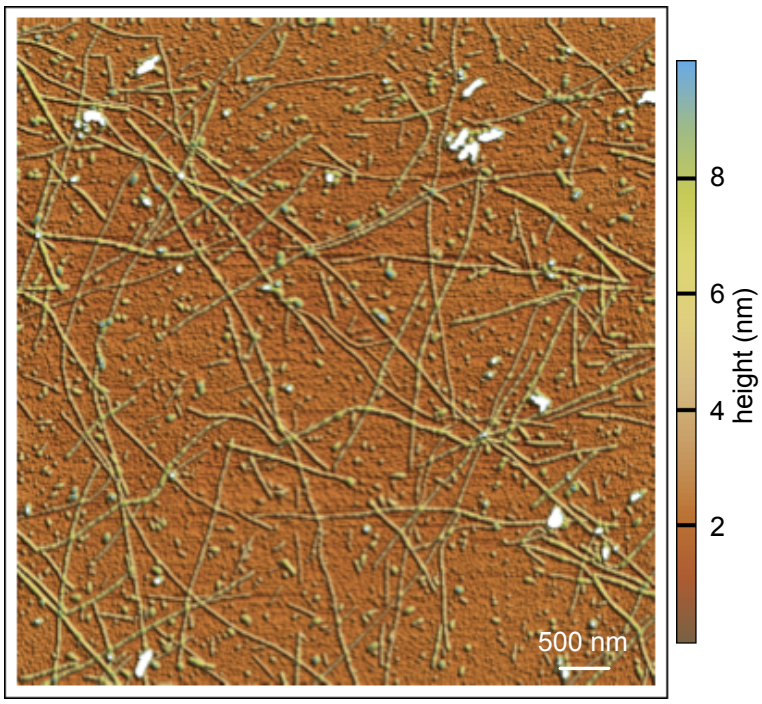

Figure 2.6: Mature amyloid fibrils detected by AFM after 65 days of incubation. During late stage incubation, mature fibrils of different heights were observed in large numbers. They coexisted with small globular particles and large amorphous particles on the surface. These fibrils were unbranched, curved and could be several micrometer long.

them. The mature fibrils could be several μm long. Our ThT luminescence measurements showed a noticeably different lifetime distribution pattern than that observed during the growth phase which was dominated by protofibrils.[69] Globular particles and short protofibrils were also observed to coexist with mature fibrils. Some very thick amorphous particles were observed but were absent from early stages.

2.3.2 Mechanisms from Kinetic Data

Approach to Simulating Kinetics

We include all classes of species as defined by analysis of AFM, DLS and luminescence lifetime distribution.[69] We calculate the evolution of the concentration of all kinetically active species without first simplifying to moment analysis or other averaged quantities. To simplify the optimization of the individual kinetic rate constants, we treat

bimolecular reactions with activated collision theory assigning similar barriers to similar reactions. This allows us to define the rate coefficients in terms of energetics. We included only the minimum number of intermediate species and reaction steps necessary to reconstruct the major features of the observed data. In general, an infinite number of more complicated mechanisms could also fit the data. We parsimoniously reject such mechanisms. By including both forward and reverse rates in our analysis we are able to estimate free energy changes at each step of the aggregation.

Early Lag Phase Reactions

The main feature of experimental DLS data for early lag phase was a shift from the monomer peak at time 0 to dimer by day 2 and tetramer by day 4 (Fig. 2.3). After day 4, the distribution pattern did not change until the start of late lag phase. This evidence shows that species presented during this early lag phase (AggA) is composed of monomeric (M), dimeric and tetrameric (A_4) forms. Moreover, monomers aggregated into tetramers through dimers and resulted in an accumulation of dimers and tetramers.

Non-reducing SDS-PAGE showed oxidative aggregation essentially halted at the dimer stage with substantial reduced monomer still present. This result suggested that tetramers form from oxidative dimers, A_2^{Ox}, and non-oxidative dimers (A_2) or monomers ($2\ M$) (Fig. 2.7).

To account for our observations and fit the DLS data, we propose a three-step mechanism to create A_4 as shown in Scheme 1. Initially, weakly associated dimers, A_2, formed from monomers. A_2^{Ox} formed by structural reorganization and oxidation of A_2. By day 4, both types of dimers had aggregated to form A_4.

$$M + M \underset{ka_{2-}}{\overset{ka_{1+}}{\rightleftharpoons}} A_2$$

$$A_2 \underset{koa_-}{\overset{koa_+}{\rightleftharpoons}} A_2^{\mathrm{Ox}}$$

$$A_2 + A_2^{\mathrm{Ox}} \underset{ka_{4-}}{\overset{ka_{2+}}{\rightleftharpoons}} A_4$$

SCHEME 1

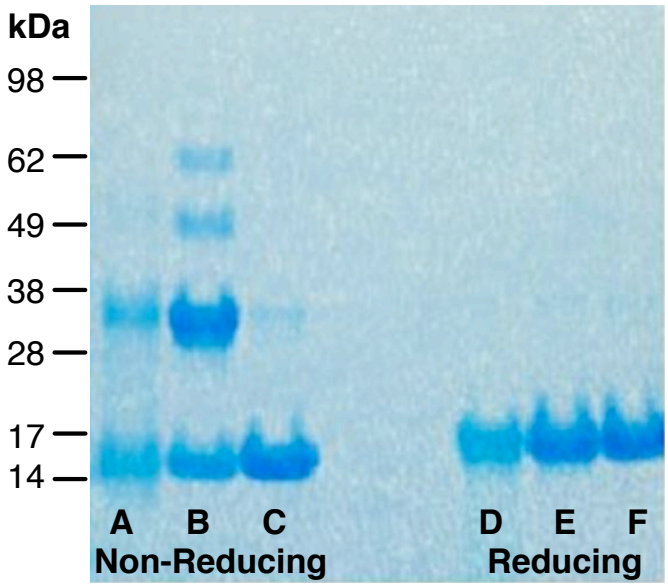

Figure 2.7: Non-reducing and reducing SDS-PAGE for protein solution at different incubation stage. The three columns on the left are non-reducing. Column A is for late stage of the incubation over 50 days. Column B is for incubation after 5 days and column C for β-LGA solution before incubation. Dithiothreitol (DTT) was used as disulfide reducing agent and mixed with protein solution before loading for column D, E, and F. Column D is for late stage of the incubation over 50 days to compare with column A. Column E and F are for incubation after 5 days and protein solution before incubation to compare with column B and C. For late stage incubation in column A, we can see that only monomer and dimer are present as oligomers, and most late stage products are too big to be analyzed with SDS-PAGE. Compared with incubation after 5 days for column B, oligomeric band of dimer, trimer and tetramer size are present, with dimer as the most populated species. After adding DTT into these two incubations, all the oligomeric bands disappear, which indicates that all these bands are from aggregates formed by disulfide bond. The disappearance of the trimeric and tetrameric bands in column B after longer incubation as indicated in column A indicates that oxidative oligomers bigger than dimer are most likely to be off-pathway species.

The simulation result for the proposed scheme was presented in Fig. 2.8, with rate coefficients in Table 2.1. The rate coefficients were optimized by minimizing the Kullback-Leibler distance as in Eq. 2.18. This simulation successfully caught the sequential shift of intensity peak in DLS from monomer to dimer to tetramer. A close comparison of the simulation to experimental data reveals a difference mainly in the width of distribution at each time point. However, without an adequate noise model for the DLS simulation a strict comparison between simulation and experimental DLS was inappropriate

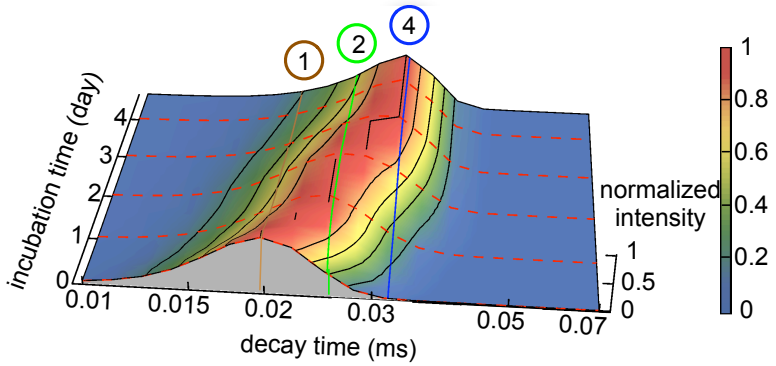

Figure 2.8: The evolution of the DLS correlation decay time distribution was constructed from a kinetic simulation of the first 4.7 days of aggregation according to Scheme 1. Species population a_j was converted to DLS decay time distribution ($I_s(\tau, t)$) using Eq. 2.15. The correlation-time distributions were renormalized to the maximum intensity at each incubation time point to facilitate comparison to the experimental data. Rate coefficients in Scheme 1 were optimized to match the constructed distribution to experimental data in Fig. 2.3. The brown, green and blue lines correspond to the correlation decay times of globular monomer, dimer and tetramer, respectively. Simulation based on Scheme 1 captured the earliest aggregation events: The DLS decay time distribution shifted from monomer to dimer, then to tetramer by day 4.

(ill-formed noise was addressed in the simulation and we do not know how particles of different sizes actually contribute to dispersed decay time distribution in our DLS measurement).

ka_{1+} $(\mu\text{M day})^{-1}$	ka_{2-} day^{-1}	koa_{+} day^{-1}	koa_{-} day^{-1}	ka_{2+} $(\mu\text{M day})^{-1}$	ka_{4-} day^{-1}
0.011	0.05*	0.28	0.05*	0.066	0.005*
$\Delta G^\circ \leq -2.0$ kJ/mol		$\Delta G^\circ \leq -4.4$ kJ/mol		$\Delta G^\circ \leq -6.7$ kJ/mol	

Table 2.1: Optimized rate coefficients for early lag phase simulation. *The three reverse rate coefficients are upper limits; whereas fit gives results effectively 0, simulations were insensitive to rates below these values. The free energy change, ΔG°, is calculated based on forward and reverse rate coefficients of each step, using Eq. 2.24.

The broadening to longer decay times might be caused by a small amount of AggA larger than A_4 or be due to the limits of the Gaussian model we used for the dispersion of the DLS distribution. We found that inclusion of AggA species larger than tetramers did not significantly improve the simulation of the data set. To be thorough, we also

included possible pathways, $2(A_2)$ to A_4 , and $2(A_2^{Ox})$ to A_4 along with formation of heterotetramers. We found that the main features of the data were reproduced with or without the added complexity. Thus, these minor pathways were excluded from the final mechanism *lex parsimoniae*.

All the reactions in this stage were determined to be energetically favorable. Monomers converted readily to more stable oligomers —A_2, A_2^{Ox} and A_4— under the experimental condition during the early lag phase.

Transition to Growth Phase

After day 10, a new class of globular aggregates, AggB, began to appear and grow in size along a globular growth pathway throughout the incubation as detected with AFM and DLS. We propose that A_4, formed in the early lag phase, converted to B_4 through a conformational change that eliminated the calyx binding site for ANS. This change in structural state was detected in our ANS and ThT measurement as a change in the lifetime distribution pattern.[69] It also enabled AggB to be stably absorbed to modified mica surface and detected with AFM.

We simulated the AggB aggregation along this globular growth pathway by appending Scheme 2 to Scheme 1, extending the aggregation mechanism through the late lag phase before protofibril formation. Converting the AFM height–length two-dimensional histogram (Fig. 2.4e-h) to oligomer size indicates that AggB sizes ranged from about tetramer (B_4) to 80-mer (B_{80}) during the 31 days of incubation. The globular particle aggregation number histogram on day 31 appeared to be multimodal with peaks separated by 4 monomer units. Moreover, an analysis of the effect of the size and type of species responsible for increasing AggB size found that a tetrameric unit of assembly,

A_4, best fit the data.

$$
\begin{aligned}
&A_4 \underset{kab_-}{\overset{kab_+}{\rightleftharpoons}} B_4 \\
&B_4 + A_4 \underset{kb_{8-}}{\overset{kb_{4+}}{\rightleftharpoons}} B_8 \\
&B_8 + A_4 \underset{kb_{12-}}{\overset{kb_{8+}}{\rightleftharpoons}} B_{12} \\
&\vdots \\
&B_{76} + A_4 \underset{kb_{80-}}{\overset{kb_{76+}}{\rightleftharpoons}} B_{80}
\end{aligned}
$$

SCHEME 2

Fig. 2.5 shows the evolution of the DLS correlation decay time distribution during incubation for the first 18 days from DLS measurement. We estimated our rate coefficents in Scheme 2 by matching the simulated decay time distribution with this data. We scaled the forward rate coefficients for the association steps, kb_+s, with Eq. 2.19, assuming the same energy barrier $\Delta G^\ddagger$ for all these steps. This assumption implies that the interaction between all AggB and A_4 are the same, reducing the number of kb_+ from 19 to 1. The same reverse rate coefficient was used for all the disassociation reactions here.

In the experimental data, a wing apart from the predominant tetrameric peak appeared around day 10 (Fig. 2.5). This wing corresponded to AggB sized between tetramers and 40-mers. The small intensity of this wing indicated that these bigger AggB were relatively small in population compared with the tetrameric form, A_4 and B_4. The addition of Scheme 2 to the model successfully reproduced the evolution of the DLS wing arising from AggB growth. Moreover, it reproduced the population relationship between AggA and AggB implied by the intensity difference of their contributions to the decay time distribution (Fig. 2.9). The small discrepancy between the shape of the simulated and experimental DLS decay time distribution is again attributed to the lack of a noise model for DLS. Because of the great heterogenerity of the system at this stage, multiple species contribute to the edge of the AggB wing. This situation

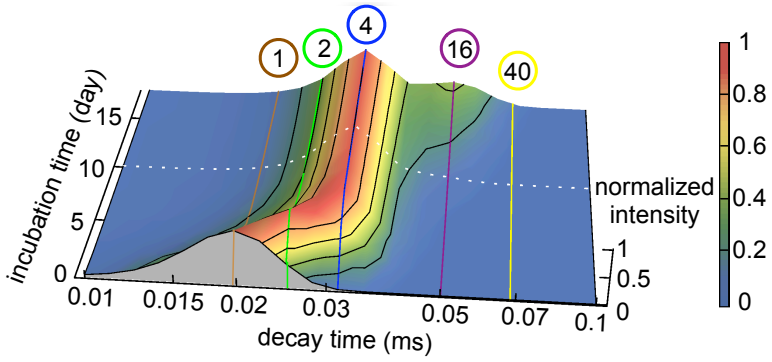

Figure 2.9: DLS correlation decay time evolution constructed based on species population from kinetic simulations for the first 18 days of incubation. We included AggB aggregation before protofibril formation as in Scheme 2. a_j was converted to DLS decay time distribution ($I_s(\tau, t)$) using Eq. 2.15. The correlation-time distributions were normalized to the maximum intensity at each incubation time point. The brown, green, blue, purple and yellow lines correspond to the correlation decay times of globular monomer, dimer, tetramer, hexadecamer and 40-mer, respectively. This simulation including AggB aggregation with successfully captured the assembly event occured during late lag phase, as shown by the wing that appeared around day 10.

prevents a precise determination of the maximum particle size in the experimental data. However, we will show below that these larger (∼40-mers) AggB species are beyond the point at which the aggregates convert to protofibrils and have minimal influence on the overall kinetic behavior. Optimized rate coefficients and barrier parameters appear in Table 2.2. According to these parameters, formation and growth of AggB were energetically unfavorable under incubation conditions.

kab_+ $(\text{day})^{-1}$	kab_- day^{-1}	kb_{4+} $(\mu\text{M day})^{-1}$	kb_{8-} day^{-1}	$\Delta G^{\ddagger}$ kJ/mol
0.024	0.28	0.023	0.067	62.1
$\Delta G^{\circ} = 6.9$ kJ/mol		$\Delta G^{\circ} = 2.7$ kJ/mol		

Table 2.2: Optimized rate coefficients for late lag phase simulation under Scheme 2. The free energy change, ΔG°, is calculated based on forward and reverse rate coefficients of each step, using Eq. 2.24. $\Delta G^{\ddagger}$ is the energy barrier for $AggB$ growth steps.

We also tested whether B_4 can be used as the assembly unit for AggB growth. The amount of AggB in both cases was determined by the formation of B_4 from A_4. The rate coefficients required to match the experimental data implied that AggB aggregation

was energetically favorable. This result precludes a nucleation barrier to protofibril formation from AggB. These observations and the characterization of the formation of amyloid as a nucleated process lead us to discount this mechanism. However, from the experiments we cannot conclusively distinguish between them. In the discussion that follows, our conclusions about the roles of the different classes of oligomers do not change depending on this detail of the mechanism.

Growth Phase Reactions

Starting around day 20, a second pathway for aggregation was observed by AFM: protofibril formation and elongation. The second pathway caused a bifurcation in the height-length two-dimensional histogram at around B_{16} (Fig. 2.4g,h). We added Scheme 3 to our overall mechanism to accommodate protofibril formation and elongation. We propose that once B_{16} is formed, it may either continue to grow into B_{20} or go through a conformational change to form a protofibril nucleus F_{16}. This conversion to protofibril structure was confirmed by ANS and ThT fluorescence lifetime measurements.[69] Protofibrils were observed to grow as long as 150 nm (Fig. 2.4h), corresponding to about a 252-mer. We considered the protofibrils to elongate through association with A_4, the most populated species prior to the growth phase.

$$B_{16} \underset{k_{bf-}}{\overset{k_{bf+}}{\rightleftharpoons}} F_{16}$$

$$F_{16} + A_4 \underset{kf_{20-}}{\overset{kf_{16+}}{\rightleftharpoons}} F_{20}$$

$$F_{20} + A_4 \underset{kf_{24-}}{\overset{kf_{20+}}{\rightleftharpoons}} F_{24}$$

$$\vdots$$

$$F_{248} + A_4 \underset{kf_{252-}}{\overset{kf_{248+}}{\rightleftharpoons}} F_{252}$$

SCHEME 3

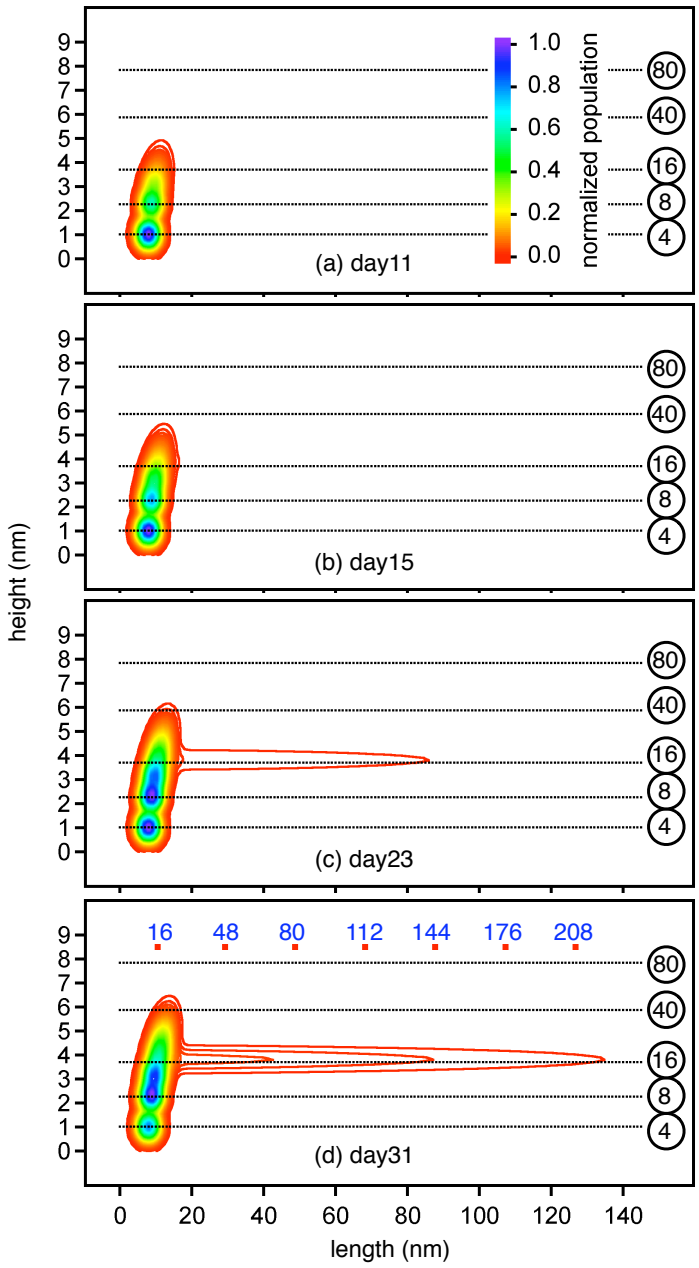

Figure 2.10: AFM height and length two-dimensional histograms constructed from kinetic simulation of Schemes 1–3. The two-dimensional histogram was constructed using Eq. 2.16 and the simulated population distribution for (a) day 11, (b) day 15, (c) day 23 and (d) day 31. The population distributions were normalized by the most populated species for that day to facilitate comparison with the experimental data. The circled numbers on the right of two-dimensional histograms give the number of monomers in globular species of corresponding heights, referring to Fig. 2.2. The red dots at the top of (d) show the number of monomers in protofibrils of corresponding length, calculated with Eq. 2.14. Both the globular and fibrillar growth patterns observed in the AFM experiments are reproduced by the simulation. This simulation captured the protofibril elongation events during growth phase. Two trends were simulated: globular assembly and fibrillar elongation.

We estimated our rate coefficients in Scheme 3 by matching the simulated height, length two-dimensional histogram with experimental data as in Fig. 2.4. As in AggB simulation, we used the same energy barrier for all the steps in protofibril elongation and used Eq. 2.24 to scale the forward rate for elongation kf_+s and reduce the number of free parameters. We used the same rate coefficients for all the disassociation reactions and found that the reverse rate was negligible.

The overall simulated height-length 2D histogram from day 11 to day 31 (Fig. 2.10) was able to reproduce our experimental data. Aggregation proceeded along the two major pathways of assembly. The range of AggB sizes increased with incubation time with the mode of the population also shifting to larger sizes. During the late lag phase, B_4 was the dominant AggB size, with a very small number of larger AggB oligomers. During the growth phase, B_8, B_{12} and B_{16} populations increased dramatically. The appearance time of protofibrils was consistent with the small number and lengths of protofibrils present on day 23 that then became abundant and long by day 31. The maximum length of protofibrils observed during the experiments was reproduced at about 150 nm. The relative population of AggB and protofibrils in the AFM (excluding B_4) was reproduced at 0.24. The population of AggB was dramatically lower above the bifurcation point, B_{16}/F_{16}.

There were also several detailed features that were not captured by our simulation. First, the size evolution of AggB did not match exactly with our data. For example, on day 23, the model over-predicted the B_{12} population (compare Fig. 2.4g to Fig. 2.10c). Our assumption that the energy barrier was the same for all steps in AggB aggregation could be an explanation of this problem. Second, a small number (approximately 3%) of particles higher than 6 nm were observed by AFM but did not appreciably populate in the simulation (Fig. 2.10g and h). These particles could be experimental artifacts from AggB and short protofibrils sitting on top of each other. Alternatively they could arise from aggregation steps involving the larger AggB aggregates. This class of reaction was not included in our final model. Third, the bundling of several protofibrils to form thicker fibrils was not considered to be important at this stage. Thus, no thicker fibrils were present in the simulation result. Fourth, we did not consider the possibility of

AggBs thicker than protofibrils converting to protofibrils as B_{16} did. The observation of particle between the two aggregation trend lines suggest this possibility, though the small population suggests a minority contribution at best. Fifth, close inspection of the protofibril length distribution in Fig. 2.4 show that there may be a local minimum of population at ∼50 nm, suggesting a local free energy maximum at this protofibril length. We have made no attempt to account for this feature as our focus is on the oligomeric species leading up to protofibrils and not the details of protofibril elongation.

Another possible mechanism was to use B_4 as the protofibrilation elongation unit, instead of A_4. The simulated fluorescence data from that model did not match our ANS measurement in the sense that the A_4 population decreased too slowly during aggregation. Our simulation also showed that monomer addition could not account for protofibril elongation in our case, because not enough monomers were around in the system to interact with the protofibril for elongation at this stage. We did not include protofibril elongation via end-to-end interactions between short protofibrils. Considering the low concentration of protofibril and their slow rate of diffusion in solution compared with A_4, the effective rate of such a reaction is likely to be very low. The remainder of the discussion focus on the mechanism with A_4 as the elongation unit.

The optimized rate constants appearing in Table 2.3 predict that there is a free energy decrease for the conversion from B_{16} to smallest amyloidogenic structure F_{16}. After optimizing the simulation, during sensitivity test we found that as long as kf_-s were smaller than 0.3, they had no effect on the simulation results. Thus the kf_- values were bracketed between 0 and 0.3. With coefficients in this range, the calculated Gibbs energy change using Eq. 2.24 was always negative, and thus the protofibril elongation steps were energetically favorable. This result implies that protofibril species can work as template to incorporate assembly units and can be used as seeds to induce fast assembly with enough assembly unit around.

kbf_+ $(\text{day})^{-1}$	kbf_- day^{-1}	kf_{16+} $(\mu\text{M day})^{-1}$	kf_{16-} day^{-1}	$\Delta G^\ddagger$ kJ/mol
0.099	0.00076	0.67	0.3*	52.3
$\Delta G^\circ = -12.5$ kJ/mol		$\Delta G^\circ \leq -2.1$ kJ/mol		

Table 2.3: Optimized rate coefficients for late lag phase simulation under Scheme 3. *This reverse rate coefficient is the upper limit; simulations were insensitive to rates below these values. The free energy change, ΔG°, is calculated based on forward and reverse rate coefficients of each step, using Eq. 2.24. $\Delta G^\ddagger$ is the energy barrier for protofibril growth steps.

2.3.3 Validation of Kinetic Model with 1-Anilino-8-naphthalene Sulfonate Data

We used qualitative aspects of the ANS data to guide the formulation of the kinetic model. We now use the kinetic simulation that was based on AFM and DLS fits to generate the evolution of the ANS fingerprints that were previously measured.[69] Thus, the ANS data provides an independent measure of the evolution of different species in solution against which we may test our overall kinetic model.

We used Eq. 2.17 with the populations of the different classes of oligomer generated by the kinetic simulations to simulate the different fluorescence contributions we previously reported.[69] The evolution of the ANS lifetime distribution fingerprints are shown in Fig. 2.11 top. By comparison the simulated contribution to the fluorescence is shown in the bottom panel. The kinetic simulation was not adjusted to match the ANS data, nor were the relative amplitudes of the different contributions adjusted. The bottom panel may also be interpreted as the amount of monomer accumulated into each species.

As in the experimental data, three stages of aggregation appeared in our simulated fingerprint evolution with the same time span. From day 0 to day 10, the dominant process was conversion of monomers to tetramers via dimers. Here we reassign the monomer fingerprint in our last paper to monomer plus both non-oxidative and oxidative dimer.

The contribution from monomer and dimers dropped dramatically as the tetramer

reached its maximum population around day 10. During this stage, a reservoir of protein made up of energetically favorable, A_2, A_2^{Ox} and A_4 accumulated before appearance of any amyloidogenic species. From day 11 to day 21, A_4 converted to AggB as shown by the anti-correlation of the two populations. Energetically unfavorable AggB accumulated in relatively smaller population than AggA before nucleation of protofibrils. After day 22, the A_4 contribution decreased while the protofibril fingerprint intensity increased accordingly and the contribution from AggB plateaued. Protein was incorporated to protofibrils via A_4.

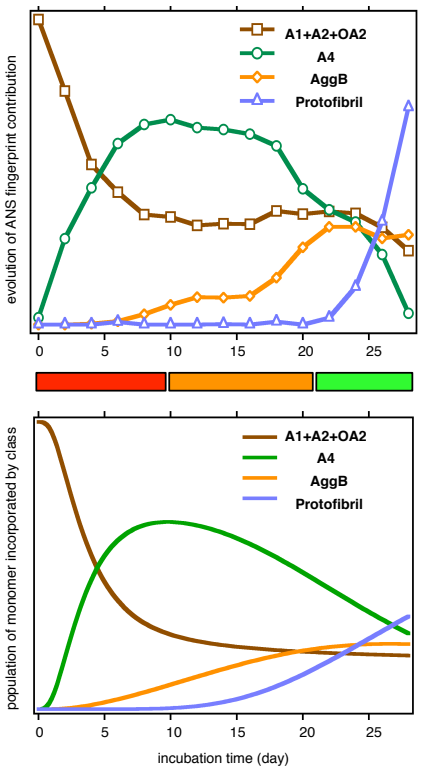

Figure 2.11: ANS fingerprint contribution was calculated as an independent validation of the kinetic model. Upper panel: experimental ANS fingerprint contribution evolution of different classes of species for 28 days of incubation. Lower panel: simulated ANS fingerprint contribution evolution based on species population from kinetic simulation, using Eq. 2.17. Three stages of growth featured by AggA, AggB and protofibril formation were captured.

One difference between the simulation and experiment fingerprint evolution was the contribution from protofibrils. The ANS lifetime measurement showed the protofibril

contribution was flat before day 20, and increased abruptly after day 21. In the simulation, this contribution was flat before day 10 and increased gradually afterwards. One possible source of this discrepancy is our omission of conversion of protofibrils to fibrils from the mechanism. Larger fibrils appear to bind ANS and ThT differently than do protofibrils. Another possibility is that the fingerprint for protofibrils should more closely resemble that of AggB. The protofibril fingerprint was generated by removing as much AggB fingerprint from the late-stage distributions as possible while maintaining non-negativity. In this case, the fingerprint for AggB would include contributions that should be attributed to protofibrils, which may account for the bi-phasic appearance of the experimental AggB fingerprint evolution.

ANS fingerprints do not give concentrations of individual species. The fingerprint is an average of the different contributions to the ANS lifetime distribution averaged over all the species included in the class of oligomer. Because the relative contribution of each size in a given oligomer class changes during incubation, the connection between a fingerprint and the overall population may not be fixed. ANS partitions amongst all its available binding sites according to their populating and binding affinities, preventing an absolute concentration of a species from being determined. Note that in spite of all these caveats, the simulated fingerprint evolution was obtained using the same proportionality constant for all species. Fig. 2.11 shows that for three of the fingerprints the evolution simulated from AFM and DLS data, the experimental ANS signals match quite well. This suggests that the different classes of aggregate have similar binding properties to the surface in the AFM experiments and to ANS in the fluorescence experiments.

2.4 Discussion

2.4.1 Aggregation Free-energy Landscape

The detailed kinetic mechanism allows us to generate an aggregation free-energy landscape under the amyloidogenic conditions of our experiments. The free energy change of each reaction, ΔG°, was calculated from Eq. 2.24 using optimized forward and reverse rate coefficients. We included the four reactions where the simulation produced only an

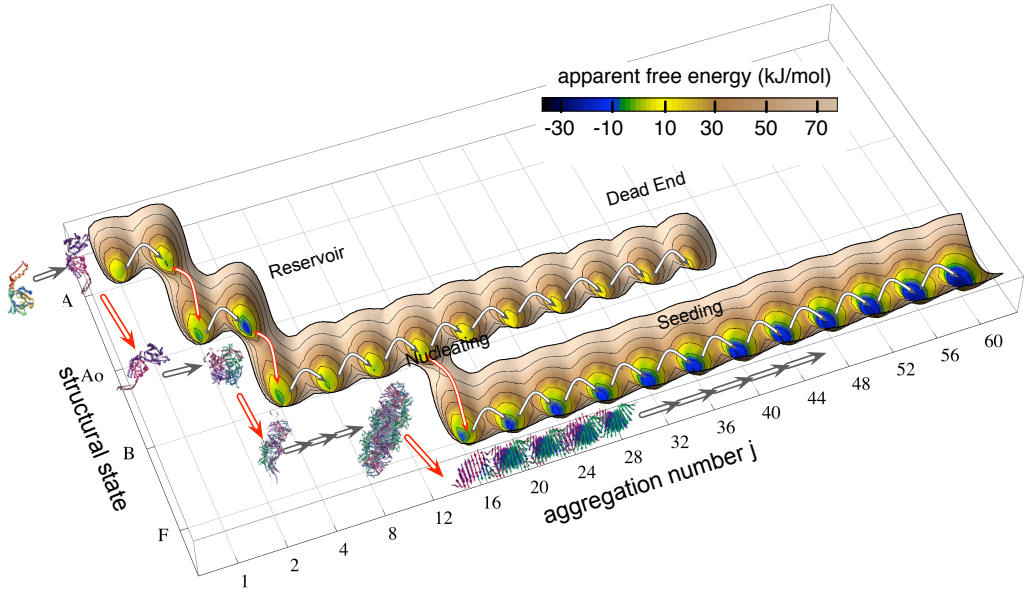

Figure 2.12: Free-energy landscape for β-LGA amyloid assembly. Assigning the origin of the free energy to be the partially unfolded monomer, the apparent free energy for AggA, AggB, and Protofibrils is plotted based on the free energy change of each reaction. The gray arrows show the path of increasing aggregation number for each class of aggregate, while the red arrows show the conformational conversions (A_2 to A_2^{Ox}, A_4 to B_4, and B_{16} to F_{16}). Four types of oligomers are identified by their location on the energy landscape and role during amyloidogenesis. Reservoir Oligomers sit at a free energy valley. The Nucleating Oligomers are the species with highest free energy along the amyloid formation pathway. Sequential assembly after nucleation of Seeding Oligomers follows a downhill trend on the energy landscape, which is the driving force for fast amyloid Protofibril elongation in the growth phase. Formation of Dead-end Oligomers has a much smaller driving force than Protofibril elongation and is off the amyloidogenic pathway.

upper limit for of the reverse rate constants (ka_{2-}, koa_-, ka_{4-} and kf_-) by considering the *least negative* ΔG° for the aggregation step in question that was supported by the data. For each of these steps the free- energy landscape could be steeper than shown in Fig. 2.12. Free energy barriers, $\Delta G^\ddagger$, were determined as a fit parameter in Eq. 2.19, which is not applicable for unimolecular reactions. For visualization purposes, barriers for $A_2 \rightarrow A_2^{Ox}$ and $A_4 \rightarrow B_4$ are shown in Fig. 2.12 with the $\Delta G^\ddagger$ for the growth reaction of the respective product species, since they should involve similar conformational

changes. Similarly, we show the energy barrier for $B_{16} \rightarrow F_{16}$ as 1.5 times that of protofibril elongation. Based on simulation, the population of B_{16} was always in excess of F_{16} (> 20 times), indicating that this step is rate-limiting compared to protofibril elongation.

Formation of AggA oligomers is energetically favorable for all steps as shown in Fig. 2.12. The accumulation of AggA in this local free energy basin at A_4 is the main characteristic of the early lag phase. Reactions in the late lag phase that form and grow AggB are uphill. Filling of the shallow free energy basin by populating AggB is the main feature of the late lag phase. There is a bifurcation in the energy landscape at B_{16}. Growth of AggB remains unfavorable above B_{16}. However, at this point formation of protofibrils becomes favorable, signaling the start of the growth phase. The lag time for β-LGA fibrillation kinetics is caused by the accumulation of AggA, the energetically unfavorable formation of B_{16} species. The net free energy increase of 15 kJ/mol for $A_4 \rightarrow B_{16}$ does not involve any bracketed rates. The sequential downhill elongation of protofibrils is the main driving force for β-LGA amyloid assembly leading to formation of mature fibrils. This aggregation free-energy landscape leads to four different behaviors for oligomers based on their kinetic relationships.

2.4.2 Species Involved in Amyloidogenesis

Reservoir Oligomers are located in a stable valley in the free-energy landscape. The dominant Reservoir Oligomer is A_4. However, other AggA species and AggB smaller than B_{16} also contribute to the pool of aggregated misfolded protein. These small oligomers accumulate at relatively larger populations during the lag phase. The pool of stable Reservoir Oligomers mediates later aggregation events. Under the amyloidogenic conditions of our experiments, Reservoir Oligomers dominate the lag phase and early growth phase. Reservoir Oligomers eventually attain a size large enough to undergo the critical conformational change to the cross-β structure of amyloid.

Nucleating Oligomers, $B_{16} \rightarrow F_{16}$, exist at the maximum free energy of intermediates along the amyloid aggregation pathway. Nucleating Oligomers do not have the stable structure of amyloid and may not have a conformational relationship to the

monomer or to other oligomers. As the species with maximum energy along amyloid formation pathway, Nucleating Oligomers are metastable and present in relatively small populations. Formation of reservoir oligomers during the pre-nucleation steps is the key feature distinguishing the proposed model in this chapter from other amyloid aggregation models, and hence this model is named reservoir-nucleation model.

Oligomers that have crossed over the barrier to the cross-β structure are **Seeding Oligomers** that mark the beginning of the amyloid fibril cascade. Protofibrils bigger than F_{16} belong to this class. Seeding oligomers can act as templates for the conformation conversion of units added to them, and thus further assembly of them is energetically favored. Addition of these Seeding Oligomers to samples under amyloidogenic conditions will reduce the length of the lag phase by incorporating Reservoir Oligomers without the need to wait for Nucleating Oligomers. Seeding Oligomers accumulate before the formation of mature fibrils and dominate the growth phase. Isolating small Seeding Oligomers would require manipulating experimental conditions to alter the free-energy landscape so as to limit the elongation of protofibrils or to induce fragmentation of larger protofibrils.

We designate AggB oligomers larger than B_{16} as **Dead-End Oligomers**. They are formed by continued growth of Reservoir Oligomers without converting to amyloid structure. Dead-End Oligomers are uphill and off-pathway from amyloid; under the amyloidogenic conditions they remained in small populations. Isolating Dead-End Oligomers would require manipulating experimental conditions to prevent the nucleation step ($B_{16} \rightarrow F_{16}$) from occurring.

2.4.3 Relationship to Other Kinetic Models

The free-energy landscape provides insight and a common framework for discussion and comparison of the present model to other common models of amyloidogenesis. The chief feature of a nucleated polymerization model is sequential energetically unfavorable aggregation to form a nucleus of critical size.[52] Polymerization is favorable above this critical size. This model precludes the accumulation of a pool of oligomers in a local free energy minimum.

The Lumry-Eyring nucleated polymerization (LENP) model is a generalization of many simpler nucleation-growth models.[84] LENP includes five stages of growth and has some superficial similarities to our model. However, there are several important differences. Our study focused on the phase after conformational changes of unaggregated protein and before the condensation of higher-order assembly. In LENP this stage is modeled as pre-nucleation, nucleation and growth of soluble aggregates via polymerization. The LENP pre-nucleation steps are comparable with our AggB formation. However, the Reservoir Oligomer is missing in the LENP model. The nucleation step in LENP is the irreversible rearrangement of an oligomer to amyloidogenic form, implying a large decrease in free energy. Our model showed only modest free energy changes for the conformational conversion steps and the formation of smallest amyloid species, F_{16}. In LENP amyloid growth is by monomer addition; in our model they elongate by incorporating Reservoir Oligomers. Finally, we explicitly compare the populations of the different species present in our model to experimental data rather than calculating averaged relaxation behavior.

The micelle nucleation model assumes an all-or-nothing aggregation to form micelles.[83,53] Though, micelle formation may not be as sharp in proteins as in traditional surfactants. We did not observe the cooperativity required for this model. However, there are some important similarities between our model and that of Lomakin *et al.* The micelle acts as a Reservoir Oligomer above the critical micelle concentration (CMC). The amphiphilic nature of proteins makes the formation of micelle-like structures a reasonable model. A CMC also suggests a limit to the size of a colloidal protein aggregate. The micelle nucleation requires that the Reservoir and Nucleating Oligomers be the same. Amyloid growth is only by monomer addition.

The nucleated conformational conversion model (NCC) for Sup35 amyloid assembly can fit into our picture in some aspects.[54,99] Lag phase oligomers of Sup35 formed a reservoir and mediated fibril elongation, similar to AggA. The Sup35 experiments did not identify any other intermediates. In NCC the Reservoir and Nucleating Oligomers are the same size. In our model, nucleation occurs through a larger and rarer intermediate.

We considered the possibility of AggB aggregation through addition of B_4 instead of A_4. Because A_4 and B_4 were in equilibrium with each other, the simulation results were indistinguishable from these two mechanisms. The parameters for growth by B_4 addition gave downhill aggregation implying no limit to AggB sizes. The globular aggregate height was limited to ~9 nm implying uphill aggregation by A_4. However, AggB size may be kinetically controlled by fibril formation.

2.4.4 Prediction of Seeding Effect by Reservoir-nucleation Model

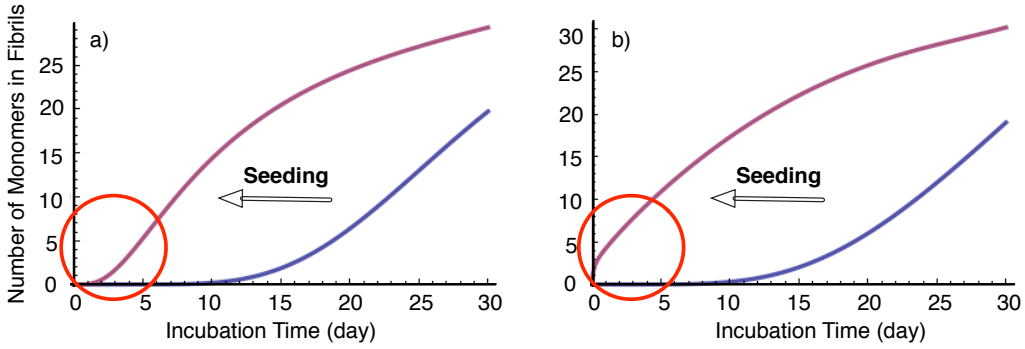

Figure 2.13: Comparison of seeding effect predicted by reservoir-nucleation model and nucleated polymerization model. Protofibrils on day 30 was used as seeds. a) Seeding effect predicted by reservoir-nucleation model in this chapter. b) Seeding effect predicted by nucleated polymerization model. Both models predicted the acceleration of the kinetics by seeding, but gave quite different seeded kinetic profiles, especially at the beginning of the incubation as shown in the red circles. The major difference was on the lag time and the initial rate after seeding.

Fig. 2.13a shows a simulated seeding experiment under experimental conditions used in this chapter. With the same kinetic parameters presented before, the population of protofibrils on day 30 was used as the protofibril initial concentration in a new run of simulation. This simulated the experiment in which protofibrils were collected on day 30 and used to seed a new incubation. The reservoir-nucleation model predicted that the lag time was substantially shortened but not completely eliminated. The initial growth rate increased compared with the unseeded incubation. Along the seeded kinetic profile, the growth rate first increased, and then decreased. An inflection point was observed.

Fig. 2.13b shows the simulated kinetic profile for the nucleated polymerization model, in which each aggregation step involves the addition of a monomer. This model predicted a complete elimination of the lag phase in the seeded profile. The initial growth rate was the maximum rate along the kinetic profile and the rate decreased monotonically as a result of decreased monomer concentration. There was no point of inflection in the seeded profile.

Jarrett and Lansbury discussed the seeding behavior of amyloid aggregation, but did not show actual experimental data.[52] Published data on amyloid seeding studies almost always resembles the seeded profile on the left, as predicted by the reservoir-nucleation model. Colby et al. used preformed fibrils and different preparation of prions to seed amyloid formation. None of their seeding experiments actually showed completely elimination of the lag phase. The lag phase were shorten to different extents, and the shape of seeded kinetic profile matched the one predicted by the reservoir-nucleation model.[100] Baskakov et al. also showed that the lag phase were shortened but not eliminated with different concentration of seeds for a recombinant prion protein, rPrP89-230, amyloid formation. Again, the shape of the seeded profile followed the prediction on the left.[101] Even for many seeding experiments that claimed complete elimination of the lag phase, the seeded kinetic profile were more like Fig. 2.13a than Fig. 2.13b.[80] The seeded kinetic profiles started with a slower initial growth rate rather than a faster initial growth rate and had an inflection point. Padrick et al. found that the lag phase of islet amyloid polypeptide (IAPP) amyloid formation was completely bypassed with 5% seeds (by mass). However, the seeded kinetic profile started with a slower initial growth rate and then increased, showing an inflection point along the population profile. By incubating the protein for 30 minutes before adding seeds, this inflection point could be removed and the seeded kinetic profile looked more like the nucleated polymerization in Fig. 2.13b.[80] Consistent with the reservoir-nucleation model, this observation can be explained by a fast (<30 min) equilibrium between monomers and reservoir species.

2.4.5 Roles of Oligomers in Amyloid Hypotheses

The presence of amyloid aggregates defines the entire class of amyloid-related diseases. Because production of amyloid is so often observed during disease progression, any suspected toxic species should be present under the physiological conditions that produce amyloid. To play a role in the disease, aggregates must be cytotoxic and stable enough to accumulate under the disease-relevant amyloidogenic conditions. Experimental tests of the amyloid cascade and toxic oligomer hypothesis mainly evaluate the first requirement of toxicity. The two hypotheses have differing free-energy landscape requirements.

The amyloid cascade hypothesis states that accumulation of autocatalytic amyloid fibrils and plaques cause the defects in amyloid-related disease.[15] The free-energy landscape picture provides restrictions on this hypothesis. First, the reservoir must fill to the point that Nucleating Oligomers are formed to allow creation of Seeding Oligomers. Second, Reservoir Oligomers must accumulate in sufficient numbers to support elongation of protofibrils. Thus, two classes of oligomers are relevant to disease progression under the amyloid cascade hypothesis: Seeding Oligomers and Reservoir Oligomers. Single amino acid mutations that increase the rate of amyloid formation often increase rate of disease progression.[10,42,43] This suggests that the mutations must either increase the depth of the reservoir and/or decrease the barrier to nucleation. An increase in cross-β propensity would stabilize the amyloid product but not increase the rate of amyloid formation unless the transition state at the nucleation step resembles cross-β. This idea can explain the inconsistency of secondary structure prediction of amyloid-prone sequences. A net kinetic effect will appear only if the nucleation barrier is reduced or the population of the Reservoir Oligomers is increased.

The Reservoir Oligomers are required for elongation of amyloid protofibrils. Therefore assays of toxicity of Seeding Oligomers when a pool of Reservoir Oligomers is not also present do not strictly evaluate the validity of the amyloid cascade hypothesis. Seeding experiments often show that the lag phase is greatly reduced but not completely eliminated as would be expected for a simple nucleation model. Under

seeded conditions, the rate-determining step may be reformation of the pool of Reservoir Oligomers. The downhill landscape after the formation of Nucleating Oligomers assures the stability and accumulation of Seeding Oligomers and long protofibrils, which are the dominant diagnostic species in most investigations of amyloidogenesis. If this is true, then it is critical to prevent formation of Nucleating and Seeding Oligomers.

The free-energy landscape picture also provides restrictions on the toxic oligomer hypothesis. Small toxic oligomers must exist at local free energy minima with significant barriers to amyloid formation; that is, they must be Reservoir Oligomers. Thus, kinetic mechanisms that imply local minima at only the monomer and fibril locations on the aggregation free-energy landscape are incompatible with the toxic oligomer hypothesis.

The small oligomers used to assay toxicity have many morphologies as they arise from many different, often physiologically impossible, preparation conditions. The different preparation conditions likely constrain the aggregation to oligomers that may be unstable or impossible under amyloidogenic conditions. No attempt is usually made to place the oligomers into the context of amyloidogenic aggregation. As a result any combination of kinetic roles may be active in the assayed samples.

The toxic oligomer hypothesis cannot, on its own, explain why amyloid is observed in amyloid-related diseases. Nor can it explain the correlation between single amino acid mutations that increase amyloid propensity and the onset and severity of disease-related symptoms. This coincidence of the toxicity of small oligomers and their amyloidogenic properties can be explained with our mechanism. To form amyloid fibrils, which are the ultimate indicators of amyloidogenesis, Reservoir Oligomers must be present under amyloidogenic conditions. The rate of growth of amyloid protofibrils is controlled by the concentration of the Reservoir Oligomers. If the Reservoir Oligomers are also intrinsically toxic, this can explain the coincidence between the progression of disease and the presence of amyloid, as both depend on the concentration of the Reservoir Oligomers. It also explains the effects of single amino acid mutations if such changes increase the population of the Reservoir Oligomers.

Identification of targets for therapeutics depends on the nature of the aggregation

free-energy landscape. Therapeutic intervention relies on the inhibition or acceleration of particular reactions, which can be accomplished by increasing or decreasing the barriers on the aggregation free-energy landscape. For example, β-LGA monomer is stabilized by the binding of an appropriate ligand, which increases the barrier to aggregation. Another approach is to open new reaction pathways to important species on the aggregation free-energy landscape. Our mechanism suggests that the formation of Reservoir Oligomers is a key feature in both of the dominant amyloid-disease hypotheses. Reservoirs Oligomers are accordingly the best target during therapeutic design. For example, toxic species could be cleared by converting them to innocuous species. However, inhibiting fibril formation might enhance the population of Reservoir Oligomers and enhance toxicity if the toxic oligomer hypothesis is correct. Other therapeutic interventions could have similar unintended consequences because of the details of the aggregation free-energy landscape.

Bibliography

[1] F. Chiti and C. M. Dobson. Protein misfolding, functional amyloid, and human disease. *Annu. Rev. Biochem.*, 75:333–366, 2006.

[2] D. J. Selkoe. Folding proteins in fatal ways. *Nature*, 426:900–904, 2003.

[3] M. B. Pepys. Pathogenesis, diagnosis and treatment of systemic amyloidosis. *Philos. Trans. R. Soc. Ser. B*, 356:203–211, 2001.

[4] M. B. Pepys. Amyloidosis. *Annu. Rev. Med.*, 57:223–241, 2006.

[5] M. H. Polymeropoulos, C. Lavedan, E. Leroy, S. E. Ide, A. Dehejia, A. Dutra, B. Pike, H. Root, J. Rubenstein, R. Boyer, E. S. Stenroos, S. Chandrasekharappa, A. Athanassiadou, T. Papapetropoulos, W. G. Johnson, A. M. Lazzarini, R. C. Duvoisin, G. Di Iorio, L. I. Golbe, and R. L. Nussbaum. Mutation in the α-synuclein gene identified in families with Parkinson's disease. *Science*, 276(5321):2045–2047, 1997.

[6] R. Krger, W. Kuhn, T. Mller, D. Woitalla, M. Graeber, S. Ksel, H. Przuntek, J. T. Epplen, L. Schls, and O. Riess. Ala30Pro mutation in the gene encoding α-synuclein in Parkinson's disease. *Nat. Genet.*, 18(2):106–108, 1998.

[7] J. J. Zarranz, J. Alegre, J. C. Gmez-Esteban, E. Lezcano, R. Ros, I. Ampuero, L. Vidal, J. Hoenicka, O. Rodriguez, B. Atars, V. Llorens, E. G. Tortosa, T. del Ser, D. G. Muoz, and J. G. de Yebenes. The new mutation, E46K, of α-synuclein causes Parkinson and Lewy body dementia. *Ann. Neurol.*, 55(2):164–173, 2004.

[8] Y. Mizuno, N. Hattori, S. Kubo, S. Sato, K. Nishioka, T. Hatano, H. Tomiyama, M. Funayama, Y. Machida, and H. Mochizuki. Progress in the pathogenesis

and genetics of Parkinson's disease. *Philos. Trans. R. Soc. Lond. B Biol. Sci.*, 363(1500):2215–2227, 2008.

[9] A. B. Singleton, M. Farrer, J. Johnson, A. Singleton, S. Hague, J. Kachergus, M. Hulihan, T. Peuralinna, A. Dutra, R. Nussbaum, S. Lincoln, A. Crawley, M. Hanson, D. Maraganore, C. Adler, M. R. Cookson, M. Muenter, M. Baptista, D. Miller, J. Blancato, J. Hardy, and K. Gwinn-Hardy. α-Synuclein locus triplication causes Parkinson's disease. *Science*, 302(5646):841, 2003.

[10] K. A. Conway, J. D. Harper, and P. T. Lansbury. Accelerated in vitro fibril formation by a mutant α-synuclein linked to early-onset Parkinson disease. *Nat. Med.*, 4(11):1318–1320, 1998.

[11] M. K. Lee, W. Stirling, Y. Xu, X. Xu, D. Qui, A. S. Mandir, T. M. Dawson, N. G. Copeland, N. A. Jenkins, and D. L. Price. Human α-synuclein-harboring familial Parkinson's disease-linked Ala-53-Thr mutation causes neurodegenerative disease with α-synuclein aggregation in transgenic mice. *Proc. Natl. Acad. Sci. U. S. A.*, 99(13):8968–8973, 2002.

[12] K. Iijima, H. Chiang, S. A. Hearn, I. Hakker, A. Gatt, C. Shenton, L. Granger, A. Leung, K. Iijima-Ando, and Y. Zhong. Aβ42 mutants with different aggregation profiles induce distinct pathologies in Drosophila. *PLoS ONE*, 3(2):e1703, 2008.

[13] J. Meinhardt, G. G. Tartaglia, A. Pawar, T. Christopeit, P. Hortschansky, V. Schroeckh, C. M. Dobson, M. Vendruscolo, and M. Fndrich. Similarities in the thermodynamics and kinetics of aggregation of disease-related Aβ(1-40) peptides. *Protein Sci.*, 16(6):1214–1222, 2007.

[14] B. Caughey and P. T. Lansbury. Protofibrils, pores, fibrils, and neurodegeneration: separating the responsible protein aggregates from the innocent bystanders. *Annu. Rev. Neurosci.*, 26:267–298, 2003.

[15] J. A. Hardy and G. A. Higgins. Alzheimer's disease: the amyloid cascade hypothesis. *Science*, 256:184–5, 1992.

[16] E. Karran, M. Mercken, and B. De Strooper. The amyloid cascade hypothesis for Alzheimer's disease: an appraisal for the development of therapeutics. *Nat. Rev. Drug Discov.*, 10(9):698–712, 2011.

[17] P. L. McGeer and E. G. McGeer. The inflammatory response system of brain: implications for therapy of Alzheimer and other neurodegenerative diseases. *Brain Res. Brain Res. Rev.*, 21(2):195–218, 1995.

[18] P. Eikelenboom and R. Veerhuis. The role of complement and activated microglia in the pathogenesis of Alzheimer's disease. *Neurobiol. Aging*, 17(5):673–680, 1996.

[19] C. J. Pike, A. J. Walencewicz, C. G. Glabe, and C. W. Cotman. Aggregation-related toxicity of synthetic β-amyloid protein in hippocampal cultures. *Eur. J. Pharmacol.*, 207(4):367–368, 1991.

[20] A. Lorenzo and B. A. Yankner. β-Amyloid neurotoxicity requires fibril formation and is inhibited by Congo red. *Proc. Natl. Acad. Sci. U. S. A.*, 91:12243–7, 1994.

[21] L. Mucke, E. Masliah, G. Q. Yu, M. Mallory, E. M. Rockenstein, G. Tatsuno, K. Hu, D. Kholodenko, K. Johnson-Wood, and L. McConlogue. High-level neuronal expression of Aβ 1-42 in wild-type human amyloid protein precursor transgenic mice: synaptotoxicity without plaque formation. *J. Neurosci.*, 20(11):4050–4058, 2000.

[22] J. C. Dodart, K. R. Bales, K. S. Gannon, S. J. Greene, R. B. DeMattos, C. Mathis, C. A. DeLong, S. Wu, X. Wu, D. M. Holtzman, and S. M. Paul. Immunization reverses memory deficits without reducing brain Aβ burden in Alzheimer's disease model. *Nat. Neurosci.*, 5(5):452–457, 2002.

[23] J. J. Meier, R. Kayed, C. Lin, T. Gurlo, L. Haataja, S. Jayasinghe, R. Langen, C. G. Glabe, and P. C. Butler. Inhibition of human IAPP fibril formation does not prevent β-cell death: evidence for distinct actions of oligomers and fibrils of human IAPP. *Am. J. Physiol. Endocrinol. Metab.*, 291(6):E1317–E1324, 2006.

[24] L. Lue, Y. Kuo, A. E. Roher, L. Brachova, Y. Shen, L. Sueand, T. Beach, J. H. Kurth, R. E. Rydel, and J. Rogers. Soluble amyloid β peptide concentration as a predictor of synaptic change in Alzheimer's disease. *Am. J. Pathol.*, 155:853–62., 1999.

[25] C. A. McLean, R. A. Cherny, F. W. Fraser, S. J. Fuller, M. J. Smith, K. Beyreuther, A. I. Bush, and C. L. Masters. Soluble pool of Aβ amyloid as a determinant of severity of neurodegeneration in Alzheimer's disease. *Ann. Neurol.*, 46:860–866, 1999.

[26] W. L. Klein, G. A. Krafft, and C. E. Finch. Targeting small Aβ oligomers: the solution to an Alzheimer's disease conundrum? *Trends Neurosci.*, 24:219–224, 2001.

[27] M. D. Kirkitadze, G. Bitan, and D. B. Teplow. Paradigm shifts in Alzheimer's disease and other neurodegenerative disorders: the emerging role of oligomeric assemblies. *J. Neurosci. Res.*, 69:567–577, 2002.

[28] W. L. Klein, W. B. Klein, and D. B. Teplow. Small assemblies of unmodified amyloid β-protein are the proximate neurotoxin in Alzheimer's disease. *Neurobiol. Aging*, 25:569–580, 2004.

[29] D. C. Crowther, K. J. Kinghorn, E. Miranda, R. Page, J. A. Curry, F. A. I. Duthie, D. C. Gubb, and D. A. Lomas. Intraneuronal Aβ, non-amyloid aggregates and neurodegeneration in a Drosophila model of Alzheimer's disease. *Neuroscience*, 132(1):123–135, 2005.

[30] J. P. Cleary, D. M. Walsh, J. J. Hofmeister, G. M. Shankar, M. A. Kuskowski, D. J. Selkoe, and K. H. Ashe. Natural oligomers of the amyloid β-protein specifically disrupt cognitive function. *Nat. Neurosci.*, 8(1):79–84, 2005.

[31] S. T. Ferreira, M. N. N. Vieira, and F. G. Felice. Soluble protein oligomers as emerging toxins in Alzheimer's and other amyloid diseases. *IUBMB Life*, 59(4-5):332–345, 2007.

[32] S. Dennis. Soluble oligomers of the amyloid β-protein impair synaptic plasticity and behavior. *Behav. Brain Res.*, 192:106–113, 2008.

[33] J. Laurn, D. A. Gimbel, H. B. Nygaard, J. W. Gilbert, and S. M. Strittmatter. Cellular prion protein mediates impairment of synaptic plasticity by amyloid-β oligomers. *Nature*, 457(7233):1128–1132, 2009.

[34] D. M. Walsh, I. Klyubin, J. V. Fadeeva, W. K. Cullen, R. Anwyl, M. S. Wolfe, M. J. Rowan, and D. J. Selkoe. Naturally secreted oligomers of amyloid β protein potently inhibit hippocampal long-term potentiation in vivo. *Nature*, 416(6880):535–539, 2002.

[35] B. A. Chromy, R. J. Nowak, M. P. Lambert, K. L. Viola, L. Chang, P. T. Velasco, B. W. Jones, S. J. Fernandez, P. N. Lacor, P. Horowitz, C. E. Finch, G. A. Krafft, and W. L. Klei. Self-assembly of Aβ 1-42 into globular neurotoxins. *Biochemistry*, 42:12749–12760, 2003.

[36] R. Kayed, Y. Sokolov, B. Edmonds, T. M. McIntire, S. C. Milton, J. E. Hall, and C. G. Glabe. Permeabilization of lipid bilayers is a common conformation-dependent activity of soluble amyloid oligomers in protein misfolding diseases. *J. Biol. Chem.*, 279(45):46363–46366, 2004.

[37] A. Demuro, E. Mina, R. Kayed, S. C. Milton, I. Parker, and C. G. Glabe. Calcium dysregulation and membrane disruption as a ubiquitous neurotoxic mechanism of soluble amyloid oligomers. *J. Biol. Chem.*, 280(17):17294–17300, 2005.

[38] R. Carrotta, M. Di Carlo, M. Manno, G. Montana, P. Picone, D. Romancino, and P. L. San Biagio. Toxicity of recombinant β-amyloid prefibrillar oligomers on the morphogenesis of the sea urchin Paracentrotus lividus. *FASEB J.*, 20(11):1916–1917, 2006.

[39] K. M. Danzer, D. Haasen, A. R. Karow, S. Moussaud, M. Habeck, A. Giese, H. Kretzschmar, B. Hengerer, and M. Kostka. Different species of α-synuclein oligomers induce calcium influx and seeding. *J. Neurosci.*, 27(34):9220–9232, 2007.

[40] M. Bucciantini, E. Giannoni, F. Chiti, F. Baroni, L. Formigli, J. Zurdo, N. Taddei, G. Ramponi, C. M. Dobson, and M. Stefani. Inherent toxicity of aggregates implies a common mechanism for protein misfolding diseases. *Nature*, 416(6880):507–511, 2002.

[41] G. Bitan, E. A. Fradinger, S. M. Spring, and D. B. Teplow. Neurotoxic protein oligomers–what you see is not always what you get. *Amyloid*, 12(2):88–95, 2005.

[42] L. Narhi, S. J. Wood, S. Steavenson, Y. Jiang, G. M. Wu, D. Anafi, S. A. Kaufman, F. Martin, K. Sitney, P. Denis, J. C. Louis, J. Wypych, A. L. Biere, and M. Citron. Both familial Parkinson's disease mutations accelerate α-synuclein aggregation. *J. Biol. Chem.*, 274(14):9843–9846, 1999.

[43] E. A. Greenbaum, C. L. Graves, A. J. Mishizen-Eberz, M. A. Lupoli, D. R. Lynch, S. W. Englander, P. H. Axelsen, and B. I. Giasson. The E46K mutation in α-synuclein increases amyloid fibril formation. *J. Biol. Chem.*, 280(9):7800–7807, 2005.

[44] D. Watson, E. Castano, T. A. Kokjohn, Y. Kuo, Y. Lyubchenko, D. Pinsky, E. S. Connoll, C. Esh, D. C. Luehrs, W. B. Stine, L. M. Rowse, M. R. Emmerling, and A. E. Roher. Physicochemical characteristics of soluble oligomeric Aβ and their pathologic role in Alzheimer's disease. *Neurol. Res.*, 27:869–881, 2005.

[45] D. M. Walsh, D. M. Hartley, Y. Kusumoto, Y. Fezoui, M. M. Condron, A. Lomakin, G. B. Benedek, D. J. Selkoe, and D. B. Teplow. Amyloid β-protein fibrillogenesis. structure and biological activity of protofibrillar intermediates. *J. Biol. Chem.*, 274:25945–25952, 1999.

[46] K. A. Conway, J. D. Harper, and P. T. J. Lansbury. Fibrils formed in vitro from α-synuclein and two mutant forms linked to Parkinson's disease are typical amyloid. *Biochemistry*, 39:2552–2563, 2000.

[47] G. Bitan, A. Lomakin, and D. B.Teplow. Amyloid-β protein oligomerization: prenucleation interactions revealed by photo-induced cross-linking of unmodified proteins. *J. Biol. Chem.*, 276:35176–35184, 2001.

[48] A. J. Modler, K. Gast, G. Lutsch, and G. Damaschun. Assembly of amyloid protofibrils via critical oligomers-a novel pathway of amyloid formation. *J. Mol. Biol.*, 325:135–148, 2003.

[49] M. M. Apetri, N. C. Maiti, M. G. Zagorski, P. R. Carey, and V. E. Anderson. Secondary structure of α-synuclein oligomers: characterization by raman and atomic force microscopy. *J. Mol. Biol.*, 355(1):63–71, 2006.

[50] A. Podest, G. Tiana, P. Milani, and M. Manno. Early events in insulin fibrillization studied by time-lapse atomic force microscopy. *Biophys. J.*, 90(2):589–597, 2006.

[51] A. Natalello, V. V. Prokorov, F. Tagliavini, M. Morbin, G. Forloni, M. Beeg, C. Manzoni, L. Colombo, M. Gobbi, M. Salmona, and S. M. Doglia. Conformational plasticity of the Gerstmann-Straeussler-Scheinker disease peptide as indicated by its multiple aggregation pathways. *J. Mol. Biol.*, 381:1349–1361, 2008.

[52] J. T. Jarrett and P. T. J. Lansbury. Seeding "one-dimensional crystallization" of amyloid: A pathogenic mechanism in Alzheimer's disease and scrapie? *Cell*, 73:1055–1058, 1993.

[53] A. Lomakin, D. S. Chung, G. B. Benedek, D. A. Kirschner, and D. B. Teplow. On the nucleation and growth of amyloid β-protein fibrils: Detection of nuclei and quantitation of rate constants. *Proc. Natl. Acad. Sci. U. S. A.*, 93(3):1125–1129, 1996.

[54] T. R. Serio, A. G. Cashikar, A. S. Kowal, G. J. Sawicki, J. J. Moslehi, L. Serpell, M. F. Arnsdorf, and S. L. Lindquist. Nucleated conformational conversion and the replication of conformational information by a prion determinant. *Science*, 289:1317–1321, 2000.

[55] J. J. M. Hoozemans, R. Veerhuis, E. S. Van Haastert, J. M. Rozemuller, F. Baas, P. Eikelenboom, and W. Scheper. The unfolded protein response is activated in Alzheimer's disease. *Acta Neuropathol.*, 110(2):165–172, 2005.

[56] M. J. Volles and P. T. Lansbury. Vesicle permeabilization by protofibrillar α-synuclein is sensitive to Parkinson's disease-linked mutations and occurs by a pore-like mechanism. *Biochemistry*, 41(14):4595–4602, 2002.

[57] B. L. Kagan, R. Azimov, and R. Azimova. Amyloid peptide channels. *J. Membr. Biol.*, 202(1):1–10, 2004.

[58] N. H. Varvel, K. Bhaskar, A. R. Patil, S. W. Pimplikar, K. Herrup, and B. T. Lamb. Aβ oligomers induce neuronal cell cycle events in Alzheimer's disease. *J. Neurosci.*, 28(43):10786–10793, 2008.

[59] V. Narayanan and S. Scarlata. Membrane binding and self-association of α-synucleins. *Biochemistry*, 40(33):9927–9934, 2001.

[60] M. Zhu, P. O. Souillac, C. Ionescu-Zanetti, S. A. Carter, and A. L. Fink. Surface-catalyzed amyloid fibril formation. *J. Biol. Chem.*, 277(52):50914–50922, 2002.

[61] M. Zhu and A. L. Fink. Lipid binding inhibits α-synuclein fibril formation. *J. Biol. Chem.*, 278(19):16873–16877, 2003.

[62] J. Pronchik, X. He, J. T. Giurleo, and D. S. Talaga. In vitro formation of amyloid from α-synuclein is dominated by reactions at hydrophobic interfaces. *J. Am. Chem. Soc.*, 132:9797–9803, 2010.

[63] V. Sluzky, J. A. Tamada, A. M. Klibanov, and R. Langer. Kinetics of insulin aggregation in aqueous solutions upon agitation in the presence of hydrophobic surfaces. *Proc. Natl. Acad. Sci. U. S. A.*, 88(21):9377–9381, 1991.

[64] D. Jiang, K. L. Dinh, T. C. Ruthenburg, Y. Zhang, L. Su, D. P. Land, and F. Zhou. A kinetic model for β-amyloid adsorption at the air/solution interface and its implication to the β-amyloid aggregation process. *J. Phys. Chem. B*, 113(10):3160–3168, 2009.

[65] M. Ramirez-Alvarado, J. S. Merkel, and L. Regan. A systematic exploration of the influence of the protein stability on amyloid fibril formation in vitro. *Proc. Natl. Acad. Sci. U. S. A.*, 97(16):8979–8984, 2000.

[66] S. R. Collins, A. Douglass, R. D. Vale, , and J. S. Weissman. Mechanism of prion propagation: amyloid growth occurs by monomer addition. *PLoS Biology*, 2:1582–1590, 2004.

[67] G. Bitan, M. D. Kirkitadze, A. Lomakin, S. S. Vollers, G. B. Benedek, , and D. B. Teplow. Amyloid-β protein (Aβ) assembly: Aβ40 and Aβ42 oligomerize through distinct pathways. *Proc. Natl. Acad. Sci. U. S. A.*, 100:330–335, 2003.

[68] A. R. Hurshman, J. T. White, E. T. Powers, and J. W. Kelly. Transthyretin aggregation under partially denaturing conditions is a downhill polymerization. *Biochemistry*, 43:7365–7381, 2004.

[69] J. T. Giurleo, X. He, and D. S. Talaga. β-Lactoglobulin assembles into amyloid through sequential aggregated intermediates. *J. Mol. Biol.*, 381:1332–1348, 2008.

[70] W. S. Gosal, S. L. Myers, S. E. Radford, and N. H.Thomson. Amyloid under the atomic force microscope. *Protein Pept. Lett.*, 13:261–270, 2006.

[71] N. M. Kad, S. L. Myers, D. P. Smith, D. A. Smith, S. E. Radford, and N. H. Thomson. Hierarchical assembly of β 2-microglobulin amyloid in vitro revealed by atomic force microscopy. *J. Mol. Biol.*, 330:785–797, 2003.

[72] K. N. Dahlgren, A. M. Manelli, W. B. J. Stine, L. K. Baker, G. A. Krafft, and M. J. LaDu. Oligomeric and fibrillar species of amyloid-β peptides differentially affect neuronal viability. *J. Biol. Chem.*, 277:32046–32053, 2002.

[73] W. B.Stien, K. N. Dahlgren, G. A. Krafft, and M. J. LaDu. In vitro characterization of conditions for amyloid-β peptide oligomerization and fibrillogenesis. *J. Biol. Chem.*, 278:11612–11622, 2003.

[74] J. Green, C. Goldsbury, T. Mini, S. Sunderji, P. Frey, J. Kistler, G. Cooper, and U. Aebi. Full-length rat amylin forms fibrils following substitution of single residues from human amylin. *J. Mol. Biol.*, 326:1147–1156, 2003.

[75] J. D. Harper, S. S. Wong, C. M. Lieber, and P. T. J. Lansbury. Assembly of Aβ

amyloid protofibrils: An in vitro model for a possible early event in Alzheimer's disease. *Biochemistry*, 38:8972–8980, 1999.

[76] W. S. Gosal, A. H. Clark, and S. B. Ross-Murphy. Fibrillar β-lactoglobulin gels: Part 1. fibril formation and structure. *Biomacromolecules*, 5:2408–2419, 2004.

[77] S. Xu, B. Bevis, and M. F. Arnsdorf. The assembly of amyloidogenic yeast Sup35 as assessed by scanning (atomic) force microscopy: an analogy to linear colloidal aggregation? *Biophys. J.*, 81:446–454, 2001.

[78] J. D. Harper, S. S. Wong, C. M. Lieber, and P. T. J. Lansbury. Observation of metastable Aβ amyloid protofibrils by atomic force microscopy. *Chem. Biol.*, 4:119–125, 1997.

[79] T. T. Ding, S. Lee, J. C. Rochet, and P. T. J. Lansbury. Annular α-synuclein protofibrils are produced when spherical protofibrils are incubated in solution or bound to brain-derived membranes. *Biochemistry*, 41:10209–10217, 2002.

[80] S. B. Padrick and A. D. Miranker. Islet amyloid: phase partitioning and secondary nucleation are central to the mechanism of fibrillogenesis. *Biochemistry*, 41:4694–4703, 2002.

[81] R. Kayed, E. Head, J. L. Thompson, T. M. McIntire, S. C. Milton, C. W. Cotman, and C. G. Glabe. Common structure of soluble amyloid oligomers Implies common mechanism of pathogenesis. *Science*, 300:486–489, 2003.

[82] E. T. Powers and D. L. Powers. Mechanisms of protein fibril formation: nucleated polymerization with competing off-pathway aggregation. *Biophys. J.*, 94:379–391, 2008.

[83] A. Lomakin, D. B. Teplow, D. A. Kirschner, and G. B. Benedek. Kinetic theory of fibrillogenesis of amyloid β-protein. *Proc. Natl. Acad. Sci. U. S. A.*, 94:7942–7947, 1997.

[84] J. M. Andrews and C. J. Roberts. A Lumry-Eyring nucleated polymerization

model of protein aggregation kinetics: 1. Aggregation with pre-equilibrated unfolding. *J. Phys. Chem. B*, 111(27):7897–7913, 2007.

[85] L. Sawyer and G. Kontopidis. The core lipocalin, bovine β-lactoglobulin. *Biochim. Biophys. Acta.*, 1482(1-2):136–148, 2000.

[86] G. Kontopidis, C. Holt, and L. Sawyer. Invited review: β-lactoglobulin: binding properties, structure, and function. *J. Dairy Sci.*, 87(4):785–796, 2004.

[87] S. Uhrnov, M. H. Smith, G. B. Jameson, D. Uhrn, L. Sawyer, and P. N. Barlow. Structural changes accompanying pH-induced dissociation of the β-lactoglobulin dimer. *Biochemistry*, 39(13):3565–3574, 2000.

[88] L. D'Alfonso, M. Collini, and G. Baldini. Evidence of heterogeneous 1-anilinonaphthalene-8-sulfonate binding to β-lactoglobulin from fluorescence spectroscopy. *Biochim. Biophys. Acta*, 1432(2):194–202, 1999.

[89] M. Collini, L. D'Alfonso, and G. Baldini. New insight on β-lactoglobulin binding sites by 1-anilinonaphthalene-8-sulfonate fluorescence decay. *Protein Sci.*, 9(10):1968–1974, 2000.

[90] R. Carrotta, R. Bauer, R. Waninge, and C. Rischel. Conformational characterization of oligomeric intermediates and aggregates in β-lactoglobulin heat aggregation. *Protein Sci.*, 10(7):1312–1318, 2001.

[91] D. Hamada and C. M. Dobson. A kinetic study of β-lactoglobulin amyloid fibril formation promoted by urea. *Protein Sci.*, 11:2417–2426, 2002.

[92] L. M. C. Sagis, C. Veerman, and E. van der Linden. Mesoscopic properties of semiflexible amyloid fibrils. *Langmuir*, 20(3):924–927, 2004.

[93] D. Hamada, T. Tanaka, G. G. Tartaglia, A. Pawar, M. Vendruscolo, M. Kawamura, A. Tamura, N. Tanaka, and C. M. Dobson. Competition between folding, native-state dimerisation and amyloid aggregation in β-lactoglobulin. *J. Mol. Biol.*, 386(3):878–890, 2009.

[94] Z. Liu, Z. Li, H. Zhou, G. Wei, Y. Song, and L. Wang. Immobilization and condensation of DNA with 3-aminopropyltriethoxysilane studied by atomic force microscopy. *J. Microsc.*, 218(3):233–239, 2005.

[95] Robert J. Schalkoff. *Digital image processing and computer vision*, page 179. John Wiley & Sons, Inc. New York, NY, USA, 1989.

[96] S. Kullback and R. A. Leibler. On information and sufficiency. *ANMS*, 22:79, 1951.

[97] C. Lee, A. Nayak, A. Sethuraman, G. Belfort, and G. J. McRae. A three-stage kinetic model of amyloid fibrillation. *Biophys. J.*, 92:3448–3458, 2007.

[98] Terrell L. Hill. *Linear aggregation theory in cell biology*, page 93. Springer-Verlag, New York, 1987.

[99] T. Scheibel, J. Bloom, and S. L. Lindquist. The elongation of yeast prion fibers involves separable steps of association and conversion. *Proc. Natl. Acad. Sci. U. S. A.*, 101:2287–2292, 2003.

[100] D. W. Colby, Q. Zhang, S. Wang, D. Groth, G. Legname, D. Riesner, and S. B. Prusiner. Prion detection by an amyloid seeding assay. *Proc. Natl. Acad. Sci. U S A.*, 104(52):20914–20919, 2007.

[101] I. V. Baskakov and O. V. Bocharova. In vitro conversion of mammalian prion protein into amyloid fibrils displays unusual features. *Biochemistry*, 44(7):2339–2348, 2005.

Chapter 3

Characterization of α-Synuclein Amyloid Fibrils by Single-molecule Fluorescence Microscopy

3.1 Introduction

Amyloid formation involves sequential aggregates of different sizes and structural states, which require multiple biophysical techniques for characterization.[1] The use of several complementary techniques in β-lactoglobulin A (β-LGA) amyloid aggregation study has been discussed in Chapter 2. During ensemble measurements, averaged signals are monitored, which limit their application in heterogeneous systems. Take the size determination with dynamic light scattering (DLS) in β-LGA amyloid aggregation study as an example, an averaged hydrodynamic radius, R_{H}, was monitored at each stage of aggregation and was used as an indicator for aggregation progression. But when the heterogeneity of the system increased with time, the resolution of different species from the average decay curve became problematic. This was overcame by engagement of atomic force microscopy (AFM) as a single-molecule technique, which differentiated individual intermediates by size and morphology. All single-molecule level experiments are beneficial for highly heterogeneous systems by the same logic.

The clarification of aggregation mechanism relies on the characterization of both aggregation and structural states of the species involved. Time-resolved fluorescence technique has been widely used to monitor protein conformational changes. Fluorescent lifetime is the average time that a fluorophore spends in the excited state and can be measured with time-correlated single photon counting (TCSPC) technique.[2] It is sensitive to the microenvironment regulated by protein structure, and thus can be used to report the protein structure change. However, the interpretation of ensemble

lifetime data is not trivial for systems with high heterogeneity, such as amyloid aggregation. While the resolution of multiple components from a single recorded decay curve suffers from increasing heterogeneity of the system, a single-molecule level structure determination with lifetime imaging is quite straightforward, by the same logic as in single-molecule size measurement. A single-molecule lifetime measurement can not only distinguish the structural states from species to species, but also structural heterogeneity inside the species. Besides mechanism studies, structural characterization is also the key to identify the origin of toxicity during amyloid aggregation. Many studies have suggested the toxicity of small intermediates during amyloid aggregation.[3,4,5,6,7,8,9,10] Characterization of the toxic, abnormal structural states in these intermediates is the key to understanding the amyloidogenesis pathology and developing the treatments.

Messina et al. demonstrated a type of single-molecule fluorescence microscopy measurement for determination of aggregation states, utilizing the generally undesirable photobleaching property of the fluorophore. The aggregation number of multi-labeled dextran polymers were determined by counting the discrete dropping steps in fluorescence intensity trajectory, during controlled photobleaching.[11] This method has resolving power from one to up to 30 fluorophores, which covers the aggregation number of amyloid aggregation intermediates. With an proper fluorophore and controlled number of dye per monomer, this method can be utilized to determine the oligomeric number of aggregates during amyloid formation on a single-molecule basis. On the other hand, without defined ratio between fluorophore and protein, this method can be used to determine the binding efficiency of the fluorophore. Combining this photobleaching method with the single-molecule lifetime measurement, the fluorophore can be used as a reporter for aggregation and structural state at the same time. Synchronous determination of aggregation and structural state can be achieved.

Most amyloid aggregation mechanism studies are based on kinetics, and rely on the characterization of intermediates population evolution. Another approach towards aggregation mechanism is to probe the structural heterogeneity inside the aggregates. Unlike kinetic studies, this approach does not require the detection and characterization of a big number of species to establish the population. Several simple scenarios are

discussed below to show how this approach can lead to clarification of aggregation mechanism. If the aggregation can be described with a non-template polymerization model, which states that monomers convert to amyloidogenic conformation before aggregation, then only the amyloidogenic lifetime should be observed in all intermediates and fibrils. If the aggregation can be described with a templated polymerization model, which states that the conversion to amyloidogenic conformation happens after the monomer addition, then unstructured lifetime signals should be detected at the fibril ends. Amyloidogenic lifetime and unstructured lifetime could also be detected coexisting in some oligomers. For the aggregate folding model, amyloidogenic lifetime and unstructured lifetime should coexist in some species. But different with the templated polymerization model, no unstructured lifetime should be detected at the fibril ends. This type of information is not available in ensemble measurements and only single-molecule lifetime measurement has the capability to resolve multiple structural states inside one species.

Characteristic Thioflavin T (ThT) fluorescence is the most popular technique used to study amyloid aggregation kinetics. ThT experiences dramatic quantum yield enhancement upon binding to amyloid fibrils, with excitation around 445 nm and emission around 480 nm. It has the advantage of not interfering with the amyloid aggregation process in *in situ* experiments.[12,13,14] In most cases, characteristic ThT fluorescence intensity is used to detect presence of amyloid. A former study in the group used ensemble time-resolved ThT fluorescence to study sequential aggregation of β-LGA.[1] More than 10 lifetime components showed up during the incubation, ranging from 11 ps to 2.6 ns. Distinctive lifetime patterns were observed at different stages, indicating the interaction of ThT with different species during the incubation. A series of lifetime showed up before fibril formation, suggesting the ability of ThT to distinguish different structural states besides amyloid. However, no assignment could be made for most of the lifetime features. The 2.6 ns lifetime component predominated the signal at very late stage of the incubation, and was suggested to arise from ThT bound to mature amyloid fibrils. Another component of 500 ps was suggested to come from ThT bound to protofibrils. These results inspired the use of ThT as a structural reporter at single-molecule level in this chapter. Instead of using β-LGA, the Parkinson's disease-associated α-Synuclein

(αSyn) amyloid fibrils were used.

3.2 Materials and Methods

Materials

Water was purified by a Millipore Synergy 185 ultrapure online filter. 10 mM phosphate buffer (pH 7.55) was made from monobasic and dibasic sodium phosphate (Sigma-Aldrich, $\geqslant$ 99%), which was filtered through a 0.22 μm Stericup filter (Millipore). Stock ThT solution ($\sim$2 mM) was prepared by dissolving ultrapure grade ThT (AnaSpec, Cat No. 88306, $>$ 98% by HPLC, $>$ 95% by TLC) in phosphate buffer. This stock solution was then purified by hexane extraction (1:4 v/v, 10 times). Purified ThT stock solution was stored at 0 °C.

Expression of α-Synuclein

Escherichia coli BL21 DE3 strain (Invitrogen) were transfected by plasmids (pT7-7) encoding human wild-type αSyn and were gifts from Professor Jean Baum (Rutgers University, Piscataway, NJ). Expression and purification of αSyn followed published protocols with following modification.[15] After heating the solution at 10 °C for 20 minutes to remove background protein, supernatant containing αSyn was loaded onto 5 mL HiTrap Q column (GE Healthcare) and elute with NaCl (0-1 M gradient). Purified αSyn was dialyzed against NH_4HCO_3 (v/v 1:20) for at least 4 times at 4 °C. Purity of obtained αSyn was checked with SDS-PAGE (NuPAGE Bis-Tris 4-12%, Invitrogen) with a single band at around $\sim$14.5 kDa. Protein was lyophilized and stored at 4 °C.

Incubation of α-Synuclein

αSyn was first dissolved in 10 mM phosphate buffer (pH 7.55), and filtered through a 100 kDa centrifugal filter (Amicon Ultra, Millipore) to remove any pre-existing aggregates. The final incubation concentration for αSyn was 1 mg/mL, as verified by UV absorbance with extinction coefficient of 5800 $M^{-1}cm^{-1}$ at 276 nm. Sodium azide with a final concentration of 0.02 % (v/v) was added to prevent bacteria growth during

the incubation. Purified ThT stock solution was added to make a final concentration of 5 μM. The concentration was verified by absorbance measurements with extinction coefficient of 36,000 $M^{-1}cm^{-1}$ at 412 nm. Grade 1 polytetrafluoroethylene (PTFE) (1/16") balls (Engineering Laboratories) were cleaned by shaking in several changes of ethanol, followed by shaking in several changes of buffer. 35 PTFE balls were put into each 2 mL polypropylene microcentrifuge tube (Fishier Scientific). The tube was overfilled with incubation solution, capped and sealed with hot glue. Samples were checked to make sure that there was no air in the tubes before starting the incubation. Incubation was performed in a 37 °C oven and vertically rotated at 76 rpm on a Roto-Torque heavy duty rotator in dark for 6 days. After 6 days, samples were left quiescent at room temperature in dark for at least a week before single-molecule measurement. Samples prepared in this way were found to have a majority of aggregates as mature amyloid fibrils.[16]

Single-molecule Fluorescence Microscopy

0.17 mm thick coverslips (Fisher Scientific) were used as substrates for single-molecule fluorescence imaging. Coverslips were soaked in 90 °C piranha solution (1:7 v/v H_2SO_4: H_2O_2) for an hour, rinsed with plenty of Millipore water and blown dry with HPLC grade compressed nitrogen gas. 0.1 % (v/v) aminopropyltetratheoxysilane (APTES) (Acros cat. num.: 151081000) was applied evenly on freshly cleaned coverslips and allowed to react for 10 minutes. Unreacted APTES was rinsed away with Millipore water and the surface was blown dry with HPLC grade compressed nitrogen gas. For single-molecule fluorescence measurements, the incubated sample was diluted 10,000 times with 10 mM phosphate buffer (pH 7.55), containing 5 μM ThT. A homemade chamber was built on the modified coverslip and overfilled with sample solution, and sealed. Thus single-molecule images were taken on the surface immersed under solution. Fibrils were observed attaching to the coverslip in minutes, and their population increased with experimental time. The dilution assured a low fibril density on the coverslip so that individual fibrils could be imaged.

A mode-locked Ti:Sapphire laser (Spectra-Physics) was operated at 915.8 nm, with

pulse frequency at 80.00000 MHz and pulse width of 12 ps FWHM. The frequency was doubled by a type I secondary harmonic generating β-barium borate crystal (United Crystals) to provide excitation wavelength of 457.9 nm. The microscope was set up in an inverted epi-fluorescence configuration with a 60X, NA 1.4, oil-immersion objective (Olympus). After being expanded and collimated, the laser beam was reflected by a dichroic mirror (Omega Optical, model: 475DRLP) to fill the objective back aperture. A quarter-wave plate was used (CVI Laser, model: QWPM-515-05040R10) before the dichroic mirror to achieve circular polarization. The objective focused the excitation light into a diffraction-limited spot and collected fluorescence emission in the same focal volume. The collected fluorescence was separated from the excitation light by the same dichroic mirror and directed to the detection channel. A 457.9 nm holographic notch filter (Kaiser Optical Systems, Part Num. HNPF-457.9-1.0) and a 475 nm long wave pass filter (Andover Corporation, Cat. Num. 475FG03-50S) were used to further attenuate excitation light and collect characteristic emission of amyloid-bound ThT $>$ 475 nm. Image scanning was enabled by a closed-loop nanopositioning stage with 0.4 nm resolution (Mad City Labs, Nano-LP200, Nano-Drive controller). During the measurements, the position of the focal volume created by the objective was fixed, while the sample was moved by the stage. Data collection was controlled with a Becker-Hickl SPC-830 time-correlated single photon counting (TCSPC) board and a Pentium 4 computer with custom-made LabVIEW virtual instruments. Instead of taking a high resolution lifetime image over the whole scan area, a fast, low resolution scan was performed first to locate the particles in the scan area. Photons were then collected from the picked locations on fibrils and background. The stage moved the sample to one spot at a time and photons were collected from that spot until no further photobleaching was observed. This greatly reduced the measurement time required in high-resolution fluorescence lifetime imaging.

During this type of measurement, instead of producing the decay time histogram, TCSPC board (SPC-830) was set to first-in-first-out (FIFO) mode, in which photons were recorded in a time-tagging way one by one. Generally, FIFO mode acquisition avoids the overflow of count in the decay time channels, and enables collection of big

amount of photons. Two important pieces of information are stored for each photon in this mode: macro time, micro time. Macro time is the time between the start of the experiment and the detection of the tagged photon. Micro time is the time between the detection of the tagged photon and the synchronized pulse. Intensity trajectory and decay time histogram were constructed in IgorPro (Wavematrics) based on macro time and micro time of photons collected at each location.

It is worth noticing that this setup had a detection volume of ∼300 nm diameter on the coverslip surface, and photons were collected from all the fluorophores in the detection volume. In the case of amyloid fibrils, fluorescence from multiple ThT molecules was collected at each location because of high fluorophore density on the fibril. The fluorescence lifetime decay curve is a convolution of multi-exponential decays with the instrument response function. The multi-exponential function used for data fitting is shown in Eqn. 3.1

$$f(\tau, t) = S + \sum_{j} A_{\mathrm{j}} e^{-\frac{t}{\tau_j}} \tag{3.1}$$

where S is the scattering term, A_{j} is the amplitude of each decay and τ_{j} is the lifetime. The goodness of the fit can be evaluated with the reduced Chi-square test. Measurement of instrument response function in single-molecule experiment is not as straightforward as ensemble fluorescence measurement. The instrument response was measured by replacing the sample with a thoroughly cleaned coverslip.

3.3 Results and Discussion

3.3.1 Single-molecule Fluorescence Intensity Images of α-Synuclein Fibrils

After 6 days of incubation, the sample was left quiescent at room temperature for another week. The incubated sample was diluted 10,000 times with 5 μM ThT in 10 mM phosphate buffer (pH 7.55) before injection into the sample chamber. A typical fluorescence intensity image was shown in Fig. 3.1a, where αSyn fibrils were observed with enhanced ThT fluorescence. In the image, fibrils showed up with different lengths

up to several micrometer. The lateral dimension was a result of convolution between the fibril dimension with the microscope focal volume. While amyloid fibrils generally have a diameter smaller than 10 nm, typical microscope focal volume has a much larger diameter of ∼300 nm near the coverslip surface. The convolution resulted in imaged fibrils of several hundred nanometers wide, and determined the spatial resolution of the single-molecule measurement. As for the morphology, fibrils in fluorescence intensity images were straight and unbranched. Variation in fluorescence intensity was observed along the fibrils, without defined pattern.

3.3.2 Single-molecule Photobleaching Measurement

After locating fibrils in the intensity image, FIFO measurements were taken at picked positions as indicated by the cursors in Fig. 3.1a. Cursors were placed to investigate ThT bound to fibrils (cursor 2, 3 and 7), at the end of fibrils (cursor 1, 4 and 8) and away from fibrils on the coverslip (cursor 5 and 6). Photons were collected at each cursor until the fluorescence intensity leveled off. The intensity trajectories are shown in Fig. 3.1c. The intensity of cursors on the fibrils were of 2.5∼4 times of the background. The background measured here had higher intensity compared with the control experiment, in which the chamber was filled with buffer only. This suggested that ThT molecules bound to the coverslip and contributed to the background signal.

Photobleaching took place for ThT bound to fibrils, as indicated by the fast drop at the beginning of the trajectories in Fig. 3.1c. Rescan of the same area after ∼20 minutes confirmed the occurrence of photobleaching and showed no recovery of the fluorescence intensity. During the measurements, the sample chamber was filled with 5 μM ThT solution, which provided a pool of fresh ThT around the fibrils. According to LeVine and coworkers, ThT bound to fibrils within seconds.[17] With fresh ThT around, the unrecoverable photobleaching of ThT bound to fibrils suggested that there was no exchange between the fibril-bound ThT and the free ThT around. This could happen if the attachment of fibrils on the coverslip shielded the binding sites away from ThT in the solution. However, considering the way of fibrils lying on the surface, this would require all the binding sites to be aligned along a narrow line on the fibrils

in contact with the surface, which was very unlikely.[18] Another possibility was that photobleaching somehow "froze" the destructed ThT onto the fibril and interrupted the interchange. As for cursors on the coverslip, fluorescence intensity remained the same as shown by trajectories in Fig. 3.1c. The absence of photobleaching could be explained by the replenishment of ThT on the surface through fast exchange with ThT in the solution. In another control experiment, ThT was deposited onto coverslip in air by spin coating. Without the fresh ThT reservoir, photobleaching happened and no recovery of the intensity was observed.

ThT was not covalently attached to the protein and the ratio between the two was unknown. As a result, no connection could be made between the number of photobleaching steps and the aggregation number. However, in the case of fibrils, the absolute aggregation number is not as important as in small oligomers. Instead, the number of photobleaching steps could be used to determined the ThT density on amyloid fibrils. Unfortunately, examination of the intensity trajectories in Fig. 3.1c showed no distinctive photobleaching steps. Attempts was made to resolve the steps by lowering the excitation intensity to reduce the photobleaching rate, but without success. The counting ability of photobleaching measurement depends on the number of photons the fluorophore emits before the photobleaching happens. In other words, enough photons need to be collected for each intensity level in the trajectory. The selection of fluorophore is thus very critical in this type of measurement.[11] The observed behavior of ThT in this chapter suggested that it was not a suitable probe for photobleaching measurement.

3.3.3 Lifetime of Fibril-bound Thioflavin T

For each FIFO cursor, fluorescence lifetime decay curve was constructed, using micro time of the collected photons. With a focal volume of ∼300 nm diameter, even though the cursors were placed on the fibrils, a big area of the background was included in the measurement. For cursors on fibrils, only photons collected before the plateau were considered.

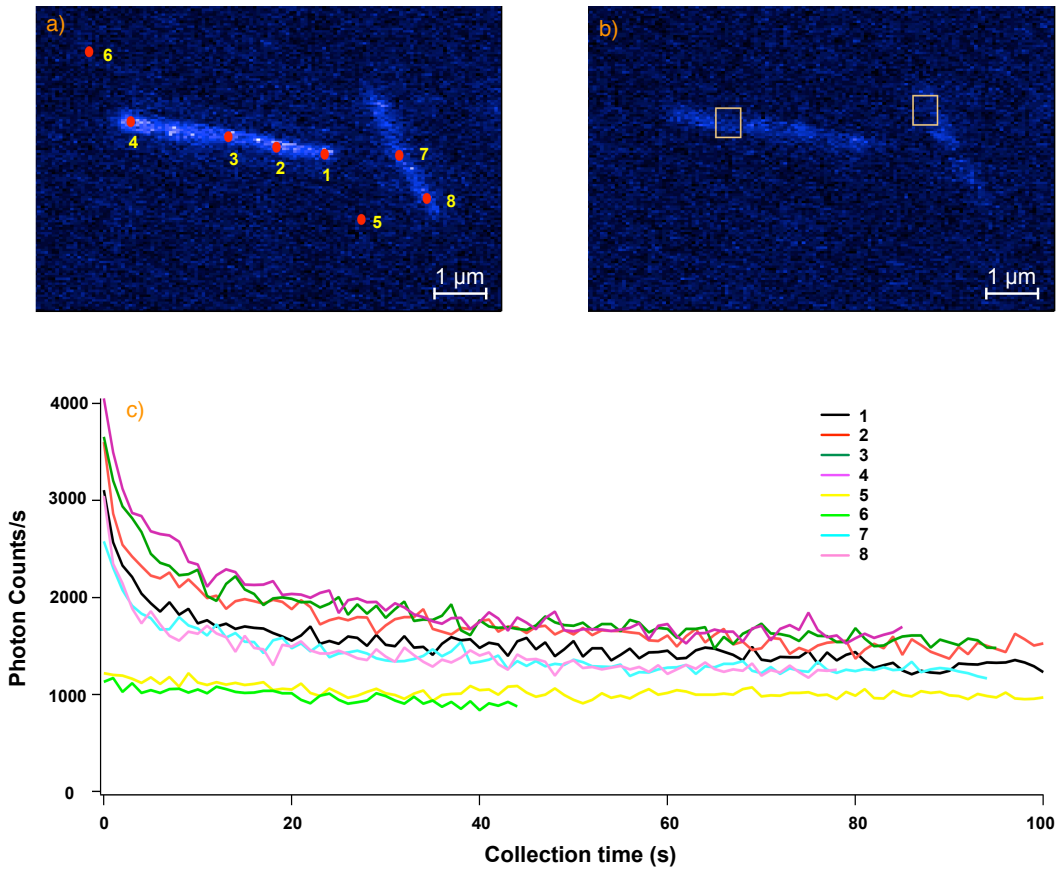

Figure 3.1: Single-molecule fluorescence photobleaching measurements on αSyn fibrils stained with ThT. a) Fluorescence intensity image of αSyn fibrils with excitation power of $\sim$10 μW. Image resolution is 128$\times$128 pixel, with 5 μs collection time for each pixel. ThT-stained fibrils were illuminated. Fibrils were of several micrometer long. The convolution between fibril width with the objective focal volume resulted in broadened fibril width of $\sim$300 nm. After a quick scan to obtain this intensity image, 8 positions were picked for FIFO collection. Cursor 2, 3, and 7 were positioned on the fibrils. Cursor 1, 4, 8 were placed at the fibril ends. Cursor 5 and 6 were placed on the background, away from any fibril. b) Intensity image collected for the same area $\sim$20 minutes later, following the FIFO measurements. Compared with a), fluorescence intensity dropped at the cursor positions. FIFO data were also taken for positions indicated by the two squares but these data were discarded because of fluctuation in the excitation intensity during collection. c) From the macro time of photons collected at each cursor, the fluorescence intensity trajectories were constructed. For all the cursors on the fibrils, there was an intensity drop at the beginning, indicating the occurrence of photobleaching of fibril-bound ThT. For the two cursors placed on the background, cursor 5 and 6, the intensity was relatively low and remained unchanged.

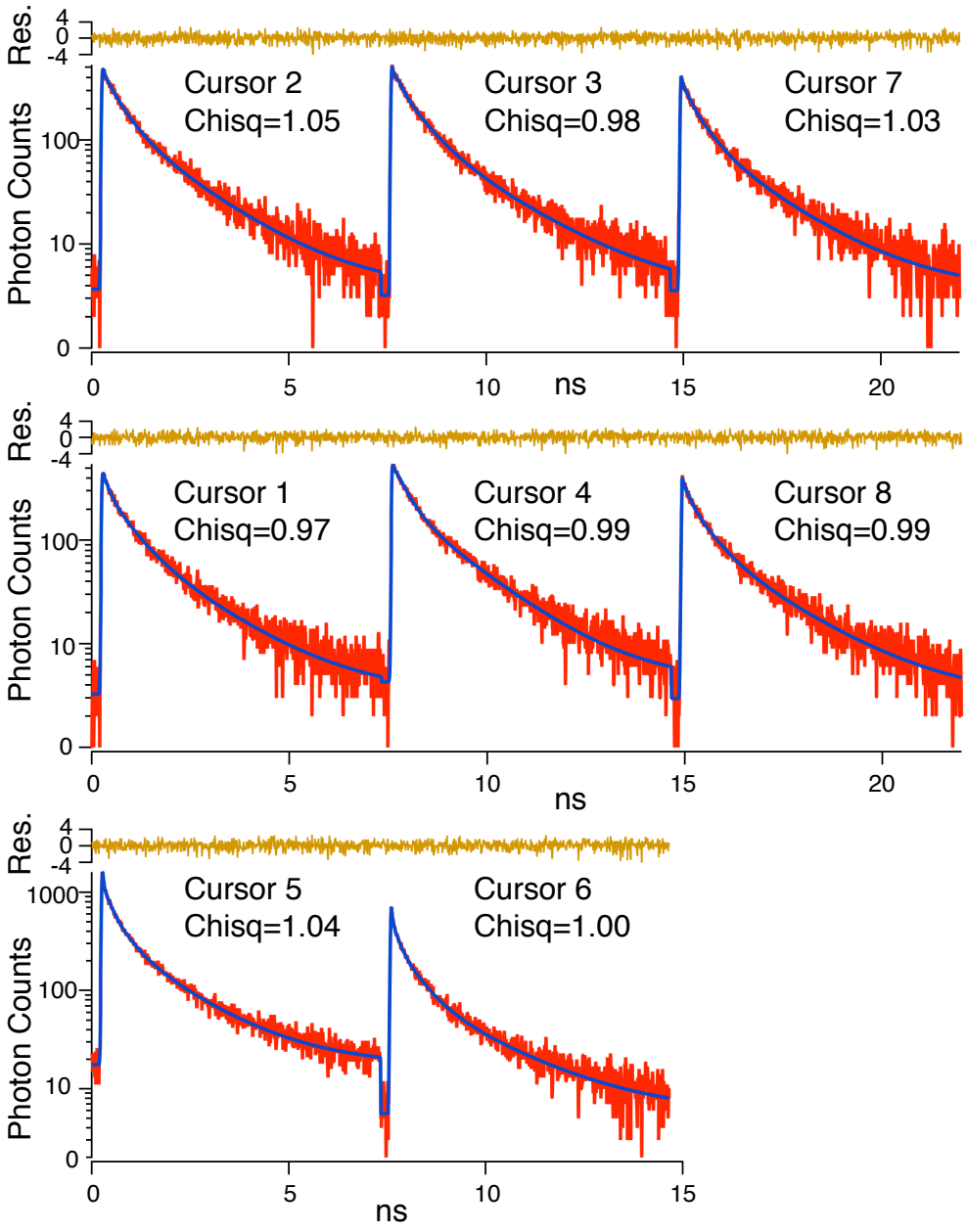

Figure 3.2: Fluorescence lifetime analysis for FIFO cursors. Lifetime decay curves were constructed from photon micro time, as shown in red. For cursor 1, 2, 3, 4, 7, 8, only photons collected during the intensity drop were considered. All the curves were fit with three exponential contributions. The fits and weighted residuals are shown in blue and brown, respectively. No difference in lifetime was observed for fibril-bound and coverslip-bound ThT.

All the decays could be fit with three exponential contributions: a very short lifetime component of ∼26 ps to ∼73 ps, an intermediate component of ∼340 ps to ∼570 ps and a long lifetime component of ∼1.4 ns to ∼1.8 ns. Fits are shown with the calculated reduced chi-square in Fig. 3.2. Surprisingly, no difference was observed for the lifetime of ThT bound to fibrils, at the fibril ends, and on the coverslip. This suggested that ThT molecules were held rigidly upon binding to amyloid fibrils as they bound to the APTES modified coverslip. This also suggested that local environment had little influence on the ThT lifetime. Similar lifetime implied similar quantum yield for fibril-bound and coverslip-bound ThT. Thus the observation of enhanced intensity for fibril-bound ThT compared with coverslip-bound ThT could not be explained by difference in quantum yield. The origin of this intensity difference was clarified in Chapter 4, through studies on the ThT fluorescence mechanism. The observation of fibrils with higher intensity than background was a result of the spectral shift. As shown later in Chapter 4, ThT was observed to bind to cuvette surface with fluorescence excitation at ∼420 nm and emission at ∼480 nm. Similar spectral property was expected for ThT on the coverslip surface. The fibril-bound ThT had excitation at ∼445 nm and emission at ∼476 nm. 457.9 nm excitation was chosen to excite fibril-bound ThT, which was away from the excitation maximum of surface-bound ThT. With smaller absorption cross-section, surface-bound ThT was illuminated with much lower efficiency and appeared as background in the single-molecule fluorescence intensity images.

3.4 Future Work

Nile red (NR), 9-diethylamino-5H-benzo[α]phenoxazine-5-one, is a solvatochromic fluorophore widely used for intracellular lipid droplets detection.[19] The emission of NR experiences red-shift in polar environment. In an earlier study, NR was covalently attached to cysteine mutant of human αSyn (A19C) to monitor the conformational change by time-resolved fluorescence measurement.[20] A preliminary single-molecule fluorescence lifetime imaging study has also been carried out to show the potential use of NR as a structural reporter for αSyn. Since NR is much brighter than ThT, single dye resolution is possible, which does not appear to be the case with ThT. Future work

includes evaluation of how the extrinsic label of NR affects the aggregation process. This can be done by comparing αSyn amyloid incubation with and without NR with AFM measurement. Then the single-molecule fluorescence lifetime imaging and photobleaching experiments described in this chapter can be performed, using NR instead of ThT.

Bibliography

[1] J. T. Giurleo, X. He, and D. S. Talaga. β-lactoglobulin assembles into amyloid through sequential aggregated intermediates. *J. Mol. Biol.*, 381(5):1332–1348, 2008.

[2] J. R. Lakowicz. *Principles of Fluorescence Spectroscopy.* Springer, third edition, 2006.

[3] L. Lue, Y. Kuo, A. E. Roher, L. Brachova, Y. Shen, L. Sue, T. Beach, J. H. Kurth, R. E. Rydel, and J. Rogers. Soluble amyloid-β peptide concentration as a predictor of synaptic change in Alzheimer's disease. *Am. J. Pathol.*, 155:853–862, 1999.

[4] C. A. McLean, R. A. Cherny, F. W. Fraser, S. J. Fuller, M. J. Smith, K. Beyreuther, A. I. Bush, and C. L. Masters. Soluble pool of Aβ amyloid as a determinant of severity of neurodegeneration in Alzheimer's disease. *Ann. Neurol.*, 46:860–866, 1999.

[5] W. L. Klein, G. A. Krafft, and C. E. Finch. Targeting small Aβ oligomers: the solution to an Alzheimer's disease conundrum? *Trends Neurosci.*, 24:219–224, 2001.

[6] W. L. Klein, W. B. Stine, and D. B. Teplow. Small assemblies of unmodified amyloid-β protein are the proximate neurotoxin in Alzheimer's disease. *Neurobiol. Aging*, 25:569–580, 2004.

[7] B. Caughey and P. T. Lansbury. Protofibrils, pores, fibrils, and neurodegeneration: separating the responsible protein aggregates from the innocent bystanders. *Annu. Rev. Neurosci.*, 26:267–298, 2003.

[8] D. C. Crowther, K. J. Kinghorn, E. Miranda, R. Page, J. A. Curry, F. A I Duthie,

D. C. Gubb, and D. A. Lomas. Intraneuronal Aβ, non-amyloid aggregates and neurodegeneration in a Drosophila model of Alzheimer's disease. *Neuroscience*, 132(1):123–135, 2005.

[9] J. P. Cleary, D. M. Walsh, J. J. Hofmeister, G. M. Shankar, M. A. Kuskowski, D. J. Selkoe, and K. H. Ashe. Natural oligomers of the amyloid-β protein specifically disrupt cognitive function. *Nat. Neurosci.*, 8(1):79–84, 2005.

[10] J. Laurn, D. A. Gimbel, H. B. Nygaard, J. W. Gilbert, and S. M. Strittmatter. Cellular prion protein mediates impairment of synaptic plasticity by amyloid-β oligomers. *Nature*, 457(7233):1128–1132, 2009.

[11] T. C. Messina, H. Kim, J. T. Giurleo, and D. S. Talaga. Hidden Markov model analysis of multichromophore photobleaching. *J. Phys. Chem. B*, 110(33):16366–16376, 2006.

[12] L. Nielsen, R. Khurana, A. Coats, S. Frokjaer, J. Brange, S. Vyas, V. N. Uversky, and A. L. Fink. Effect of environmental factors on the kinetics of insulin fibril formation: elucidation of the molecular mechanism. *Biochemistry*, 40(20):6036–6046, 2001.

[13] M. Manno, M. Mauro, E. F. Craparo, A. Podest, D. Bulone, R. Carrotta, V. Martorana, G. Tiana, and P. L. San Biagio. Kinetics of different processes in human insulin amyloid formation. *J. Mol. Biol.*, 366(1):258–274, 2007.

[14] M. Groenning, M. Norrman, J. M. Flink, M. van de Weert, J. T. Bukrinsky, G. Schluckebier, and S. Frokjaer. Binding mode of thioflavin T in insulin amyloid fibrils. *J. Struct. Biol.*, 159(3):483–497, 2007.

[15] H. Yagi, E. Kusaka, K. Hongo, T. Mizobata, and Y. Kawata. Amyloid fibril formation of α-synuclein is accelerated by preformed amyloid seeds of other proteins: implications for the mechanism of transmissible conformational diseases. *J. Biol. Chem.*, 280(46):38609–38616, 2005.

[16] J. Pronchik, X. He, J. T. Giurleo, and D. S. Talaga. In vitro formation of amyloid from α-synuclein is dominated by reactions at hydrophobic interfaces. *J. Am. Chem. Soc.*, 132(28):9797–9803, 2010.

[17] H. LeVine. Thioflavine T interaction with synthetic Alzheimer's disease β-amyloid peptides: detection of amyloid aggregation in solution. *Protein Sci.*, 2(3):404–410, 1993.

[18] X. He, J. T. Giurleo, and D. S. Talaga. Role of small oligomers on the amyloidogenic aggregation free-energy landscape. *J. Mol. Biol.*, 395:134–154, 2010.

[19] P. Greenspan, E. P. Mayer, and S. D. Fowler. Nile red: a selective fluorescent stain for intracellular lipid droplets. *J. Cell Biol.*, 100(3):965–973, 1985.

[20] J. Giurleo. *Time-resolved fluorescence studies of protein aggregation leading to amyloid formation.* PhD thesis, Rutgers University, 2008.

Chapter 4

Mechanism of Characteristic Thioflavin T Fluorescence Upon Binding to Amyloid Fibrils

4.1 Introduction

4.1.1 Use of Thioflavin T as an Amyloid Probe

Thioflavin T (ThT) is a standard fluorescence molecular probe for amyloid fibrils, and has been widely used for detection of amyloid both *in vivo* and *in vitro*.[1] Upon binding to amyloid fibrils, ThT experiences a dramatic increase in quantum yield with excitation and emission maximum around 445 nm and 480 nm, respectively.[2,3] ThT was first used in 1959 as a histological stain to show amyloid deposits in tissue sections.[4] Later, ThT fluorescence intensity was shown to be proportional to the amyloid fibril load *in vitro* and thus could be used to monitor the progression of amyloid formation.[2,5]

ThT does not interfere with amyloid fibrillization kinetics in most cases. This makes ThT especially useful in *in situ* kinetic studies to evaluate environmental effects on fibrillization kinetics.[6,7,8] Besides steady-state fluorescence measurement, ThT characteristic fluorescence has also been successfully used in fluorescence microscopy to image amyloid fibrils. Kitts et al. successfully imaged individual insulin fibrils with near-field scanning fluorescent microscopy.[9] Andersen et al. monitored the *in situ* growth of glucagon and amyloid β-peptide fibril on coverslip with total internal reflection fluorescence microscopy.[10] In Chapter 3, ThT was used in single-molecule fluorescence imaging of α-Synuclein (αSyn) amyloid fibrils. Besides intensity, Sabate et al. used ThT anisotropy at $\sim$480 nm to monitor fibrillization of HET-s fungal prion protein, and generated a sigmoidal kinetic profile.[11]

ThT fluorescence has also been observed in absence of amyloid fibrils in some cases,

which brings its specificity into question. For example, Harel et al. showed that ThT could be used to monitor conformational change in Torpedo Californica Acetylcholinesterase (TcAChE). ThT was observed to bind to the peripheral site of TcAChE monomer and showed ∼1000 fold enhancement of fluorescence intensity, with excitation maximum at 448 nm and emission maximum at 488 nm.[12] Wolfe et al. also showed that ThT bound to a non-fibrillar hexameric species during amyloidogenic aggregation of β-microglobulin, with comparable magnitude of fluorescence enhancement as binding to fibrils.[13] Interaction of ThT with monomer, small oligomers formed earlier in the β-lactoglobulin A (β-LGA) amyloid aggregation was also observed. With small quantum yield, these events were usually overlooked in fluorescence intensity measurements but were resolved in time-resolved fluorescence studies. Specific ThT lifetime patterns were observed at different stages before the mature fibril formation.[14] In another case, ThT failed to report the formation of ΔE22-Aβ_{1-39} fibrils, while they were unmistakably detected with typical amyloid appearance in electron microscope (EM) and cross-β X-ray diffraction pattern.[15]

As an empirical method, ThT fluorescence for amyloid fibril detection is convenient but not perfect. Elucidation of the ThT characteristic fluorescence mechanism is the basis for effective diagnosis of amyloidosis, data interpretation in experiments, and rational design of more efficient amyloid probes.[1,16] The interaction of ThT with amyloid fibrils and the mechanism of characteristic fluorescence is thus under intensive study. No molecular model has been determined for ThT bound to amyloid fibrils. Amyloid fibrils have the well-known structure feature of continuous β-sheet running parallel to the fibril long axis, but there is no structural detail for fibrils at molecular level.[17] ThT fluorescence relies on structural specificity. In Chapter 3, it was showed that ThT was held rigid upon binding to amyloid fibrils. Not only should ThT recognize certain structure features on amyloid fibrils for rigid binding, but its photophysical properties should also be regulated by these features.

4.1.2 Properties of Thioflavin T

ThT, 3, 6-dimethyl-2-(4-dimethylaminophenyl)-benzothiazolium cation has one positive charge localized on nitrogen of the benzothiazole ring. The structure can be divided into two relatively rigid fragments: the benzothiazole ring and the dimethylaminobenzene as shown in Fig. 4.1. The rings can rotate freely around the shared C-C bond. This motion can be characterized with the dihedral angle φ between the two fragments.[18,19] In the two crystal structures of ThT determined by Rodriguez-Rodriguez et al., two ThT cations stacked with a head to tail disposition, with the charges on the opposite sides.[20] The stacking interaction resulted in increased planarity of ThT molecules in both crystals, with a dihedral angle < 25 °. ThT is 15 Å long and 6 Å short, with a thickness of 4.3 Å assuming a planar conformation. Krebs et al. showed that ThT excitation dipole lied parallel to its structural long axis, through fluorescent polarization measurement on the aligned ThT in polyvinyl alcohol/ThT films.[21]

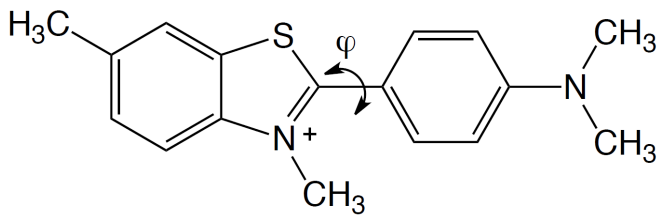

Figure 4.1: Chemical structure of thioflavin T

4.1.3 Photophysical Properties of Thioflavin T

Aqueous ThT solution has an absorption maximum at ∼412 nm, with an extinction coefficient of 36,000 $M^{-1}cm^{-1}$.[3,22] The absorption maximum red-shifts in solvents with decreasing orientational polarizability. Among the solvents studied, water has the largest orientational polarizability, and shortest absorption at 412 nm, compared to 430 nm in dichlormethane.[3,23] Upon interaction with amyloid fibrils, ThT absorption maximum shifts from ∼412 nm to ∼450 nm.[18,24]

The determination of ThT fluorescence spectra in solutions is somehow problematic. The fluorescence spectra of aqueous ThT solutions are overwhelmed by a fluorescence

feature with an excitation maximum around 340 nm and an emission maximum around 450 nm.[2,3,23,25] Besides this predominant short-wavelength peak, a low-intensity shoulder at ∼420 nm is also observed for ThT excitation spectra when emission is recorded at 480 nm. Many studies mistake the 340 nm excitation and 450 nm emission peaks as from ThT in solutions, which are actually produced by a fluorescent impurity.[13,26,25] With a very low concentration, the absorption of this impurity is low, and is completely disguised by the primary ThT absorption peak at 412 nm. On the other hand, with a large quantum yield, the strong fluorescence signal from this impurity overwhelms ThT fluorescence and results in false excitation maximum at 340 nm and emission at 450 nm. Removal of this fluorescent impurity by recrystallization reduced the intensity ratio of excitation peak and shoulder, I_{340}/I_{420}. While ThT is insoluble in hexane and cyclohexane, this impurity has an absorption maximum near 340 to 350 nm in both solvents.[3] The identity of this impurity has not been determined, and there is no effective way to separate this fluorescence impurity to a level low enough to remove their fluorescence signal in the spectra.[3] With acknowledgment of the impurity origin of the ∼340 nm peak, studies focus on low intensity feature with excitation at ∼420 nm and emission at ∼480 nm, which has been assigned to ThT in aqueous solution.[3] This assignment results in a discrepancy between the absorption maximum and the excitation maximum for aqueous ThT solution. The origin of this discrepancy has not been identified.

Photophysical properties of ThT in different solvents has been studied.[3,18,23,27] No simple dependence of either the emission maximum nor the quantum yield on the solvent dielectric properties was observed.[18,23] With a constant dielectric constant, Friedhoff et al. observed a linear relationship for ThT quantum yield and viscosity of a wide variety of solvents. This relationship was fit to a fluorescence molecular rotor model.[27] Studies also showed great enhancement of ThT quantum yield with increasing viscosity of glycerol-water mixtures, achieved by either increasing the glycerol content or decreasing the temperature.[19,28] In all glycerol-water mixtures studied, the emission maximum stayed around 490 nm.[19,28]

4.1.4 Proposed Mechanisms for Characteristic Thioflavin T Fluorescence

Different models have been proposed for ThT fluorescence mechanism. The micelle model states that the pre-existing micelle in ThT solution is the fluorescent species, instead of monomeric ThT. A break in the concentration dependence of conductivity was used as evidence for micelle formation in ThT aqueous solution. Khurana et al. showed that the conductivity of the ThT solution was independent of the ThT concentration and stayed around 0 μS/cm for concentrations < 4 μM. For concentrations > 4 μM, linear dependence was observed. A critical micelle concentration (CMC) of 4.0 $\pm$0.5 μM was thus determined.[29] The break in concentration dependence of conductivity curve is a standard method for the CMC determination of ionic surfactants. Before the CMC, the conductivity increases linearly with the concentration. After the CMC, the conductivity keeps increasing linearly with the concentration, but with a smaller rate. The formation of micelles results in decreased rate because micelles have lower mobility than surfactant monomers. The profile observed by Khurana et al. was quite different with the standard profile. Most likely, the observed change in conductivity around 4 μM for ThT reflected the instrumental limitation in their study. For solutions with concentration < 4 μM, the conductivity was too low to cause instrument response. For solutions with concentration > 4 μM, the conductivity increased with ThT concentration. In the same study, nanometer-sized globular particles were observed in atomic force microscopy (AFM) images by deposition of ThT solution on mica surface. Deposited in presence of amyloid fibrils, nanometer-sized globular particles were found attaching along the fibrils. These particles were claimed as ThT micelles. However, there was no evidence to support the existence of these particles in solution, not to mention the causative relationship between these particles and the observed fluorescence.

The exciton model suggests that two ThT molecules stay together to act as fluorescence exciton. Raj et al. observed fluorescence with excitation at $\sim$430 nm and emission at $\sim$484 nm in presence of γ-cyclodextrin (γ-CD), but not β-cyclodextrin (β-CD). It was suggested that γ-CD could accommodate two ThT molecules and promoted

exciton formation, while β-CD cavity was too small. Even though the proposed dimeric fluorescent species was called excimer in this study, it was actually exciton by definition. While excimers are formed by an excited molecule with a ground state molecule, excitons are formed by two ground state molecules before excitation. The formation of excitons inside γ-CD was proposed merely based on the cavity size difference of the two reagents and was not supported by any direct evidence. Close examination of the fluorescence data revealed fast binding of the fluorescence impurity to γ-CD, with excitation maximum of $\sim$330 nm and emission at $\sim$450 nm. Inclusion of this impurity into β-CD and γ-CD could happen before ThT binding and thus reduced the cavity size.[26,30] Ilanchelian et al. observed ThT fluorescence in the presence of DNA. The co-occurrence of fluorescence decrease at $\sim$450 nm and increase at $\sim$485 nm was interpreted as formation of exciton promoted by DNA.[25] However, this explanation ignored the fact that the 450 nm fluorescence was from the fluorescence impurity instead of ThT monomers.

ThT has also been suggested to work as a fluorescence molecular rotor. Upon excitation, the molecular rotor is excited to a local fluorescent excited state. Fast intramolecular rotation of the molecule occurs and the molecule readily relaxes to an equilibrium twisted intramolecular charge transfer (TICT) state. Relaxation from this TICT state to ground state is non-radiative. The quantum yield of the molecular rotor depends on the accessibility of the TICT state. The slower the intramolecular rotation, the larger the quantum yield, because more molecules relax from the local fluorescent state. When the intramolecular rotation is completely prohibited, all relaxation happens from the local fluorescent state and the quantum yield is maximized. ThT has a typical structure of molecular rotors. Molecular rotors generally have an electron donating and an electron accepting unit. These two units have relatively rigid conformation and are connected with a bond or an electron-rich unit, where the intramolecular rotation takes place.

With little change in spectral shape and peak position, ThT quantum yield increases with increasing viscosity of the solution. This is a typical observation for fluorescence

molecular rotors.[19,28] Through quantum chemistry calculation, Stsiapura et al. suggested that the intramolecular rotation of ThT could lead to the formation of TICT state. The dihedral angle φ was calculated to be 37° for ThT at ground state and 90° for excited state at equilibrium in gas phase. The calculation also showed increase of dipole moment from 7 D to 14 D, indicating the occurrence of intramolecular charge transfer accompanying the rotation.[19] With a small energy barrier for intramolecular rotation of ThT around the C-C bond between the benzothiazole ring and the dimethylaminobenzene, relaxation readily occurs from the local fluorescent excited state to the TICT state in solutions with low viscosity. With increased viscosity of the solutions, the rotation is slowed, which results in the increased quantum yield. Characteristic ThT fluorescence upon binding to amyloid fibrils has been suggested to act in the same way that the intramolecular rotation is hindered upon binding, and the TICT state becomes inaccessible.[18,19,31,32] The molecular rotor model can explain the quantum yield enhancement of ThT upon binding to fibrils, but not the spectral shifts experienced by ThT.

4.1.5 Interaction of Thioflavin T with Amyloid Fibrils

The insolubility of amyloid fibrils prevents the co-crystallization of ThT with fibrils, and no experimentally determined molecular model for ThT binding is available. Based on the confocal fluorescence microscopy pattern for ThT stained spherulites, Krebs et al. suggested that ThT bound to bovine insulin and β-LG fibrils with its structural long axis aligned parallel to the fibril axis.[21] Spherulites are super assembly of amyloid fibrils, in which fibrils orient radially around an irregular core. Krebs showed that because of the regular alignment of ThT along the fibril, only diametrically opposite parts in the direction of excitation polarisation of the spherulites were excited.[21] Using near field scanning polarized fluorescence microscopy, Kitts et al. showed that only insulin fibrils sitting in the direction of detection polarisation were observed, indicating the alignment of ThT along insulin fibrils.[9]

Various binding sites and amyloid fibril structural features have been suggested to be essential for ThT fluorescence. The cross-β-sheet structural hallmark of amyloid fibrils

exists at the level of protofilaments, which are the basic fibrillar amyloid unit and bundle together to form amyloid fibrils. As indicated by a universal intense 4.8 Å meridional reflection in the diffraction pattern for amyloid fibrils, the continuous cross-β-sheets run parallel to the fibril axis, with the strands perpendicular to the axis. However, β-sheet structure alone cannot induce the characteristic ThT fluorescence. No fluorescence was observed in β-sheet-rich protein precursors nor the β-sheet constructed by peptide self-assembly.[30,33] Biancalana et al. suggested that this difference might be resulted from a threshold of β-sheet length or flatness.[33]

Side chains in cross-β-sheet structure can form ladders running on fibril surface.[21,33] Krebs et al. suggested that ThT could bind in the grooves formed by these side chain ladders.[21] Instead of being flatly extended, β-sheets in amyloid fibrils are arranged in helix, with axis coincident to fibril axis.[17,34,35] With an average twisting angle of 15° for neighboring strands, 24 β-strands make up one helical turn.[17] Thus both the hydrogen bond and the side chain ladder orientations are different with those in extended β-sheet. The helix configuration of β-sheets creates a central hollow cavity in protofilaments, which provides another plausible binding site for ThT. For example, a 6 Å wide cavity was indicated for poly-L-glutamine, and 6.5 Å for Transthyretin (TTR) protofilaments. Water molecules or other small molecules was suggested to fill in this type of cavities.[17,35] Comparing the X-ray diffraction pattern of insulin fibril before and after ThT binding, Groenning et al. implied that ThT molecules probably bound in these cavities formed inside or by the protofilaments as well.[8]

The number of β-sheets in protofilaments differs from precursor to precursor.[17,34,35] For example, αSyn and poly-L-glutamine were detected with only one β-sheet in their protofilament, while four β-sheets were determined to stack together in each TTR protofilament.[36,35] Nelson et al. proposed a structure model at atomic level for cross-β-sheet spine, based on X-ray diffraction study of microcrystal formed by a seven-residue peptide segment from yeast protein Sup35. The structure unit was described as a steric zipper, in which the side chains arranged in register between a pair of β-sheets. A dry surface was formed by this steric zipper arrangement between the two β-sheets with a distance of $\sim$8.5 Å which could provide binding site for ThT.[37] It has also been

suggested that ThT can bind in between fibrillar substructures, such as protofilaments and protofibrils.[8,30] It is important to keep in mind that the observed binding mode of ThT is not necessarily the one that causes characteristic fluorescence. Multiple binding sites might exist on fibrils, but not all of them are related with the characteristic fluorescence.[8,38] Moreover, controversial observations have been made on whether the accessibility of ThT binding sites differs for ThT added before and after the amyloid incubation.[8,39]

4.1.6 Chiral Absorption of Thioflavin T Upon Binding to Fibrils

Positive, negative and zero cotton effect has been observed at ∼450 nm for ThT bound to bovine insulin fibrils incubated under different conditions. This was first used as evidence that ThT bound to fibrils with a twisted conformation.[24,40,41] Further study showed that the difference in the induced CD signal was likely to come from polymorphism of amyloid fibrils. AFM imaging showed that the induced CD signal only appeared with presence of superstructures, in which fibrils laterally aligned with one another.[41] The author proposed that the induced CD signal arose from ThT excitons, whose formation was promoted by the lateral alignment of fibrils. Negative cotton effect at ∼450 nm was also observed for ThT bound to HET-s amyloid fibrils.[38]

4.1.7 Crystal Structures of Thioflavin T Bound to Other Systems

Wolfe et al. observed enhanced fluorescence intensity in co-crystal of ThT with β-2 microglobulin (β2m) hexamer ($\beta 2m_{holo}$) with excitation maximum at ∼440 nm, and emission at ∼492 nm.[13] In this co-crystal, ThT molecule was determined to be intercalated at the intersheet interfaces formed by two β-sheets, orthogonal aligned to the β-strand. Moreover, the interaction was stabilized by stacking interaction of ThT with the aromatic side chains. The benzothiazole ring was fixed in a well-defined binding pocket, while the dimethylaminobenzene could rotate between φ value of 57° and 102°. Biancalana et al. designed peptide self-assembly mimic (PSAM) scaffolds to mimic amyloid fibril structural features, with only one layer of β-sheet. The originally designed PSAM, which was ThT fluorescence negative, was used as a starting structure

for site-directed mutagenesis. The introduction of a single 4-tyrosine (Tyr) ladder induced fluorescence at 485 nm. A single mutation of the ladder residue from Tyrosine to Lysine or Isoleucine abolished the ThT fluorescence.[33] The crystal structure suggested that ThT was docking onto the surface of the tyrosine ladder.[33,42] Harel et al. showed that ThT bound to the peripheral site with two aromatic rings in coplanar conformation and packing parallel to the aromatic side chains around the binding site in the crystal structure of ThT/TcAChE.[12] Aromatic side chain stacking has been suggested to facilitate the ThT binding in all structures discussed above. Again, the ThT fluorescence did not necessarily arise from the determined structures in the last two cases.

4.2 Material and Methods

Materials

Water was purified by a Millipore Synergy 185 ultrapure online filter. 10 mM phosphate buffer (pH 7.55) was made from monobasic and dibasic sodium phosphate (Sigma-Aldrich, $\geqslant$ 99%) and was filtered through a 0.22 μm Stericup filter (Millipore). Stock ThT solution ($\sim$2 mM) was prepared by dissolving ultrapure grade ThT (AnaSpec, Cat No. 88306, $>$ 98% by HPLC, $>$ 95% by TLC) in phosphate buffer. This stock solution was then purified by hexane extraction (1:4 v/v, 10 times). Purified ThT stock solution was stored at 0 °C.

Expression and Incubation of α-Synuclein

Same protocols were used for αSyn expression and incubation as described in Chapter 3. After 6 days of incubation, samples were left quiescent at room temperature in dark for at least a week before bulk and single-molecule measurement. This incubation resulted in aggregates mainly consisted of elongated amyloid fibrils.[43] For the control experiment, ThT was added after the incubation, instead of at the beginning of the incubation.

Dynamic Light Scattering Measurement

ThT solutions of different concentrations were prepared by diluting purified ThT stock solution with 10 mM phosphate buffer (pH 7.55) or Millipore water. Solutions with different ionic strengths were obtained by addition of NaCl. All samples were filtered through 100 kDa centrifugal filter (Amicon Ultra, Millipore). ThT concentration was then determined with extinction coefficient of 36,000 $M^{-1}cm^{-1}$ at 412 nm. To get rid of dust and other contamination, round borosilicate DLS cuvettes (Kimble Glass) were first rinsed with plenty of Millipore water, and then centrifuged inversely until dry. The cleaned cuvettes were immediately sealed with Parafilm. Samples were injected into cleaned cuvettes and immediately sealed with hot glue and used in dynamic light scattering (DLS) measurement later. DLS measurements were carried out on a Nicomp Model 380 Particle Size Analyzer (Particle Sizing Systems), equipped with an ALV-6010 Multi-Tau autocorrelator (ALV GmbH, Langen, Germany) to expand the resolution from 64 to 128 channels. Temperature control was achieved by engaging the temperature-controlled sample chamber. Scattered light from the incident laser (λ=532 nm) was collected at 90° or 130°. At least three parallel measurements were taken for each sample.

Intensity autocorrelation function $g_2(t,x)$ was recorded during DLS measurement and was later converted to the field correlation function $g_1(t,x)$, using the Siegert relation as in Eq. 4.1:

$$g_1(t,x) \propto \sqrt{g_2(t,x)-1} \tag{4.1}$$

This autocorrelation function is a sum of exponential decays corresponding to different particle sizes as shown in Eq. 4.2:

$$g_1(t,x) = \int_0^\infty e^{-\tau t} f(\tau,x) d\tau \tag{4.2}$$

Fitting was carried out with Interior-Point Gradient (IPG) code earlier developed in the group, with local regularization in the decay time dimension.[14] A 61-point logarithmically spaced grid with decay time ranging from 0.001 to 1000 ms was used. The standard deviation during measurement was calculated in real time by the ALV-6010

autocorrelator. Transitional diffusion coefficient D_{t} can be determined with $D_{\mathrm{t}} = \tau/q^2$, where q is the scattering vector as expressed in Eq. 4.3.

$$q = \frac{4n\pi}{\lambda \sin\left(\frac{\theta}{2}\right)} \tag{4.3}$$

where n is the refractive index, and θ is the angle between incident beam and the detector. Assuming a spherical geometry for the particles, hydrodynamic radius, R_{H}, can be calculated with the Stokes-Einstein relation, as in Eq. 4.4.

$$R_{\mathrm{H}} = \frac{k_{\mathrm{B}}T}{6\pi\eta D_{\mathrm{t}}} \tag{4.4}$$

where k_B is the Boltzmann constant, and η is the solution viscosity.

Steady-state Fluorescence Measurement

Steady-state ThT fluorescence spectra were taken on a FluoroMax-3 fluorometer (Jobin-Yvon Horiba), equipped with an automatic polarizer set (Jobin-Yvon Horiba, model FL-1044). For the 2 D ThT fluorescence spectrum measurement, ultra-low volume cuvettes with short pathlength (∼1 mm, FluoroVettes, ALine) were used. The cuvette window is made of UV-transparent, highly hydrophobic cyclic olefin film. Using an adapter, cuvette was put at 45° angle in the cuvette holder. 2 D spectra were taken with an integration time of 1 s at each emission wavelength, with both the source and observation slits set to 5 nm.

Steady-state anisotropy excitation spectra were taken by activating the polarizer set. A quartz cuvette with 1 cm optical path was used. Integration time was 1 s at each excitation wavelength. Both source and observation slits were set to 3 nm. In each anisotropy measurement, fluorescence intensity was recorded with four different settings of the polarizer set: I_{VV} for vertical excitation and vertical emission; I_{HH} for horizontal excitation and horizontal emission; I_{VH} for vertical excitation and horizontal emission; I_{HV} for horizontal excitation and vertical emission. The different efficiency of detection channel with vertical and horizontal polarization is compensated with G factor, calculated as in Eq. 4.5:

$$G = \frac{I_{\mathrm{HV}}}{I_{\mathrm{HH}}} \tag{4.5}$$

The measured anisotropy, $< r >$, is defined as in Eq. 4.6:

$$< r >= \frac{I_{\mathrm{VV}} - G \times I_{\mathrm{VH}}}{I_{\mathrm{VV}} + 2 \times G \times I_{\mathrm{VH}}} \tag{4.6}$$

For the fluorescence titration measurement, a quartz cuvette with 1 cm optical path was used. Fresh ThT was titrated into the amyloid sample. Data fit was performed in Mathematica 7.0 (Wolfram), with correction for inner filter effect.

Single-molecule Fluorescence Microscopy Imaging

Same protocols for coverslip treatment and sample preparation were used as in Chapter 3. Same instrument setup was used as in Chapter 3, with following modification for polarization measurement: a sheet polarizer (New Port, model: 5511) was inserted between the quarter-wave plate and the dichroic mirror to obtain excitation with vertical and horizontal polarization. A polarizing cube was used to separate the collected fluorescence into vertical and horizontal polarizations, which were recorded in two separate detector channels (PerkinElmer, model SPC-AQR-15).

4.3 Results

4.3.1 Thioflavin T Aggregation States Probed by Dynamic Light Scattering

Non-invasive DLS technique was used to monitor the formation of nanometer-sized aggregates in ThT solutions. ThT solutions with concentrations ranging from $\sim$26 μM to $\sim$1000 μM, were prepared in 10 mM phosphate buffer (pH 7.55). For all the concentrations studied, the DLS autocorrelation decays obtained at room temperature were quite similar, and could not be distinguished from that of buffer blank, as shown in Fig. 4.2. The signal was so low that it mainly came from afterpulsing. The distribution of particle size confirmed that there was no essential change in the particle size with increasing ThT concentrations, as shown in Fig. 4.2 inset. The main size distribution peaks for all the solutions, including the buffer, showed up below the detection limit of DLS of $\sim$1 nm. They were mainly detector afterpulsing and fitting artifacts. With a dimension of ThT molecule mentioned before, the hydrodynamic radius of ThT molecule

should be under 1 nm, which is beyond the detection of current instrument setup.[44] The absence of any peak of radius > 1 nm in Fig. 4.2, indicates that no nanometer-sized aggregates existed in any of these solutions, even with a ThT concentration as high as 1000 μM. The particle size distribution of ThT solutions with different ionic strengths were measured in the same way. Again, no particle with radius > 1 nm was detected with NaCl concentrations ranging from 10 mM to 200 mM, as shown in Fig. 4.3. The decay curves mainly consisted of afterpulsing.

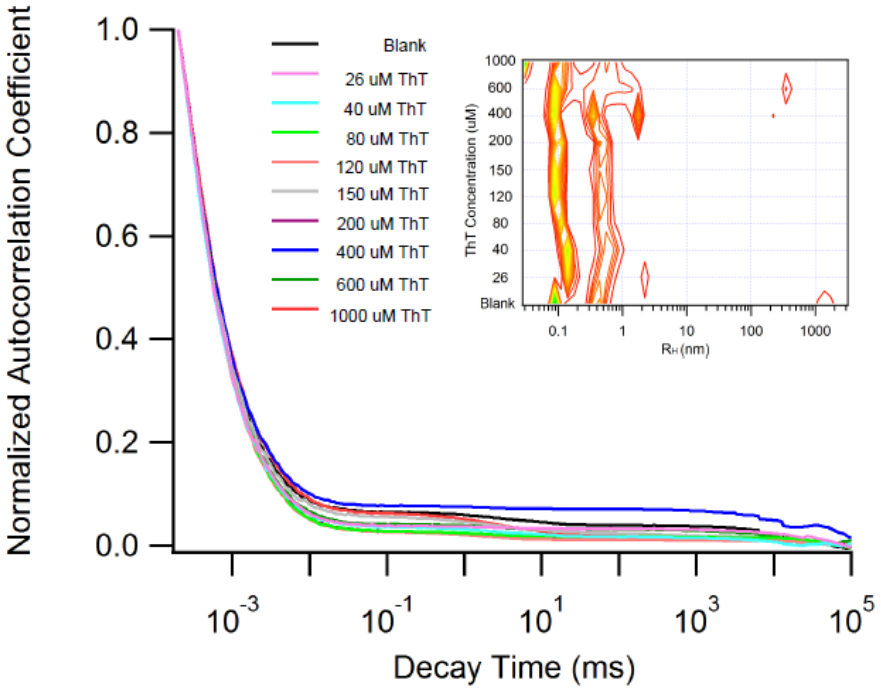

Figure 4.2: Autocorrelation decays obtained in DLS measurements for ThT solutions of different concentrations. Phosphate buffer was used as blank. Each curve was calculated by averaging at least three parallel measurements. Inset, the calculated hydrodynamic radius, R_{H} distribution by IPG fit. For all concentrations, the decay curves closely resemble one another, as well as the R_{H} distribution determined by fit. The signal was so low that the decay curves mainly consisted of afterpulsing.

To evaluate how temperature affected the ThT aggregation states, two parallel 40 μM ThT solutions were prepared in 10 mM, pH 7.55 phosphate buffer. One sample was stored at 60 °C overnight and the other at 22 °C. Distinctive decays were observed for these two samples, as shown in Fig. 4.4a. While no change was observed for the 22 °C sample, particles of 1 μm radius were observed in the 60 °C sample. Accompanying

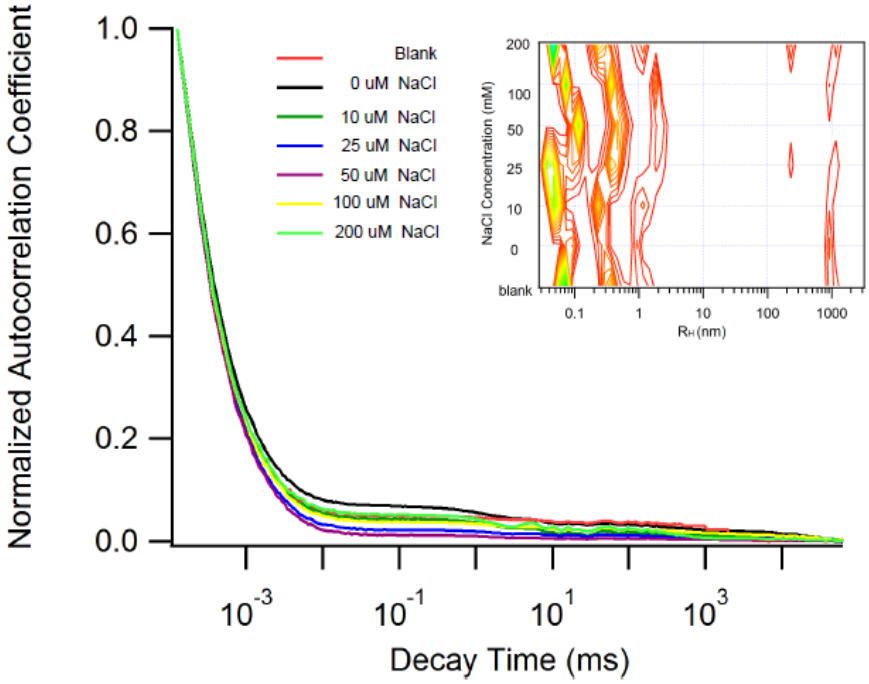

Figure 4.3: Autocorrelation decays obtained in DLS measurements for 40 μM ThT in phosphate buffer with different NaCl concentrations. Phosphate buffer was used as blank. Each curve was calculated by averaging at least 3 parallel measurements. Inset, the calculated hydrodynamic radius, R_{H}, distribution by IPG fit. For all NaCl concentrations, the decay curves closely resemble one another, as well as the R_{H} distribution determined by fit.

the appearance of these large aggregates, the yellow color of the ThT solution faded in the 60 °C sample, as shown in Fig. 4.4b. Large aggregates were observed in all ThT solutions with various concentrations after storing at 60 °C overnight, and their population increased with the increased concentrations, as shown in Fig. 4.4c. However, with comparable concentrations, solutions prepared by dissolving ThT in Millipore water seemed to be exempted from this aggregation process induced by heat denaturing, as shown in Fig. 4.4d. No peak was observed around 1 μm for all ThT concentrations and the yellow color stayed.

Fodera et al. showed that the absorbance of basic ThT solutions decreased with elongated incubation under 50 °C and the color of solutions disappeared accordingly.[45] This process was accelerated with increased pH and was only observed in solutions of pH >7.3. We found our DLS observation to be consistent with their study. While the

phosphate buffer has a slight basic pH of 7.55, dissolving of ThT in Millipore water would result in a pH around 7. While the decrease in ThT absorbance was caused by hydroxylation of ThT at basic pH, as suggested by Fodera et al., observation of large particles in Fig. 4.4 suggested that this process was accompanied with ThT aggregation.

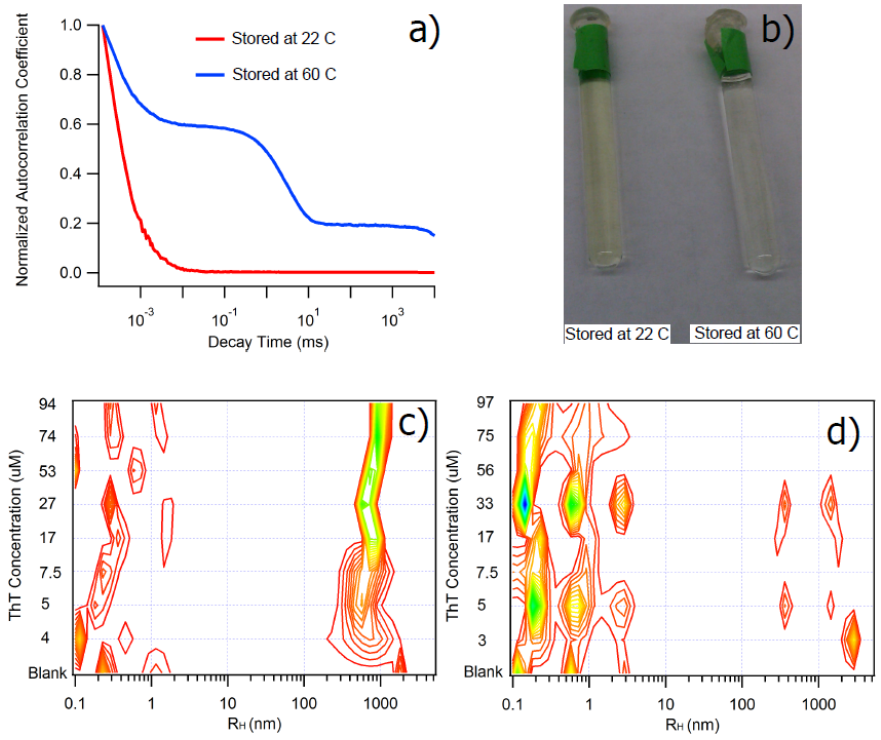

Figure 4.4: Aggregation of ThT induced by heat. a) DLS autocorrelation decays for 40 μM ThT in pH 7.55 phosphate buffer, stored at 60 °C and 22 °C overnight. b) Appearance of the two samples used for DLS measurement in a). The yellow color faded after storage at 60 °C. c) Calculated hydrodynamic radius distribution for different concentrations of ThT buffer solution after incubation at 60 °C overnight. An obvious peak appeared around ~1 μm and its intensity increased with increasing concentration. d) Calculated hydrodynamic radius distribution for different concentrations of ThT in Millipore water after incubation at 60 °C overnight. Compared with c), no aggregation was observed.

4.3.2 Steady-state Fluorescence Study on Aqueous Thioflavin T Solutions

2 D fluorescence spectra were taken for ~40 μM ThT in phosphate buffer, with excitation ranging from 380 nm to 460 nm, and emission ranging from 400 nm to 550 nm. A

weak fluorescence peak was observed around 482 nm, with excitation around 420 nm, as shown in Fig. 4.5a. After the measurement, the solution was decanted. 2 D spectrum was taken on the emptied cuvette with exact settings. The fluorescence feature at ∼420 nm excitation and ∼482 nm emission did not disappear. Instead, its intensity increased, as shown in Fig. 4.5c. This fluorescence peak stayed after washing with buffer, but was completely eliminated by washing with methanol, as shown in Fig. 4.5d. Same results were obtained for solutions of 60 μM, 80 μM and 100 μM ThT. The fluorescence at ∼420 nm excitation and ∼482 nm emission was thus determined to come from ThT bound to the cuvette window surface, but not solution phase ThT. While the signal from solution phase ThT was too low to detect, the fluorescence spectra were dominated by surface effect. The intensity enhancement after emptying the cuvette could be explained by removal of the inner filter effect, which was caused by absorption of concentrated solution phase ThT. Without ThT solution, excitation intensity at the surface increased, and resulted in increased fluorescence intensity. ThT has better solubility in methanol than in water. Rinsing with methanol removed ThT from the cuvette window surface and thus abolished the fluorescence.

4.3.3 Steady-state Fluorescence Study on Thioflavin T in Presence of Amyloid Fibrils

Thioflavin T Fluorescence Spectra upon Binding to Amyloid Fibrils

αSyn amyloid fibrils were used to study ThT fluorescence upon binding to amyloid fibrils. ThT was added before the incubation. Upon binding to αSyn fibrils, characteristic ThT fluorescence with excitation maximum at ∼445 nm and emission maximum at ∼476 nm was detected, as shown in Fig. 4.6

Dependence of Fluorescence Upon Thioflavin T Concentration

αSyn incubations with and without ThT were prepared. According to AFM measurement, both incubations resulted in aggregation with major population of amyloid fibrils with indistinguishable morphologies. Concentration dependence of fluorescence

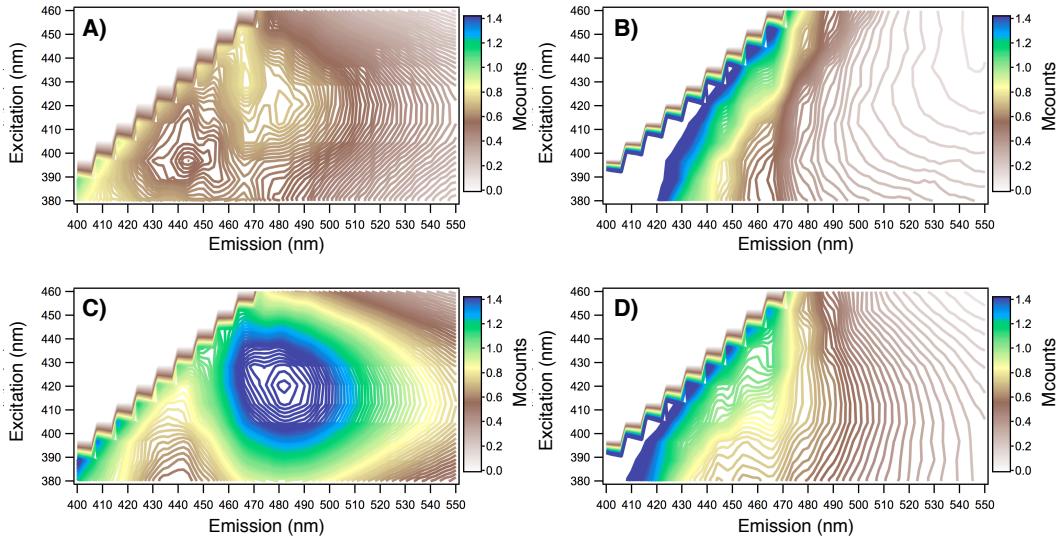

Figure 4.5: 2 D fluorescence spectra of aqueous ThT solution. A) Measurement taken on cuvette filled up with ∼40 μM ThT in 10 mM, pH 7.55 phosphate buffer. A fluorescence peak showed up with excitation at ∼420 nm and emission at ∼482 nm. B) Measurement taken on cuvette filled up with 10 mM, pH 7.55 phosphate buffer. No fluorescence peak was observed. C) Measurement taken on the same cuvette after decanting the ThT solution. The fluorescence peak stayed at the same position with increased intensity. D) Measurement taken after rinsing the cuvette with 50 μL methanol for three times. The fluorescence peak was removed.

intensity at 476 nm was determined by titrating ThT into αSyn amyloid fibrils. Three models were used to fit this titration curve, which are summarized in Fig. 4.7. 1) The fluorescent monomer model, which states that ThT monomers become fluorescent upon binding to fibrils. 2) The fluorescent dimer model, which states that pre-existing ThT dimers become fluorescent upon binding to fibrils. 3) The coupled exciton model, which states that ThT monomers bind to fibrils first. Two ThT monomers sitting close to each other on the fibril then form the fluorescent exciton. The reactions and constrains involved in each model are summarized in Scheme 1. In the monomer model, ThT monomers, T, react with the binding sites on amyloid fibrils, S, to produce fluorescence Fl. In the dimer model, two ThT monomers react to form dimer, T_2, in solution. T_2 then interaction with the binding site to produce fluorescence. In in the exciton model, ThT monomer bound to the binding site to form B. P is the ratio of number of

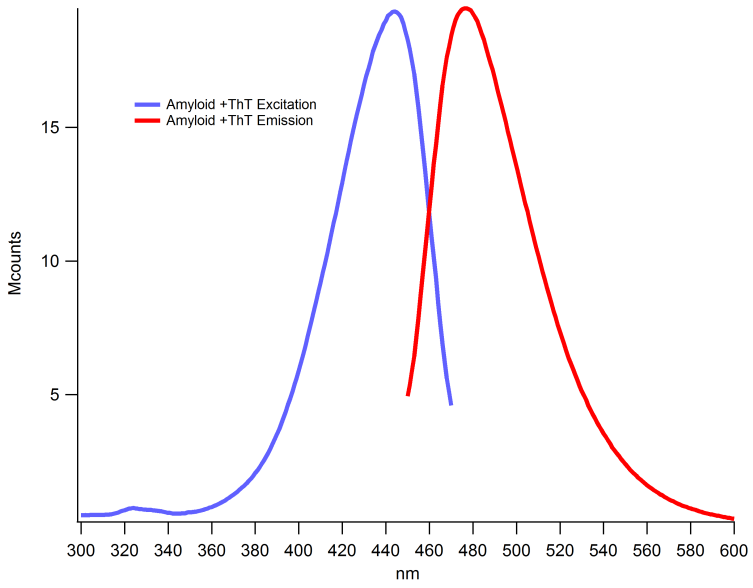

Figure 4.6: Characteristic ThT fluorescence upon binding to αSyn amyloid fibrils. 5 μM ThT was added in amyloid incubation for *in situ* measurement.

occupied binding site to the initial number of binding sites, S_0. The probability of two ThT sitting at adjacent binding site to form exciton is $2P - P^2$. Each of these models leads to different fluorescence intensity dependence on ThT concentration.

The fluorescence titration curve and best fit of each model are shown in Fig. 4.8. The monomer model fit the data best. The dimer model began to follow the data point with concentrations above 1 μM. At high concentrations, the monomer and dimer model fit overlay with each other. However, the K_a obtained for dimer model was of 80,000 times of the K_f. This implied a big population of unbounded dimers in the solution, which was negated by absorption spectrum of ThT. The coupled exciton model did not track the data points at all. The concentration dependence of the fluorescence intensity revealed ThT monomer as the fluorescent species. To determine the chirality of the fluorescent species, CD spectra were collected in parallel with the fluorescence measurement. No CD signal was detected.

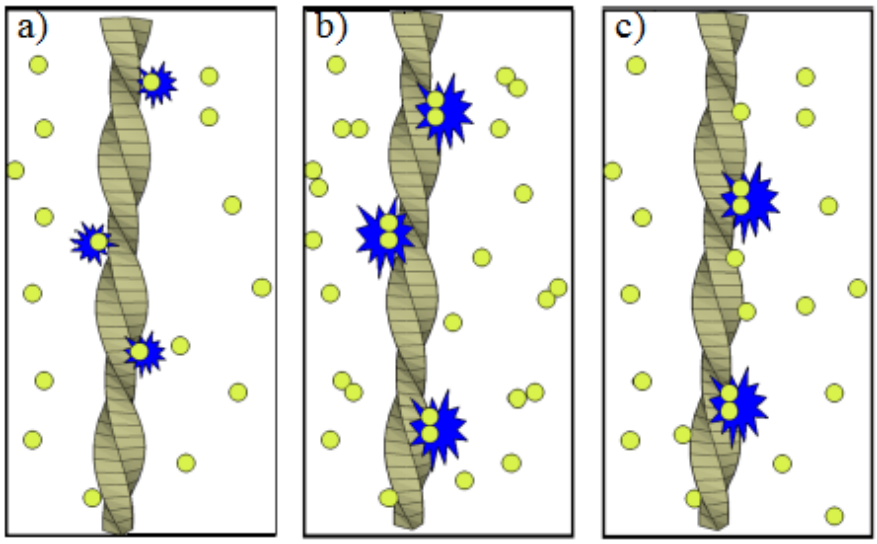

Figure 4.7: Three models used to fit the ThT fluorescence titration curve. a) Fluorescent monomer model. Only monomers exist in solution. Upon binding to fibrils, monomers become fluorescent. b) Fluorescent dimer model. Monomers and dimers are in equilibrium in the solution. Dimers bind to fibrils and become fluorescent. c) Coupled exciton model. Only monomers exist in solution. Monomers bind to fibril without fluorescence. Only when fibril-bound monomers sit next to each to form excitons, they become fluorescent.

$$T + S \overset{K_f}{\rightleftharpoons} Fl$$

a) Monomer model

$$T + T \overset{K_a}{\rightleftharpoons} T_2$$

$$T_2 + S \overset{K_f}{\rightleftharpoons} Fl$$

b) Dimer model

$$T + S \overset{K_b}{\rightleftharpoons} B$$

$$P = B/S_0$$

$$Fl = B(2P - P^2)$$

c) Exciton model

Scheme 1

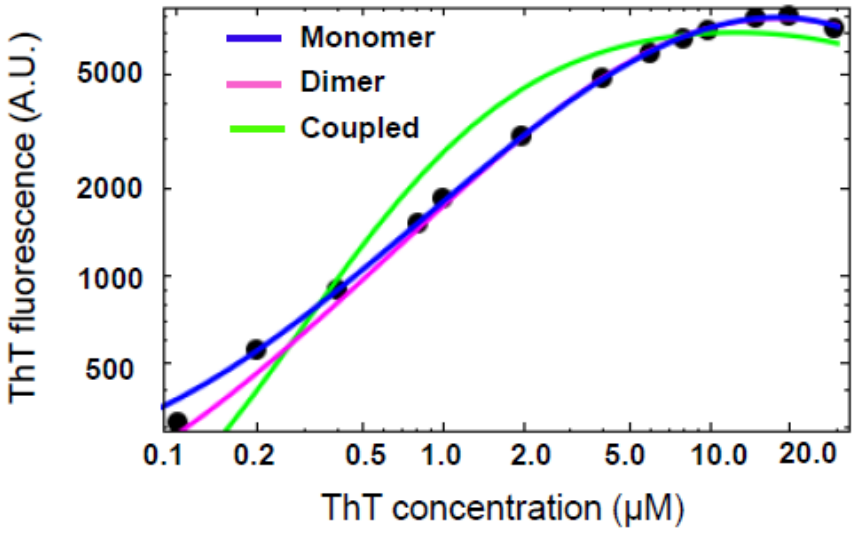

Figure 4.8: Concentration dependence of ThT fluorescence intensity at 476 nm. The data was plot without correction for internal filter effect. The correction was performed during the fit. Providing the best fit to the titration data, monomer was determined as the fluorescent species

Excitation Anisotropy Spectra of Thioflavin T Bound to Amyloid Fibrils

Excitation anisotropy spectra were taken for ThT in presence of αSyn amyloid fibrils, with detection at 476 nm. The anisotropy was $\sim$0.36 at $\sim$445 nm, as shown in Fig. 4.9. The anisotropy was pretty consistent within this excitation peak. Anisotropy is used to measure the angle between excitation moment upon excitation and emission moment at the time of emission. The higher the anisotropy, the smaller the angle between the two. For a system in which the fluorophore excitation and emission moments are perfectly aligned and experiences no depolarization by rotational diffusion, the anisotropy is 0.4. The slow rotation of large, rigid fibrils between excitation and emission could only result in limited depolarization of the anisotropy. An anisotropy as high as 0.36 indicated that the angle between the two transition moments of ThT was small. Control experiments on ThT alone and ThT added to fresh αSyn solution without incubation showed very low fluorescence intensity.

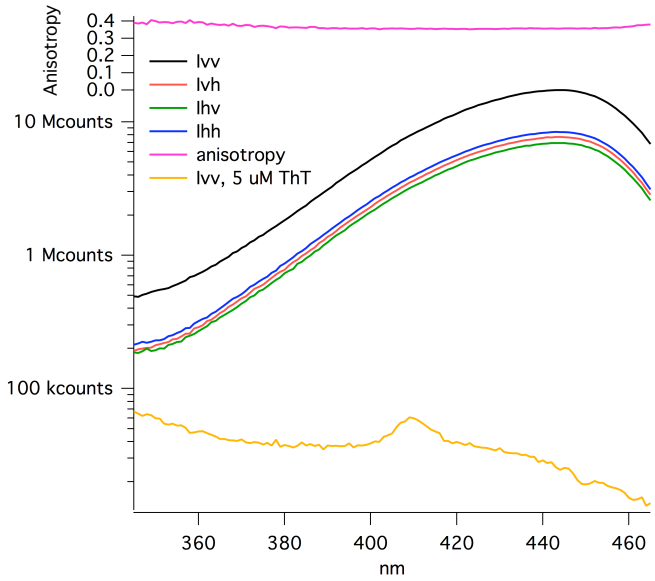

Figure 4.9: Steady-state fluorescence anisotropy excitation spectrum of ThT bound to αSyn amyloid fibrils. With detection at 476 nm, the excitation was scanned over 350 nm to 470 nm with different polarizer settings of excitation and emission. I_{HH} recorded the horizontal polarization component of fluorescence with horizontal excitation, and I_{HV} measured the vertical component. G factor for the system was determined at each wavelength as $I_{\mathrm{HV}}/I_{\mathrm{HH}}$. With vertically polarized excitation, I_{VV} was obtained for vertically polarized fluorescence and I_{VH} for the horizontal component. The main excitation peak for fibril-bound ThT was at $\sim$445 nm. The anisotropy was pretty consistent within the wavelength range of the main excitation peak, with a value of 0.36. Same measurements were taken on 5 μM ThT in pH 7.55, 10 mM phosphate buffer to compare with ThT fluorescence in presence of fibrils. Without amyloid fibrils, ThT fluorescence signal was much lower compared with that of the amyloid sample, and the water Raman peak was visible at $\sim$410 nm.

4.3.4 Single-molecule Fluorescence Polarization Imaging of α-Synuclein Amyloid Fibrils

Single-molecule Fluorescence Intensity Imaging

Single-molecule fluorescence imaging was used to study the property of ThT specifically bound to αSyn amyloid fibrils. αSyn fibrils were immobilized on APTES modified glass coverslip during scanning. Different areas of the coverslip were then scanned with 457.9 nm excitation. Emission $>$ 475 nm was collected. ThT-stained fibrils were imaged with enhanced fluorescence intensity than the background, as shown in Fig. 4.10a.

The fluorescence images captured the morphology features of amyloid fibrils: fibrils were of various lengths, straight and unbranched. However, since the obtained images were convolution of nanometer sized fibrils with ∼300 nm sized focal volume, fibrils in fluorescence images looked more like rods.

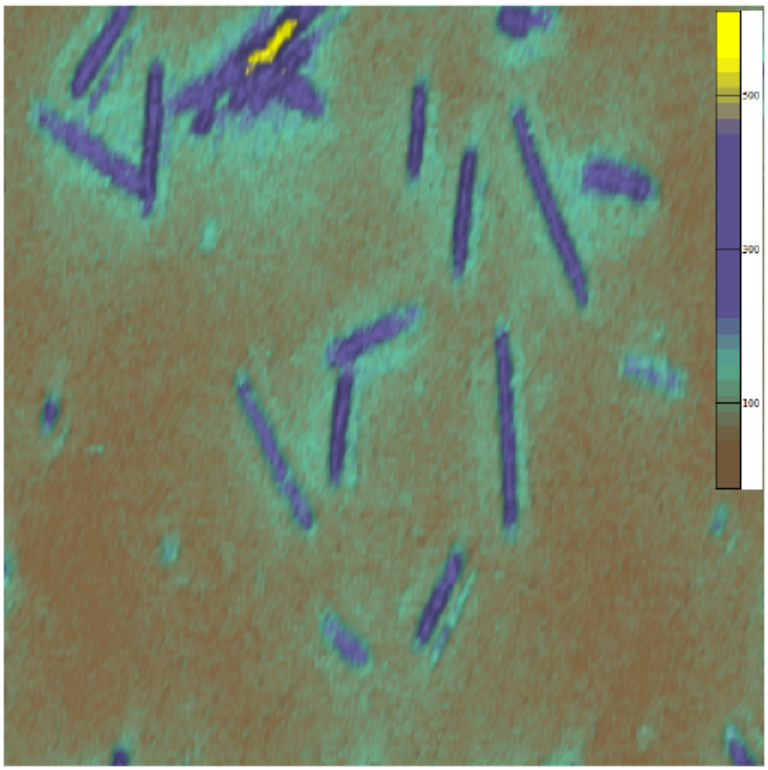

Figure 4.10: A typical single-molecule fluorescence intensity image of αSyn fibrils stained with ThT. The scan area was 18 μm × 18 μm, with a resolution of 128 pixel × 128 pixel. Fibrils were imaged on the surface, with various lengths up to several micrometers. The fibril lateral dimension was broadened in the fluorescence image, as a result of convolution with the objective focal volume.

Single-molecule Fluorescence Polarization Imaging

Single-molecule fluorescence intensity images successfully captured fibrils with enhanced ThT fluorescence intensity. According to results in Chapter 3, ThT need to be held rigidly to produce enhanced fluorescence. Thus, the ThT fluorescence polarization should be determined by the host, amyloid fibrils. On this basis, the ThT and fibril interaction was studied by polarization imaging. For polarization measurements, the

emission was separated into two orthogonal polarizations, P_{x} and P_{y}, and collected by two detectors. Px and P_{y} corresponded to the direction of x and y axis of the collected images, respectively. For each single-molecule fluorescence polarization measurement, three scans were made over the same area, with excitation of circular polarization and linear polarization of orientation P_{x} and P_{y}. With detection in two channels, six intensity images were obtained during each measurement. A typical data set obtained by one single-molecule fluorescence polarization imaging measurement is shown in Fig. 4.11. With circularly polarized excitation, two intensity images, I_{cx} and I_{cy}, were collected for P_{x} and P_{y} emission, as shown in Fig. 4.11a and b. A new image, I_{cf}, was constructed to show the overall fluorescence intensity without discrimination of polarization by adding up I_{cx} and I_{cy} pixel by pixel, as shown in Fig. 4.11c. Using excitation P_{x}, a second scan generated two images, I_{xx} and I_{xy}, with emission separated into two components, as shown in Fig. 4.11d and e. The total intensity image was constructed the same way as for I_{cf}, by adding up I_{xx} and I_{xy}, as shown in Fig. 4.11f. A third scan was carried out over the same area with excitation polarization P_{y}. Again, two emission polarization components were recorded in two images, I_{yx} and I_{yy}, as shown in Fig. 4.11g and h. I_{yf} was the constructed intensity image from I_{yx} and I_{yy}, as shown in Fig. 4.11i.

The fluorescence intensity of the same fibril varied from image to image in the data set. This variation depended on the orientation of fibrils in the images. Take the fibril in the red box in Fig. 4.11 as an example, this fibril lied almost parallel to the x axis of the scan area. With circularly polarized excitation, this fibril was observed in I_{cx}, but completely disappeared in I_{cy}. When illuminated, only the fluorophores with their excitation dipole aligned parallel to the excitation polarization could be excited. When the excitation was circularly polarized, all ThT molecules should have the same possibility to be excited, regardless of their orientations. Thus, the fibril in the red box should have been excited as other fibrils in I_{cy}. The disappearance of this fibril in I_{cy} can only be explained by a close alignment of ThT emission dipole to the fibril long axis, and consequently to the x axis of the scan area. Upon excitation, ThT molecules bound to this fibril emitted strictly with a polarization of P_{x}, which resulted in zero signal in the orthogonal P_{y} detection channel.

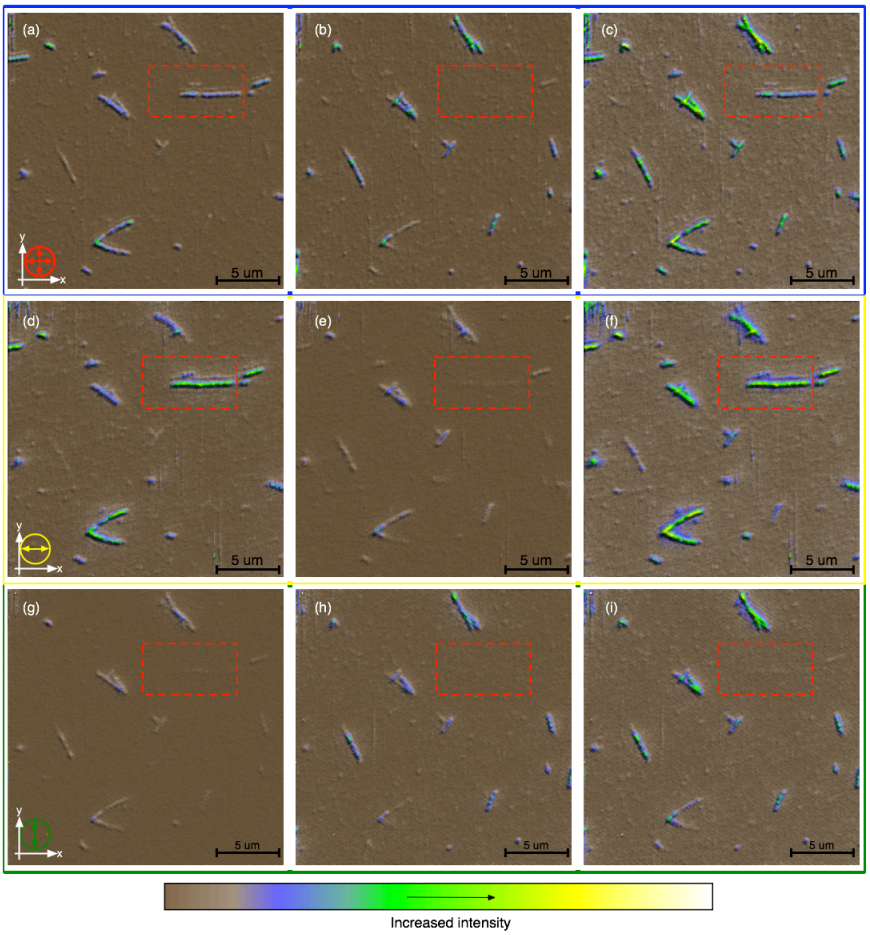

Figure 4.11: Single-molecule fluorescence images of ThT bound to αSyn amyloid fibrils over the same 20 $\times$ 20 μm area (256 $\times$ 256 pixel) with different polarization configurations. Excitation wavelength was 457.9 nm and emission $>$ 475 nm was collected. Circularly polarized excitation was used for (a) I_{cx} and (b) I_{cy}. During one scan, the emission polarization component parallel to x axis was recorded in (a) and parallel to y axis in (b), respectively. (c) I_{cf} is the constructed image by adding up signal (a) and (b) pixel by pixel. (d) I_{xx} and (e) I_{xy} were taken during a scan with P_{x} excitation, with (d) recording emission polarization component of P_{x}, and (e) for P_{y}. (f) I_{xf} was constructed by pixel to pixel addition of (d) and (e). (g) I_{yx} and (h) I_{yy} were taken during a scan with P_{y} excitation, with (g) recording emission polarization component of P_{x}, and (h) of P_{y}. (i) I_{yf} was constructed from (g) and (h). The fibril in the red box is discussed as an example in the body text.

This conclusion is further supported by I_{xy} in Fig. 4.11e, where the fibril disappeared again in the P_y detection channel, even though it was excited as indicated by Fig. 4.11f. Comparing I_{xf} with I_{yf} in Fig. 4.11f and i, it is clear that this fibril was only excited with polarization parallel to its long axis, but not polarization orthogonal to it. No signal from this fibril was detected in either channel with excitation of P_y, as in Fig. 4.11g and h, indicating that the fibril was not excited at all. This leads to the conclusion that the excitation dipole of ThT is also closely aligned with the fibril long axis. For fibrils oriented in other directions other than aligned to either of the two axes, ThT fluorescence was detected in all images. For linearly polarized excitations, the smaller the angle between the fibril long axis and the excitation polarization, the larger the efficiency, as reflected by higher fluorescence intensity. Same principle for the detection, the smaller the angle between the fibril orientation and the detection polarization, the larger the signal for that channel. In conclusion, both the excitation and emission dipole moments of fluorescent ThT are aligned along the fibril. Since the excitation dipole has been determined to lie parallel to the long molecular axis of ThT,[21] ThT binds to αSyn fibrils with its long molecular axis aligned with fibril long axis.

4.4 Discussion

Evaluation of Thioflavin T Fluorescence Mechanisms

Sabate et al. proposed the fluorescent micelle model based on observation of pre-existing micelles in ThT solutions.[38] The evidence used for micelle formation was a break in the concentration dependence of conductivity, which was actually an artifact caused by instrumental limitation. The observation of globular particles on mica surface could be artifact caused by sample preparation in their study. AFM samples were prepared by directly blowing dry the sample deposited on mica surface, without rinsing. The observed globular particles were likely nanocrystals formed on the surface during drying. With a different AFM sample preparation protocol, in which the surface was fully rinsed before drying, no globular particle was observed attached to αSyn fibrils during AFM imaging.[43] No particles with hydrodynamic radius larger than 1 nm was observed during

DLS measurement for solution conditions commonly used in amyloid studies. ThT aggregation was only induced by heat denaturation. However, this process is irrelevant with observed ThT fluorescence in amyloid studies. In a word, no micelle exists in ThT solutions used for amyloid studies and it can not be the fluorescent species. The fluorescence titration result, as shown in Fig. 4.8, negates the exciton model proposed by Raj et al, and indicated the ThT monomers as fluorescent species.

Lindgren et al. used the fluorescent molecular rotor model to explain the increased quantum yield of ThT upon binding to amyloid fibrils.[19,28] According to results in Fig. 4.5, ThT quantum yield was greatly enhanced upon binding to surface. In the 2 D fluorescence spectra of ThT aqueous solution, only fluorescence from ThT bound to the cuvette surface was observed. This was consistent with ThT working as a molecular rotor. In the low viscosity aqueous ThT solution, fast intramolecular rotation between the benzthiazole and dimethylaminobenzene ring happened before emission from the local fluorescent excited states, which resulted in the relaxation of ThT to the non-fluorescent TICT state. The solution phase ThT was thus practically nonfluorescent. Upon binding to the cuvette surface, the intramolecular rotation was hindered, and ThT relaxed from the local fluorescent excited state.

Binding of ThT to the coverslip was also indicated by increased fluorescence intensity compared with control experiment in single-molecule measurements in Chapter 3. Same lifetime features were observed for surface-bound ThT and amyloid fibril-bound ThT. The surface-bound ThT was observed with excitation at $\sim$420 nm as shown in Fig. 4.5, while the excitation maximum red shifted to $\sim$445 nm for fibril-bound ThT. Unlike the lifetime, the spectral shift of ThT was regulated by the local environment. As a result, even though the surface-bound and fibril-bound ThT had similar quantum yield and lifetime features, fibrils were imaged with enhanced intensity against the low intensity background. 457.9 nm excitation illuminated fibril-bound ThT more efficiently since this wavelength was close to the fibril-bound ThT excitation maximum, but away from that of surface-bound ThT; Emission $>$ 475 nm was collected, which covered the emission maximum in both cases.

Re-evaluation of Reported Thioflavin T Photophysical Properties

The otherwise insignificant surface effect predominated the aqueous ThT solution fluorescence spectra, as a result of low quantum yield in solution phase and high quantum yield on the surface. To monitor the photophyiscal properties of ThT, it is very important to evaluate the surface effect, especially for solutions with low viscosity. The discrepancy between absorption and excitation maximum has been observed for ThT in many solvents, such as water and alcohols, which raises confusion in the determination of ThT photophysical properties.[3] According to Fig. 4.5, this discrepancy is actually an artifact caused by the surface effect: the absorption peak arises from solution phase ThT, while the excitation measured is for the ThT bound to the cuvette surface. Only in high viscosity solutions, such as glycerol, this discrepancy disappears.[3] In solutions of high viscosity, the detected fluorescence is from the solution phase ThT with high quantum yield. Maskevich et al. evaluated the effect of solvent polarity on ThT photophysical properties in 14 different solvents.[18] Excitation different than the absorption maximum of each solution was used. With low viscosity of most solvent studied, the determined quantum yields were pretty low, mostly under 0.001. The presence of surface effect in these data calls for a re-evaluation of the ThT photophysical properties in these solution.

The spectral properties that has been determined in this chapter and other studies can be summarized as: First, absorption maximum of ThT shifts from 412 nm to 445 nm upon binding to fibrils in aqueous solutions. Second, no fluorescence spectra have been determined for ThT in aqueous solution because of low quantum yield. Fluorescence data are only available for solutions with high viscosity, such as glycerol (421 nm excitation, 493 nm emission) and for ThT bound to surface, such as cyclic olefin film(420 nm excitation, 482 nm emission). Third, upon binding to αSyn amyloid fibrils, the excitation shifts to 445 nm, and emission to 476 nm. Negative solvatochromism might be one of the factors that determine the ThT spectral shift. With decreased polarity of the microenvironment, ThT absorption shifts to longer wavelength.

Alignment of Thioflavin T Along α-Synuclein Amyloid Fibrils

ThT was shown to bind αSyn amyloid fibrils with its excitation and emission dipole moments parallel to the long axis of the fibrils, with single-molecule polarization imaging. ThT excitation dipole moment lies parallel to its long structural axis, and thus ThT molecule should bind αSyn fibrils with its long axis aligned to the fibril axis.[21] This is consistent with the observed binding orientation of ThT to insulin amyloid fibrils and PSAM scaffold.[21,33] Biancalana et al. suggested that ThT docked onto channels formed by a single cross-strand tyrosine ladder along the β-sheet, based on PSAM crystal structure. In this model, ThT is held in a planar conformation by stacking interaction of two aromatic rings in ThT with tyrosine aromatic side chains.[33] However, without structural details on αSyn amyloid fibrils, exact binding sites for ThT on αSyn amyloid fibrils can not be determined.

Bibliography

[1] M. Groenning. Binding mode of thioflavin T and other molecular probes in the context of amyloid fibrils-current status. *J. Chem. Biol.*, 3(1):1–18, 2009.

[2] H. LeVine. Thioflavine T interaction with synthetic Alzheimer's disease β-amyloid peptides: detection of amyloid aggregation in solution. *Protein Sci.*, 2(3):404–410, 1993.

[3] E. S. Voropai, M. P. Samtsov, K. N. Kaplevskii, A. A. Maskevich, V. I. Stepuro, O. I. Povarova, I. M. Kuznetsova, K. K. Toroverov, A. L. Fink, and V. N. Uverskii. Spectral properties of thioflavin T and its complexes with amyloid fibrils. *J. Appl. Spectrosc.*, 70:868–874, 2003.

[4] P. S. Vassar and C. F. Culling. Fluorescent stains, with special reference to amyloid and connective tissues. *Arch. Pathol.*, 68:487–498, 1959.

[5] H. Naiki, K. Higuchi, M. Hosokawa, and T. Takeda. Fluorometric determination of amyloid fibrils in vitro using the fluorescent dye, thioflavin T1. *Anal. Biochem.*, 177(2):244–249, 1989.

[6] L. Nielsen, R. Khurana, A. Coats, S. Frokjaer, J. Brange, S. Vyas, V. N. Uversky, and A. L. Fink. Effect of environmental factors on the kinetics of insulin fibril formation: elucidation of the molecular mechanism. *Biochemistry*, 40(20):6036–6046, 2001.

[7] M. Manno, M. Mauro, E. F. Craparo, A. Podest, D. Bulone, R. Carrotta, V. Martorana, G. Tiana, and P. L. San Biagio. Kinetics of different processes in human insulin amyloid formation. *J. Mol. Biol.*, 366(1):258–274, 2007.

[8] M. Groenning, M. Norrman, J. M. Flink, M. van de Weert, J. T. Bukrinsky,

G. Schluckebier, and S. Frokjaer. Binding mode of thioflavin T in insulin amyloid fibrils. *J. Struct. Biol.*, 159(3):483–497, 2007.

[9] C. C. Kitts and D. A. V. Bout. Near-field scanning optical microscopy measurements of fluorescent molecular probes binding to insulin amyloid fibrils. *J. Phys. Chem. B*, 113(35):12090–12095, 2009.

[10] C. B. Andersen, H. Yagi, M. Manno, V. Martorana, T. Ban, G. Christiansen, D. E. Otzen, Y. Goto, and C. Rischel. Branching in amyloid fibril growth. *Biophys. J.*, 96(4):1529–1536, 2009.

[11] R. Sabat and S. J. Saupe. Thioflavin T fluorescence anisotropy: an alternative technique for the study of amyloid aggregation. *Biochem. Biophys. Res. Commun.*, 360(1):135–138, 2007.

[12] M. Harel, L. K. Sonoda, I. Silman, J. L. Sussman, and T. L. Rosenberry. Crystal structure of thioflavin T bound to the peripheral site of Torpedo californica acetylcholinesterase reveals how thioflavin T acts as a sensitive fluorescent reporter of ligand binding to the acylation site. *J. Am. Chem. Soc.*, 130(25):7856–7861, 2008.

[13] L. S. Wolfe, M. F. Calabrese, A. Nath, D. V. Blaho, A. D. Miranker, and Y. Xiong. Protein-induced photophysical changes to the amyloid indicator dye thioflavin T. *Proc. Natl. Acad. Sci. U. S. A.*, 107(39):16863–16868, 2010.

[14] J. T. Giurleo, X. He, and D. S. Talaga. Beta-lactoglobulin assembles into amyloid through sequential aggregated intermediates. *J. Mol. Biol.*, 381(5):1332–1348, 2008.

[15] A. L. Cloe, J. P. R. O. Orgel, J. R. Sachleben, R. Tycko, and S. C. Meredith. The Japanese mutant Aβ(δE22-Aβ(1-39)) forms fibrils instantaneously, with low-thioflavin T fluorescence: seeding of wild-type Aβ(1-40) into atypical fibrils by δE22-A(1-39). *Biochemistry*, 50(12):2026–2039, 2011.

[16] M. Biancalana and S. Koide. Molecular mechanism of thioflavin T binding to amyloid fibrils. *Biochim. Biophys. Acta.*, 1804(7):1405–1412, 2010.

[17] M. Sunde, L. C. Serpell, M. Bartlam, P. E. Fraser, M. B. Pepys, and C. C. Blake. Common core structure of amyloid fibrils by synchrotron X-ray diffraction. *J. Mol. Biol.*, 273(3):729–739, 1997.

[18] A. A. Maskevich, V. I. Stsiapura, V. A. Kuzmitsky, I. M. Kuznetsova, O. I. Povarova, V. N. Uversky, and K. K. Turoverov. Spectral properties of thioflavin T in solvents with different dielectric properties and in a fibril-incorporated form. *J. Proteome Res.*, 6(4):1392–1401, 2007.

[19] V. I. Stsiapura, A. A. Maskevich, V. A. Kuzmitsky, V. N. Uversky, I. M. Kuznetsova, and K. K. Turoverov. Thioflavin T as a molecular rotor: fluorescent properties of thioflavin T in solvents with different viscosity. *J. Phys. Chem. B*, 112(49):15893–15902, 2008.

[20] C. Rodrguez-Rodrguez, A. Rimola, L. Rodrguez-Santiago, P. Ugliengo, A. Alvarez-Larena, H. Gutirrez de Tern, M. Sodupe, and P. Gonzlez-Duarte. Crystal structure of thioflavin T and its binding to amyloid fibrils: insights at the molecular level. *Chem. Commun.*, 46(7):1156–1158, 2010.

[21] M. R. H. Krebs, E. H. C. Bromley, and A. M. Donald. The binding of thioflavin T to amyloid fibrils: localisation and implications. *J. Struct. Biol.*, 149(1):30–37, 2005.

[22] G. V. De Ferrari, W. D. Mallender, N. C. Inestrosa, and T. L. Rosenberry. Thioflavin T is a fluorescent probe of the acetylcholinesterase peripheral site that reveals conformational interactions between the peripheral and acylation sites. *J. Biol. Chem.*, 276(26):23282–23287, 2001.

[23] L. R. Naik, A. B. Naik, and H. Pal. Steady-state and time-resolved emission studies of Thioflavin T. *J. Photochem Photobio A*, 204:161–167, 2009.

[24] W. Dzwolak and M. Pecul. Chiral bias of amyloid fibrils revealed by the twisted conformation of thioflavin T: an induced circular dichroism/DFT study. *FEBS Lett.*, 579(29):6601–6603, 2005.

[25] M. Ilanchelian and R. Ramaraj. Emission of thioflavin T and its control in the presence of DNA. *J. Photochem. Photobio. A*, 162(1):129–137, 2004.

[26] C. R. Raj and R. Ramaraj. γ-Cyclodextrin induced intermolecular excimer formation of thioflavin T. *Chem. Phys. Lett.*, 273:285–290, 1997.

[27] P. Friedhoff, A. Schneider, E. M. Mandelkow, and E. Mandelkow. Rapid assembly of Alzheimer-like paired helical filaments from microtubule-associated protein tau monitored by fluorescence in solution. *Biochemistry*, 37(28):10223–10230, 1998.

[28] M. Lindgren, K. Srgjerd, and P. Hammarstrm. Detection and characterization of aggregates, prefibrillar amyloidogenic oligomers, and protofibrils using fluorescence spectroscopy. *Biophys. J.*, 88(6):4200–4212, 2005.

[29] R. Khurana, C. Coleman, C. Ionescu-Zanetti, S. A. Carter, V. Krishna, R. K. Grover, R. Roy, and S. Singh. Mechanism of thioflavin T binding to amyloid fibrils. *J. Struct. Biol.*, 151(3):229–238, 2005.

[30] M. Groenning, L. Olsen, M. van de Weert, J. M. Flink, S. Frokjaer, and F. S. Jrgensen. Study on the binding of thioflavin T to β-sheet-rich and non-β-sheet cavities. *J. Struct. Biol.*, 158(3):358–369, 2007.

[31] V. I. Stsiapura, A. A. Maskevich, S. A. Tikhomirov, and O. V. Buganov. Charge transfer process determines ultrafast excited state deactivation of thioflavin T in low-viscosity solvents. *J. Phys. Chem. A.*, 114(32):8345–8350, 2010.

[32] A. Srivastava, P. K. Singh, M. Kumbhakar, T. Mukherjee, S. Chattopadyay, H. Pal, and S. Nath. Identifying the bond responsible for the fluorescence modulation in an amyloid fibril sensor. *Chemistry*, 16(30):9257–9263, 2010.

[33] M. Biancalana, K. Makabe, A. Koide, and S. Koide. Molecular mechanism of thioflavin T binding to the surface of β-rich peptide self-assemblies. *J. Mol. Biol.*, 385(4):1052–1063, 2009.

[34] C. Blake and L. Serpell. Synchrotron X-ray studies suggest that the core of the

transthyretin amyloid fibril is a continuous β-sheet helix. *Structure*, 4(8):989–998, 1996.

[35] M. F. Perutz, J. T. Finch, J. Berriman, and A. Lesk. Amyloid fibers are water-filled nanotubes. *Proc. Natl. Acad. Sci. U. S. A.*, 99(8):5591–5595, 2002.

[36] L. C. Serpell, J. Berriman, R. Jakes, M. Goedert, and R. A. Crowther. Fiber diffraction of synthetic α-synuclein filaments shows amyloid-like cross-β conformation. *Proc. Natl. Acad. Sci. U. S. A.*, 97(9):4897–4902, 2000.

[37] R. Nelson, M. R. Sawaya, M. Balbirnie, A. Madsen, C. Riekel, R. Grothe, and D. Eisenberg. Structure of the cross-β spine of amyloid-like fibrils. *Nature*, 435(7043):773–778, 2005.

[38] R. Sabat, I. Lascu, and S. J. Saupe. On the binding of thioflavin T to HET-s amyloid fibrils assembled at pH 2. *J. Struct. Biol.*, 162(3):387–396, 2008.

[39] J. Wall, C. L. Murphy, and A. Solomon. In vitro immunoglobulin light chain fibrillogenesis. *Methods Enzymol.*, 309:204–217, 1999.

[40] A. Loksztejn and W. Dzwolak. Chiral bifurcation in aggregating insulin: an induced circular dichroism study. *J. Mol. Biol.*, 379(1):9–16, 2008.

[41] A. Loksztejn and W. Dzwolak. Vortex-induced formation of insulin amyloid superstructures probed by time-lapse atomic force microscopy and circular dichroism spectroscopy. *J. Mol. Biol.*, 395(3):643–655, 2010.

[42] M. Biancalana, K. Makabe, and S. Koide. Minimalist design of water-soluble cross-β architecture. *Proc. Natl. Acad. Sci. U. S. A.*, 107(8):3469–3474, 2010.

[43] J. Pronchik, X. He, J. T. Giurleo, and D. S. Talaga. In vitro formation of amyloid from α-synuclein is dominated by reactions at hydrophobic interfaces. *J. Am. Chem. Soc.*, 132(28):9797–9803, 2010.

[44] M. Kaszuba, D. McKnight, M. T. Connah, F. K. McNeil-Watson, and U. Nobbmann. Measuring sub nanometre sizes using dynamic light scattering. *J. Nanopart. Res.*, 10:823–829, 2008.

[45] V. Foder, M. Groenning, V. Vetri, F. Librizzi, S. Spagnolo, C. Cornett, L. Olsen, M. van de Weert, and M. Leone. Thioflavin T hydroxylation at basic pH and its effect on amyloid fibril detection. *J. Phys. Chem. B*, 112(47):15174–15181, 2008.

Chapter 5

Atomic Force Microscopy Studies of α-Synuclein Aggregation Leading to Amyloid Formation

5.1 Introduction

Parkinson's disease (PD) is one of the over 20 amyloidoses, which are defined by abnormal fibrillar amyloid deposits in organs or tissues of the patients.[1,2] It is the second most common neurodegenerative disease after Alzheimer's disease (AD) and 1% of the population over 60 years old are affected by it in industrial countries.[3] α-Synuclein (αSyn) is the primary protein involved in the formation of Lewy bodies found in PD, as fibrillar deposit.[4,5] The mechanism of αSyn conversion from soluble, functional state to insoluble, dysfunctional amyloid fibrils is under intensive study, aiming to provide basis for PD cure developments.[6,7]

αSyn is a small (140 residues, 14.5 kDa), intrinsically disordered protein and is mainly present in presynaptic terminals.[8,9] αSyn primary structure can be divided into three domains with distinct features.[10,11] The non-Aβ component (NAC) region includes sequence 61-95 and is highly hydrophobic. It was first identified in AD deposit as unrecognized component not related to amyloid-β (Aβ) protein.[12] This domain is resistant to proteolysis and thus believed to be incorporated in the amyloid fibril core structure. NAC is necessary for fibrillization and some short sequences in this region are sufficient to form fibrils alone.[13,14,15] The N-terminal region (1-60) contains four imperfect 11-residue repeats with consensus motif KTKEGV. All three mutations of αSyn involved in familial PD are in this region: A30P, E46K, and A53T.[16] At pH 7.55, this region has 3 net positive charges. The C-terminal (96-140) is highly acidic with 12 net negative charges at pH 7.55.[11] Overall, the αSyn primary structure can be consider as an excellent surfactant with two charged ends and a strong hydrophobic center.[17]

αSyn can form amyloid fibrils *in vitro*, which resemble those found in PD, with a typical nucleation-dependent aggregation kinetic profile.[18] However, the observed aggregation kinetics has two orders of magnitude variation in lag time from study to study. Examination of literatures reveals that αSyn amyloidogenic aggregation kinetics is very sensitive to the way of sample preparation.[18] Recorded lag time and incubation protocols are summarized in table 5.1. The αSyn aggregation kinetics *in vitro* is greatly affected by the homogeneity of αSyn sample used. While most studies use lyophilized αSyn, Apetri and coworker showed the presence of aggregates before start of the incubation in lyophilized αSyn sample.[19] Without removal of these aggregates, shorter lag time was observed, as shown in table 5.1. These pre-existing aggregates may act as seeds to accelerate the aggregation kinetics. Another important factor is whether the incubation is performed with agitation. Shorter lag time was observed for incubations with agitation. Conway and coworkers showed that no fibril was observed for several months for αSyn filtered with 100 kDa cutoff filter by quiescent incubation.[20] On the other hand, incubations with pre-existing seeds and agitation aggregated in hours.[20,21]

Agitation has been suggested to accelerate the aggregation by increasing mass transfer speed through mixing, and/or increasing number of elongation sites by promoting fibril fragmentation. In the mass transfer model, local protein concentration decreases as a result of fast fibril elongation reaction. The slow diffusion of protein to active elongation sites limit the reaction speed. Agitation can replenish protein at these sites by mixing and thus accelerate the aggregation. The fragmentation model states that fragmentation of fibril by mechanical forces during agitation can create more active sites for fibril elongation and lead to accelerated kinetics. No evidence has been shown to support either of these two mechanisms. Another factor is usually overlooked. With air and/or Teflon stir bar present, big area of hydrophobic-water interface is introduced into the incubation solution by agitation.

A systematic study was conducted to determine the primary factor for kinetic acceleration with agitation: mass transfer, fibril fragmentation or hydrophobic-water interface. To avoid the uncertainty introduced by air, namely the uncontrolled area of air-water interface, polytetrafluoroethylene (PTFE, aqueous contact angle: 108°-121°)

Lag time /hours	Conc. /uM	Buffer	Incubation	Starting material
5-30[21]	69	20 mM acetate pH 1.92-8.92	Glass vial, micro stir bar	N/A
10-70[22]	35	10 mM phosphate, pH 8.4 0-1000 mM NaCl	plate reader, agitation	Lyophilized, NaOH(pH 10) to break aggregates, centrifuge
18[23]	400	30 mM Mops, pH 7.2 0.02% NaN_3, 20uM ThT	incubator, shaking	N/A
24[24]	69	20 mM Tris-HCl, pH 7.5 100 mM NaCl	Glass Vial, micro stir bar	Lyophilized, NaOH(pH 10) to break aggregates, centrifuge
48[25]	140	20 mM Tris, pH 7.5 100 mM NaCl	Agitation,	Fresh
50[26]	83	20 mM MES, pH 6.5 100 mM NaCl	Shaking, @200 rpm	Lyophilized
80[27]	80	TBS	Roller drum, @60 rpm	Lyophilized
720[19]	300	20 mM NaPhos, pH 7.5, 0.03% NaN_3	Quiescent,	Lyophilized,100 kDa cutoff filter
>3 weeks[16]	300	10 mM NaPhos, pH 7.4, 100 mM NaCl	Quiescent	Lyophilized
Months[20]	300	10 mM NaPhos, pH 7.4, 2.7 mM KCl 137 mM NaCl	Quiescent	Lyophilized,100 kDa cutoff filter

Table 5.1: Selected publications on αSyn kinetic studies. This list shows variation in aggregation lag time with different ways of sample preparation and incubation conditions. All these experiments were on wild-type human αSyn and with incubation at 37 °C. Two factors stand out as main causes of observed kinetic variations: whether the starting material is processed to remove pre-existing aggregates and whether the incubation is performed with agitation. Both pre-existing aggregates and agitation can greatly accelerate aggregation and result in reduced lag time.

balls were used to provide hydrophobic-water interface instead. Polymethylmethacrylate (PMMA, aqueous contact angle: 73°-74°) and glass balls (aqueous contact angle: 40°-47°) were used to provide agitation with different interfaces. The αSyn amyloid aggregation kinetics were monitored with *in situ* steady-state thioflavin T (ThT) fluorescence and atomic force microscopy (AFM).

No essential aggregation was detected for both quiescent and agitated incubations with PMMA and glass balls for 300 hours. On the other hand, all the agitated incubations with PTFE balls showed substantial increase of ThT fluorescence intensity during the first 60 hours. Nucleation-dependent aggregation kinetics was observed with steady-state ThT fluorescence measurements. Fluorescence intensity plateaued within 40 hours for the 10, 20, 50 PTFE ball samples. The acceleration depended on amount of PTFE surface area, with the lag time inversely proportional to the PTFE balls used. Both the initial slope and asymptoic limit were proportional to available PTFE surface area.

These results negate mass transfer model as the primary factor for acceleration in agitated incubation. Since one PTFE ball should provide enough mixing to remove the mass transfer limitation, there should be no difference in kinetics with increased number of PTFE balls, or with PMMA and glass balls. If fibril fragmentation is the determinative factor, no difference should be observed for incubation with same number of PTFE, PMMA, and glass balls. However, with same interface area of PMMA and glass balls, no aggregation was observed in the time period during which aggregation in PTFE samples were substantial. This clearly indicated that the property of surface play an important role in αSyn amyloid aggregation. The measurement on incubations with different number of PTFE balls further supported this conclusion. With increased number of PTFE balls, greater acceleration effects were observed.

This chapter focuses on the AFM measurements made in this study. Morphologies of different species were determined by AFM imaging. Even though ThT is widely used to monitor kinetics during amyloid aggregation, the specificity and mechanism of ThT fluorescence is still unclear.[28] Aggregation other than amyloid fibrils can also induce ThT fluorescence in some cases, and thus use of ThT fluorescence alone to monitor

the amyloid aggregation process can be misleading.[29,30,31] It is necessary to take AFM measurement to check whether the aggregation actually leads to amyloid formation and to verify that the observed ThT signal reflects the amyloid aggregation progression.

5.2 Material and Methods

Removal of Pre-existing Oligomers in Lyophilized α-Synuclein

A detailed protocol for expression of αSyn can be found in Chapter 3. Four different methods were tested in attempt to remove pre-existing oligomers in freshly prepared solution of lyophilized αSyn. Native Novex Tris-Glycine gel (Invitrogen) electrophoresis was used to show effectiveness of each method. For removal by filtration, 100 kDa and 30 kDa centrifugal filter (Millipore) were used. 1mg/mL αSyn solution was prepared in 10 mM phosphate buffer (pH 7.4) with 200 mM NaCl. The filtrate from 100 kDa and 30 kDa filter were loaded directly onto the gel. The retentate was re-dissolved to make 20 times concentrated solution for 100 kDa filter and 10 times concentrated solution for the 30 kDa filter before loading. In another preparation, 6.5 mg αSyn was dissolved in 2 mL, 1 mM Na_3PO_4 solution (pH 11) for 20 minutes at room temperature. Then 0.5 M phosphate buffer (pH 6.8) was used to bring pH down and 1 mL 1.2 M NaCl was added. Millipore water was then added to adjust αSyn final concentration to 1 mg/mL. The solution was then centrifuged at 16000 rpm for 20 minutes at 10 °C and the supernatant was collected for electrophoresis. In the third preparation, 1 mg αSyn was dissolved in 100 μL Millipore water and 3 μL 0.1 N NaOH was added to bring the pH to 10.[22] After sitting at room temperature for 20 minutes, 3 μL 0.1 N HCl was added to bring the pH down. 10 mM phosphate buffer (pH 7.4) with 200 mM NaCl was added to make 1 mL solution with 1 mg/mL αSyn. The pH for is preparation was measured to be 7.2. This solution was then centrifuged at 16000 rpm for 20 minutes at 10 °C. Supernatant was collected and loaded onto the native gel.

Amyloidogenic Incubation of α-Synuclein

Grade 1, 1/16 in PTFE; 1 mm PMMA balls (Engineering Laboratories); and 1 mm glass balls (B. Braun Melsungen) were shaken in several changes of buffer to remove dust before use. Solutions were degassed with helium and an aerating frit for 3 minutes immediately before use. Protein solutions were filtered with 100 kD ultracentrifuge (Amicon Ultra, Millipore) membrane filter and diluted to a final concentration of 1 mg/mL. Purified ThT was added to make a total concentration of 8 μM. Different numbers of PTFE and PMMA balls were added to reduced volume PMMA fluorescence cuvettes (Fisher). Cuvettes were overfilled and capped with polyethylene caps (Fisher). After making sure there was no air in the cuvettes, they were sealed with hot glue. Incubation was performed in a 37 °C oven and vertically rotated at 76 rpm on a Roto-Torque heavy duty rotator in dark.[17]

Atomic Force Microscopy Sample Preparation and Imaging

After the last fluorescence measurement, sealed cuvettes were opened for AFM measurement. After inverting the cuvette several times, 20 μL incubated solution was aliquoted and deposited onto modified mica. To modify the mica surface, 30 μL of 0.1% (v/v) aminopropyltetratheoxysilane (APTES) (Acros catalog number: 151081000) was applied evenly on freshly cleaved 9.9 mm diameter muscovite mica disk (Ted Pella product number: 50) and allowed to react for 10 minutes.[32] Unreacted APTES was rinsed away with 15 mL Millipore water. The surface was dried with HPLC grade compressed nitrogen gas. Incubated sample was applied evenly on this freshly prepared surface and allowed to sit for 10 minutes. Unbound species were rinsed away with Millipore water. Residual water was blown away with nitrogen gas. The sample was imaged by a MultiMode Scanning Probe Microscope with a Nanoscope IIIa controller (Veeco), with a tapping-mode etched silicon probe (TESP, Veeco) in tapping mode in air. The scan speed was 1 Hz with an image size of 512×512 pixels. At least 3 images were obtained for each sample.

5.3 Results

5.3.1 Removal of Pre-existing Oligomers for α-Synuclein Amyloid Incubation

Pre-existing aggregates can act as seeds to accelerate αSyn amyloid aggregation. Four different methods were tested to remove these pre-existing oligomers, and the results were monitored with gel electrophoresis, as shown in Fig. 5.1. Oligomers were detected in fresh preparation made with lyophilized αSyn as shown in Fig. 5.1 column 2 and 10. Both the treatments with NaOH and basic buffer, followed by centrifugation (Fig. 5.1 column 7, 8 and 9) did not improve the homogeneity of the solution. Both monomer and oligomer band were observed, without noticeable shift of population to monomer. Filtration though 100 kDa MWCO centrifugal filter successfully removed the oligomeric species as shown by Fig. 5.1 column 3. This was confirmed by result for retentate on 100 kDa filter, as shown by Fig. 5.1 column 4, where the oligomeric species dominated the population. However, 30 kDa filter retained both monomer and oligomeric species with similar efficiency and no improvement in homogeneity was observed, as shown in Fig. 5.1 column 5 and 6. Filtration with 100 kDa filter was determined to be the only efficient method to prepare αSyn incubation without pre-existing aggregates. This method was used for all sample preparation in αSyn kinetic studies in the group.

5.3.2 Atomic Force Microscopy Measurements on Amyloid Aggregation with Agitation

All incubations agitated with PTFE balls showed increased ThT fluorescence during the first 60 hours of incubation as shown in Fig. 5.2f. Results for incubations with 1, 5, 10, 20, and 50 PTFE balls were shown in Fig. 5.2a, b, c, d, and e, respectively. For all these incubations, both fibrillar and globular particles were observed. Fibrils had the typical morphology: they were of different lengths and could be several micrometers long, with heights ranging from 3.5 nm to 9.5 nm. Some fibrils showed periodicity in height along the fibril axis, which was also commonly observed for amyloid fibrils. Some fibrils broke into small pieces when they were in full contact with the APTES modified

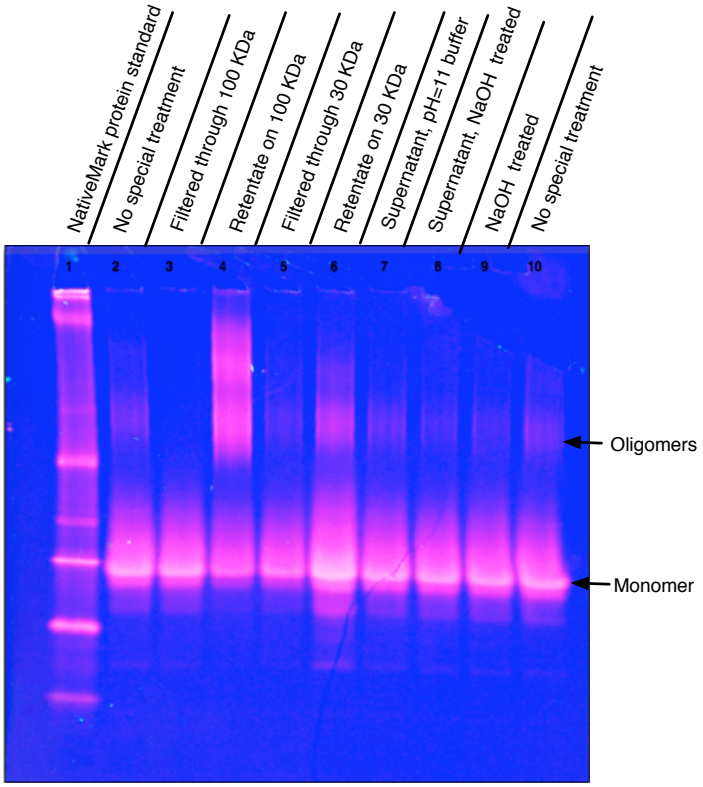

Figure 5.1: Native gel electrophoresis shows the removal of pre-existing oligomers in solution of lyophilized αSyn. Four different methods were tested with filtration or base treatment. Each column is labeled with the method used for sample preparation. Two main bands were observed in the fresh αSyn solution without any treatment. The intense lower band suggested predominant monomeric population. The band with higher molecular weight showed the pre-existing aggregates. The oligomer band disappeared completely after filtration through 100 kDa MWCO filter, while stayed after other three treatments.

mica surface. Few breakage was observed when the fibrils were sitting on top of other fibrils. With increasing density of fibrils on the surface, less breakage was observed for fibrils as in 5.2e and f. This fragmentation of fibrils on surface was likely caused by interaction between fibrils and the surface. Fibril fragmentation was seldom observed during AFM measurements for β-lactoglobulin A (β-LGA) amyloid fibrils in Chapter 2, which were obtained through quiescent incubation.[33] This suggested that the force experienced by αSyn during agitated incubation with PTFE balls made the fibrils more fragile and vulnerable to fragmentation through interaction with the surface.

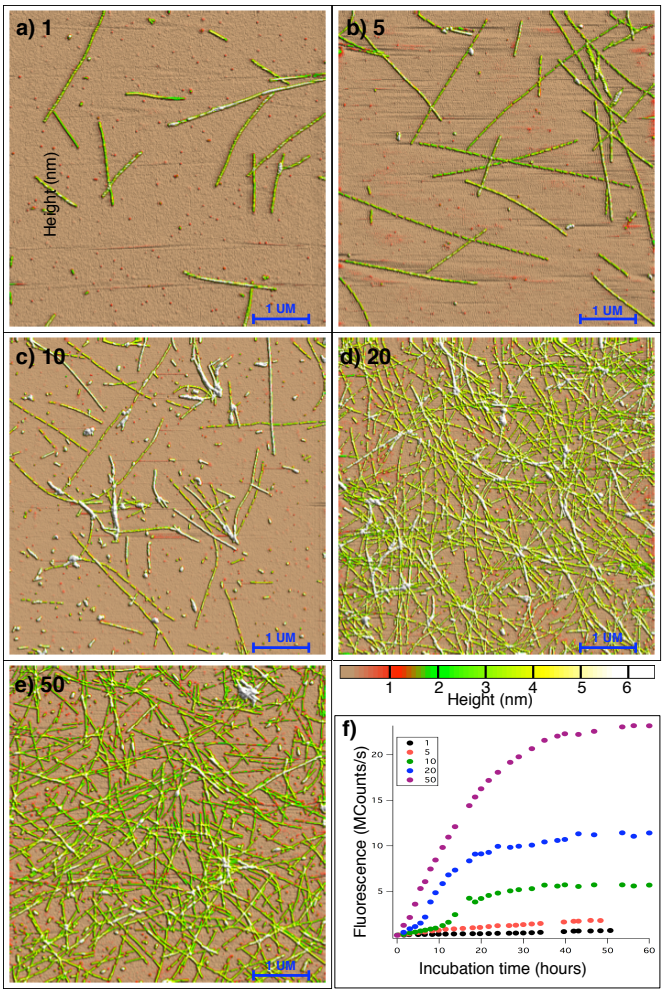

Figure 5.2: AFM images for αSyn fibrils formed by incubation with different number of PTFE balls. 1, 5, 10, 20 and 50 PTFE balls were used, as indicated in image a, b, c, and d. After the same incubation period, with more PTFE balls, increased number of fibrils were imaged on the surface. e) shows steady-state ThT fluorescence results for the same samples during first 60 hours of incubation.[17]

All the AFM data were taken after the ThT fluorescence reached the elongation phase. With more PTFE balls, the density of fibril on the surface increased from Fig. 5.2 a to f. This was consistent with the steady-state ThT fluorescence profile, as shown in Fig. 5.2 e, in which the final fluorescence intensity was proportional to the number of PTFE balls used. With more fibrils in AFM images, higher ThT fluorescence intensity was observed. The AFM measurement showed that all these conditions were actually amyloidogenic and the steady-state ThT fluorescence reflected the kinetics of

amyloid aggregation.

5.3.3 Different Aggregates Present in Incubation with Air and PTFE Balls

Most studies on αSyn aggregation agitated the sample with air present.[21,22,23,24,25,26] PTFE balls were used in this study to avoid uncontrolled area of hydrophobic/water interface created by air. Both the presence of PTFE ball and air could accelerate the aggregation kinetics. However, AFM measurements showed different morphologies for species formed under these two conditions. Fibrils were formed in both incubations, as shown in Fig. 5.3a and b. However, a great population of small globular particles showed up in the incubation with air, while only very small amount particles of similar size were observed in the incubation with PTFE balls. Moreover, larger amorphous aggregates with tens of nanometer height were found in incubation with air and were absent in incubation with PTFE balls. This observation suggested that even though both air and PTFE introduced hydrophobic-water interface into the incubation and accelerated the amyloid aggregation kinetics, different mechanisms might be involved at the PTFE-water and air-water interface.

5.4 Discussion and Future Work

Steady-state ThT fluorescence and AFM studies under different conditions revealed that hydrophobic-water interface played an important role on αSyn amyloid aggregation. αSyn aggregation kinetics was accelerated with presence of both PTFE-water and air-water interface with dependence on surface area. With hydrophobic-water interface, a heterogeneous nucleation mechanism overcome the slow homogeneous nucleation reactions. Acting as a surfactant, the partition of αSyn to hydrophobic surface was promoted, with hydrophobic NAC region interacting with the interface. How this partition actually lowered the energy barrier of the rate-determining step in amyloid aggregation is not clear. Conformational changes could be induced in protein upon binding to surface. Brezesinski and coworkers showed that Aβ was in unordered form

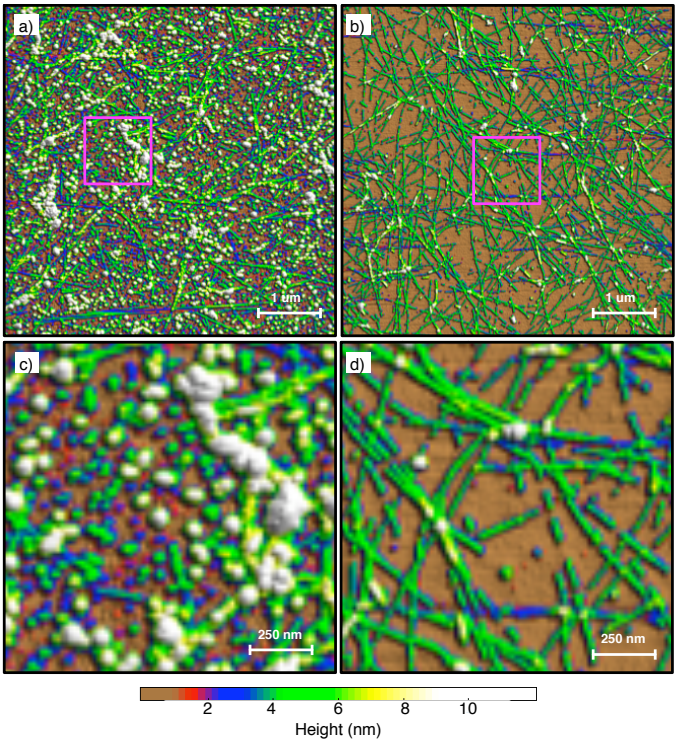

Figure 5.3: Different aggregates observed in AFM images for incubation with air/water interface and PTFE/water interface. a) and c) Aggregates formed by incubation with air. Larger amorphous aggregates were observed frequently, which were much higher than fibrils. An enlarged image of squared area in a) is shown in c). Globular particles of various heights were observed. b) and d) Aggregates formed by incubation with 20 PTFE balls. Fibrillar species dominate the population. No amorphous aggregate was observed. An enlarged image of the squared area in b) is shown in d). Few small globular particle was observed.

in solution, but adopted β-sheet structure at the air-water interface during aggregation.[34] Giacomelli and coworkers suggested that absorption of Aβ to PTFE surface promoted α-helix formation.[35] It is likely that αSyn can go through conformational change to an amyloid-prone form more readily at the interface. Increase of αSyn concentration and regular alignment of proteins on the surface can also result in accelerated fibrillization.

Behavior of αSyn at hydrophobic-water interface is the key to explain why hydrophobic interface can accelerate αSyn amyloid aggregation. Mcmillin and coworkers demonstrated a method to monitor conformational change of proteins upon binding to

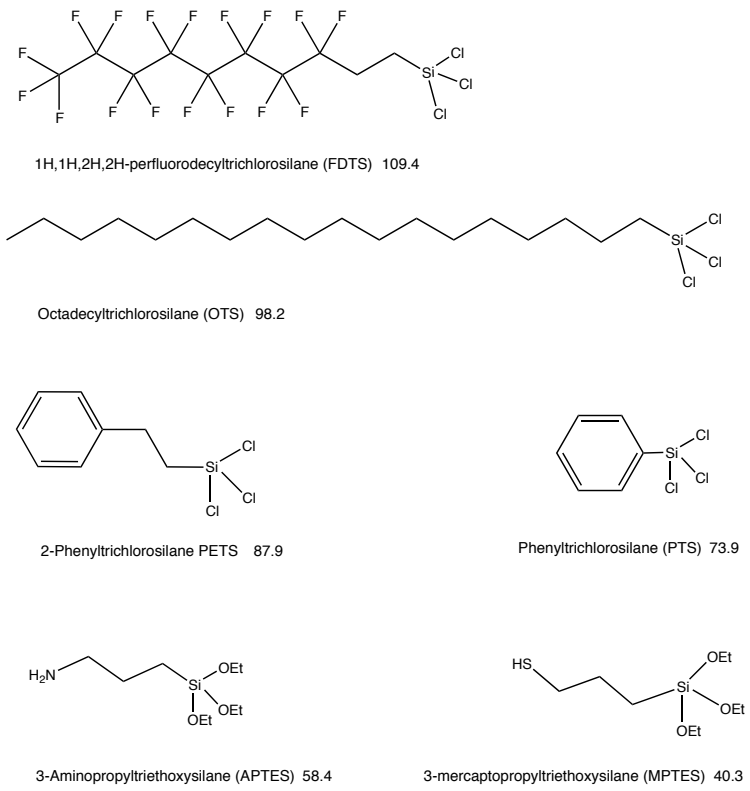

Figure 5.4: Suggested silanes for surface modification in CD measurement. The reagents are listed in the order of decreasing hydrophobicity. The strongest hydrophobic reagent FDTS has water contact angle of 109.4 °, which is close to that of PTFE. These reagents, together with hydrophilic quartz slide without modification can be used to evaluate how hydrophobicity of the surface affect αSyn secondary structure on surface.

surface, using CD measurement.[36] Shimizu and coworkers illustrated the methodology of this type of CD measurement with Cytochrome b(562) (cyt.b562). Cyt.b562 was immobilized on gold surface and the secondary structure content was measured with CD in solution and air.[37] Same idea can be used to determine αSyn secondary structure on surface. Quartz slides used in CD measurement can be modified with different silanes. With different substitutes of the silane, different hydrophobicity of the surface can be achieved. A list of silane candidates to provide a ladder of hydrophobicity is summarized in Table. 6.1.[38] The hydrophobicity is represented as water contact angle. Quartz slide without modification is hydrophilic and has contact angle of $\sim 0°$.

With different silanes, different modification protocols are needed.[38] APTES has

been used to modify glass and mica surface, used in AFM measurement on αSyn and β-LGA fibrils.[17,33] FDTS modified glass coverslip were prepared and water contact angle was measured to be $\sim$106°. Clean PTFE surface has contact angle of $\sim$108° to $\sim$121°, and the contact angle decreased with presence of ThT and protein during the incubation.[17] αSyn should undergo similar conformational changes on the FDTS modified surface as on the PTFE balls. The protocol used to prepared FDTS modified glass surface can be summarized as following: slides were first treated with Piranha (H_2SO_4:H_2O_2, v/v 3:1) solution at 90 °C for 30 minutes, then thoroughly rinsed with Millipore water and dried with high purity compress nitrogen gas. The slides were cleaned and hydroxylated after this treatment. The modification was carried out in a glove box filled with nitrogen. Slides were put in a petri disk with a drop of FDTS applied onto the same petri disk but away from the slides. The petri disk was covered and heated to 90 °C on a hot plate for 3 hours. After the hot plate cooled down to room temperature, the slides were washed with anhydrous hexane.[39]

Bibliography

[1] M. B. Pepys. Amyloidosis. *Annu. Rev. Med.*, 57:223–241, 2006.

[2] F. Chiti and C. M. Dobson. Protein misfolding, functional amyloid, and human disease. *Annu. Rev. Biochem.*, 75:333–366, 2006.

[3] L. M. L. de Lau and M. M. B. Breteler. Epidemiology of Parkinson's disease. *Lancet Neurol.*, 5:525–535, 2006.

[4] K. Arima, K. Ueda, N. Sunohara, S. Hirai, Y. Izumiyama, H. Tonozuka-Uehara, and M. Kawai. Immunoelectron-microscopic demonstration of NACP/α-synuclein-epitopes on the filamentous component of Lewy bodies in Parkinson's disease and in dementia with Lewy bodies. *Brain Research*, 808(1):93–100, 1998.

[5] M. G. Spillantini, R. A. Crowther, R. Jakes, M. Hasegawa, and M. Goedert. α-Synuclein in filamentous inclusions of Lewy bodies from Parkinson's disease and dementia with lewy bodies. *Proc. Natl. Acad. Sci. U. S. A.*, 95(11):6469–6473, 1998.

[6] W. Dauer and S. Przedborski. Parkinson's disease: mechanisms and models. *Neuron*, 39(6):889–909, 2003.

[7] A. L. Fink. The aggregation and fibrillation of α-synuclein. *Acc. Chem. Res.*, 39(9):628–634, 2006.

[8] D. Eliezer, E. Kutluay, R. Bussell, and G. Browne. Conformational properties of α-synuclein in its free and lipid-associated states. *J. Mol. Biol.*, 307(4):1061–1073, 2001.

[9] V. N. Uversky, C. J. Oldfield, and A. K. Dunker. Intrinsically disordered proteins

in human diseases: introducing the D2 concept. *Annu. Rev. Biophys.*, 37:215–246, 2008.

[10] T. S. Ulmer, A. Bax, N. B. Cole, and R. L. Nussbaum. Structure and dynamics of micelle-bound human α-synuclein. *J. Biol. Chem.*, 280(10):9595–9603, 2005.

[11] M. Bisaglia, S. Mammi, and L. Bubacco. Structural insights on physiological functions and pathological effects of α-synuclein. *FASEB J.*, 23(2):329–340, 2009.

[12] K. Ueda, H. Fukushima, E. Masliah, Y. Xia, A. Iwai, M. Yoshimoto, D. A. Otero, J. Kondo, Y. Ihara, and T. Saitoh. Molecular cloning of cDNA encoding an unrecognized component of amyloid in Alzheimer disease. *Proc. Natl. Acad. Sci. U. S. A.*, 90(23):11282–11286, 1993.

[13] A. Iwai, M. Yoshimoto, E. Masliah, and T. Saitoh. Non-Aβ component of Alzheimer's disease amyloid (NAC) is amyloidogenic. *Biochemistry*, 34(32):10139–10145, 1995.

[14] B. I. Giasson, I. V. Murray, J. Q. Trojanowski, and V. M. Lee. A hydrophobic stretch of 12 amino acid residues in the middle of α-synuclein is essential for filament assembly. *J. Biol. Chem.*, 276(4):2380–2386, 2001.

[15] A. M. Bodles, D. J. Guthrie, B. Greer, and G. B. Irvine. Identification of the region of non-Aβ component (NAC) of Alzheimer's disease amyloid responsible for its aggregation and toxicity. *J. Neurochem.*, 78(2):384–395, 2001.

[16] K. A. Conway, J. D. Harper, and P. T. Lansbury. Accelerated in vitro fibril formation by a mutant α-synuclein linked to early-onset Parkinson disease. *Nat. Med.*, 4(11):1318–1320, 1998.

[17] J. Pronchik, X. He, J. T. Giurleo, and D. S. Talaga. In vitro formation of amyloid from α-synuclein is dominated by reactions at hydrophobic interfaces. *J. Am. Chem. Soc.*, 132:9797–9803, 2010.

[18] A. L. Fink. Factors affecting the fibrilliztion of α-synuclein, a natively unfolded protein. *Misbehaving Proteins*, 2006.

[19] M. M. Apetri, N. C. Maiti, M. G. Zagorski, P. R. Carey, and V. E. Anderson. Secondary structure of α-synuclein oligomers: characterization by raman and atomic force microscopy. *J. Mol. Biol.*, 355(1):63–71, 2006.

[20] K. A. Conway, S. J. Lee, J. C. Rochet, T. T. Ding, R. E. Williamson, and P. T. Lansbury. Acceleration of oligomerization, not fibrillization, is a shared property of both α-synuclein mutations linked to early-onset Parkinson's disease: implications for pathogenesis and therapy. *Proc. Natl. Acad. Sci. U. S. A.*, 97(2):571–576, 2000.

[21] J. Kaylor, N. Bodner, S. Edridge, G. Yamin, D. Hong, and A. L. Fink. Characterization of oligomeric intermediates in α-synuclein fibrillation: FRET studies of Y125W/Y133F/Y136F α-synuclein. *J. Mol. Biol.*, 353(2):357–372, 2005.

[22] L. A. Munishkina, J. Henriques, V. N. Uversky, and A. L. Fink. Role of protein-water interactions and electrostatics in α-synuclein fibril formation. *Biochemistry*, 43(11):3289–3300, 2004.

[23] S. Zibaee, R. Jakes, G. Fraser, L. C. Serpell, R. A. Crowther, and M. Goedert. Sequence determinants for amyloid fibrillogenesis of human α-synuclein. *J. Mol. Biol.*, 374(2):454–464, 2007.

[24] R. Khurana, C. Ionescu-Zanetti, M. Pope, J. Li, L. Nielson, M. Ramrez-Alvarado, L. Regan, A. L. Fink, and S. A. Carter. A general model for amyloid fibril assembly based on morphological studies using atomic force microscopy. *Biophy.J.*, 85(2):1135–1144, 2003.

[25] K. Ono, M. Hirohata, and M. Yamada. Anti-fibrillogenic and fibril-destabilizing activities of anti-Parkinsonian agents for α-synuclein fibrils in vitro. *J. Neurosci. Res.*, 85(7):1547–1557, 2007.

[26] J. S. Ahn, J. Lee, J. Kim, and S. R. Paik. Novel method for quantitative determination of amyloid fibrils of α-synuclein and amyloid β/A4 protein by using resveratrol. *Anal. Biochem.*, 367(2):259–265, 2007.

[27] J. C. Kessler, J. Rochet, and P. T. Lansbury. The N-terminal repeat domain of α-synuclein inhibits β-sheet and amyloid fibril formation. *Biochemistry*, 42(3):672–678, 2003.

[28] M. Groenning. Binding mode of Thioflavin T and other molecular probes in the context of amyloid fibrils-current status. *J. Chem. Biol.*, 3(1):1–18, 2009.

[29] J. T. Giurleo, X. He, and D. S. Talaga. β-lactoglobulin assembles into amyloid through sequential aggregated intermediates. *J. Mol.. Biol.*, 381(5):1332–1348, 2008.

[30] M. Harel, L. K. Sonoda, I. Silman, J. L. Sussman, and T. L. Rosenberry. Crystal structure of thioflavin T bound to the peripheral site of Torpedo californica acetylcholinesterase reveals how thioflavin T acts as a sensitive fluorescent reporter of ligand binding to the acylation site. *J. Am. Chem. Soc.*, 130(25):7856–7861, 2008.

[31] L. S. Wolfe, M. F. Calabrese, A. Nath, D. V. Blaho, A. D. Miranker, and Y. Xiong. Protein-induced photophysical changes to the amyloid indicator dye thioflavin T. *Proc. Natl. Acad. Sci. U. S. A.*, 107(39):16863–16868, 2010.

[32] Z. Liu, Z. Li, H. Zhou, G. Wei, Y. Song, and L. Wang. Immobilization and condensation of DNA with 3-aminopropyltriethoxysilane studied by atomic force microscopy. *J. Microsc.*, 218(Pt 3):233–239, 2005.

[33] X. He, J. T. Giurleo, and D. S. Talaga. Role of small oligomers on the amyloidogenic aggregation free-energy landscape. *J. Mol. Biol.*, 395:134–154, 2010.

[34] G. Brezesinski, E. Maltseva, and H. Moehwald. Adsorption of amyloid β(1-40) peptide at liquid interfaces. *Z. Phys. Chem*, 221:95–111, 2007.

[35] C. E. Giacomelli and W. Norde. Influence of hydrophobic Teflon particles on the structure of amyloid β-peptide. *Biomacromolecules*, 4(6):1719–1726, 2003.

[36] C. R. Mcmillin and A. G. Walton. A circular dichroism technique for the study of adsorbed protein structure. *J. Colloid Interface Sci.*, 48(2):345–349, 1974.

[37] M. Shimizu, K. Kobayashi, H. Morii, K. Mitsui, W. Knoll, and T. Nagamune. Secondary structure analyses of protein films on gold surfaces by circular dichroism. *Biochem. Biophys. Res. Commun.*, 310(2):606–611, 2003.

[38] D. Janssen, R. De Palma, S. Verlaak, P. Heremans, and W. Dehaen. Static solvent contact angle measurements, surface free energy and wettability determination of various self-assembled monolayers on silicon dioxide. *Thin Solid Films*, 515:1433–1438, 2006.

[39] W. Zhou, J. Zhang, Y. Liu, X. Li, X. Niu, Z. Song, G. Min, Y. Wan, L. Shi, and S. Feng. Characterization of anti-adhesive self-assembled monolayer for nanoimprint lithography. *Appl. Surf. Sci.*, 255:2885–2889, 2008.

Chapter 6

Appendix

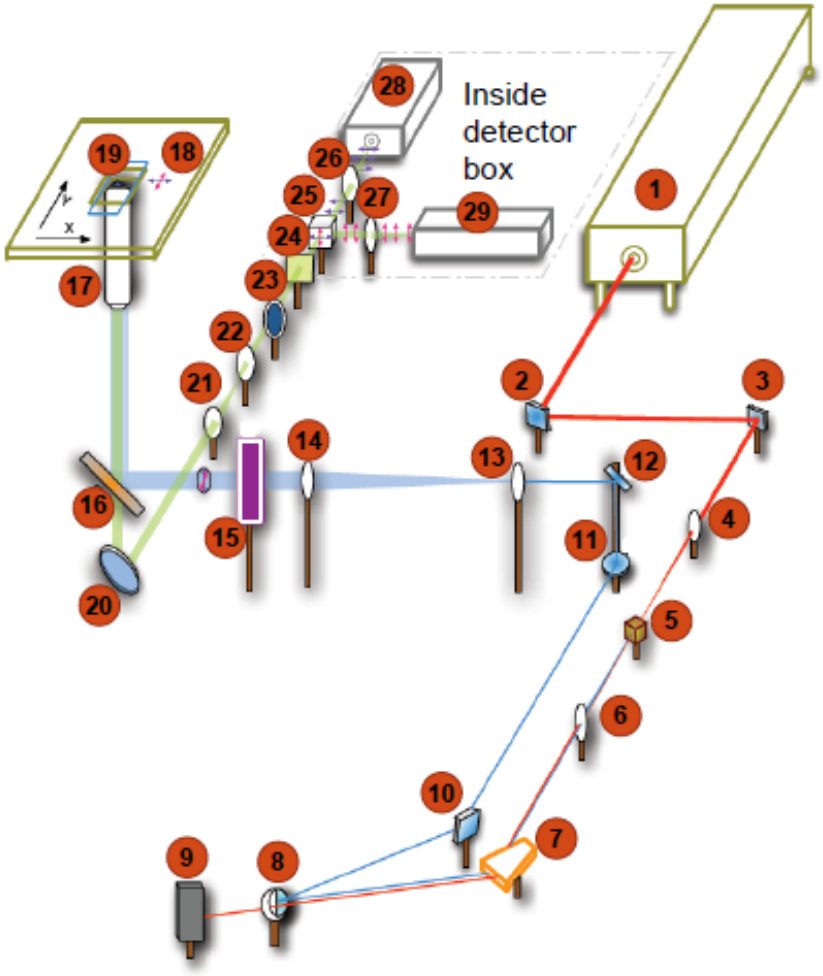

Figure 6.1: Single-molecule fluorescence microscopy instrumentation.

List of components in single-molecule fluorescence microscopy:

1) 80.00000 MHz Mode-locked Ti-Sapphire laser

2), 3) Mirror

4) Lens to laser beam into doubling crystal

5) Frequency doubling crystal

6) Lens to collimate laser beam

7) Prolin-Broca prism to separate doubled beam and fundamental beam

8) Half-mirror: used to reflect doubled beam

9) Photodiode for Sync signal in TCSPC measurement

10), 11), 12) Mirror used to direct beam into microscope

13), 14) Lens to expand and collimate excitation beam

15) Quarter-wave plate convert linear polarized light to circularly polarized light

16) Dichroic mirror

17) Objective

18) Nanopositioning stage

19) Coverslip

20) Mirror to direct emission light to detection channel

21), 22) lens to focus and collimate emission light

23) Notch filter to block excitation light

24) High-pass filter

25) Polarizer cube to separate emission into horizontal and vertical components

26), 27) Lens to focus emission light onto detectors

28), 29) Detectors

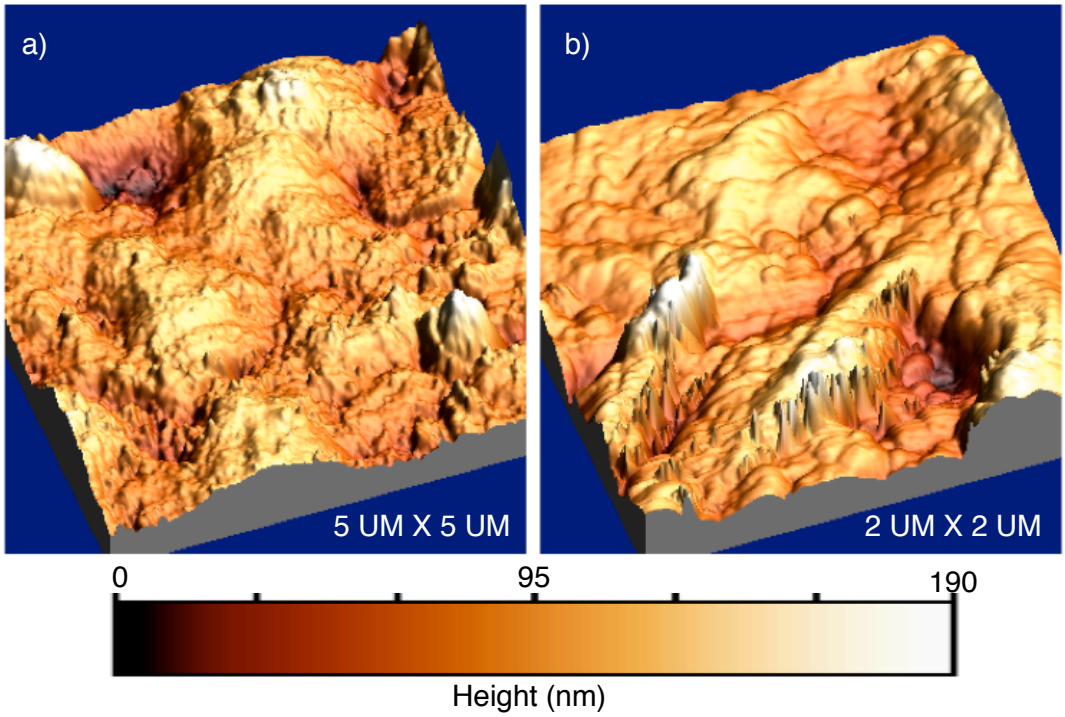

Figure 6.2: AFM images of a) PTFE and b) PMMA ball surface. PTFE balls were used to provide hydrophobic-water interface in α-Synuclein amyloid incubation. With smaller aqueous contact angle, PMMA balls provided different interface for control experiment. The area of interface was controlled by number of balls during the experiment. The roughness of the balls could result in larger surface area for protein interaction. AFM images showed comparable roughness for the two types of balls used.

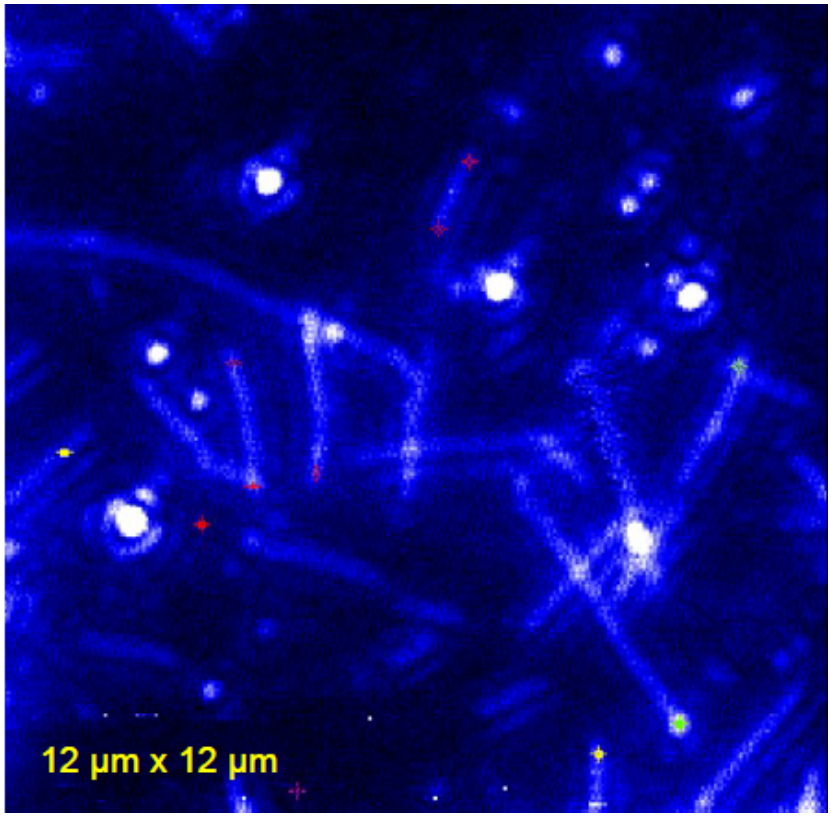

Figure 6.3: Single-molecule fluorescence microscopy intensity image for ThT-stained α-Synuclein amyloid fibrils dried on coverslip. Except this image, all other single-molecule fluorescence images presented in this dissertation were taken using a house-designed sample chamber, which kept the sample from drying out on the coverslip during the measurement. This image here was taken by letting the sample slowly dry out on the coverslip. Bright globular particles were observed in this image but absent in all other images taken under wet condition. These bright spots could be nanoparticles formed by ThT on the surface during drying.

Below are the sample Mathematica codes used to perform kinetic simulations for β-LGA amyloid formation in Chapter 2. The first function *SimuDLS* in Eq. 6.1 was used to plot the simulated DLS data for reservoir-nucleation model, based on the kinetic scheme below. *max* is the aggregation number of the largest aggregates included in the simulation, which equals to 252 according to the scheme below.

$$A_1 + A_1 \underset{kra_2}{\overset{kfa_1}{\rightleftharpoons}} A_2$$

$$A_2 \underset{kr_{oa}}{\overset{kf_{oa}}{\rightleftharpoons}} A_2^{\mathrm{Ox}}$$

$$A_2 + A_2^{\mathrm{Ox}} \underset{kra_4}{\overset{kfa_2}{\rightleftharpoons}} A_4$$

$$A_4 \underset{kr_{ab}}{\overset{kf_{ab}}{\rightleftharpoons}} B_4$$

$$B_4 + A_4 \underset{krb_8}{\overset{kfb_4}{\rightleftharpoons}} B_8$$

$$B_8 + A_4 \underset{krb_{12}}{\overset{kfb_8}{\rightleftharpoons}} B_{12}$$

$$\vdots$$

$$B_{76} + A_4 \underset{krb_{80}}{\overset{kfb_{76}}{\rightleftharpoons}} B_{80}$$

$$B_{16} \underset{kr_f}{\overset{kf_f}{\rightleftharpoons}} F_{16}$$

$$F_{16} + A_4 \underset{kr_{fg}}{\overset{kffg_{16}}{\rightleftharpoons}} F_{20}$$

$$F_{20} + A_4 \underset{kr_{fg}}{\overset{kffg_{20}}{\rightleftharpoons}} F_{24}$$

$$\vdots$$

$$F_{248} + A_4 \underset{kr_{fg}}{\overset{kffg_{248}}{\rightleftharpoons}} F_{252}$$

SAMPLE SCHEME FOR RESERVOIR NUCLEATION MODEL

SimuDLS [$\text{kfa}_{1\_}, \text{kra}_{2\_}, \text{kf}_{oa\_}, \text{kr}_{oa\_}, \text{kfa}_{2\_}, \text{kra}_{4\_}, \text{kf}_{ab\_}, \text{kr}_{ab\_}, \text{kfb}_{list\_}, \text{krb}_{list\_}, \text{kf}_{f\_}, \text{kr}_{f\_}$,

$\text{kffg}_{list\_}, \text{kr}_f g_{\_}, \text{max}_{\_}]:=$

Module[{soln}, Table[$\text{kfb}_i = \text{kfb}_{list}[[i/4]]$, $\{i, 4, 76, 4\}$]; Table[$\text{krb}_i = \text{krb}_{list}[[i/4 - 1]]$,

$\{i, 8, 80, 4\}$]; Table [$\text{kffg}_i = \text{kffg}_{list}[[i/4 - 3]]$, $\{i, 16, \text{max}, 4\}$] ;

soln = NDSolve[Flatten[$\{a_1'[t] == -2\ \text{kfa}_1\ a_1[t]^2 + 2\ \text{kra}_2\ a_2[t]$,

$a_2'[t] == \text{kfa}_1\ a_1[t]^2 - \text{kra}_2\ a_2[t] - \text{kf}_{oa}\ a_2[t] - \text{kfa}_2\ a_2[t]\ \text{oa}_2[t] + \text{kra}_4\ a_4[t] + \text{kr}_{oa}\ \text{oa}_2[t]$,

$\text{oa}_2'[t] == \text{kf}_{oa}\ a_2[t] - \text{kfa}_2\ a_2[t]\ \text{oa}_2[t] + \text{kra}_4\ a_4[t] - \text{kr}_{oa}\ \text{oa}_2[t]$,

$a_4'[t] == \text{kfa}_2\ a_2[t]\ \text{oa}_2[t] - \text{kra}_4\ a_4[t] - \text{kf}_{ab}\ a_4[t] + \text{kr}_{ab}\ b_4[t] - \text{Sum}[\text{kffg}_i\ f_i[t]\ a_4[t]$,

$\{i, 16, \text{max} - 4, 4\}] + \text{Sum}[\text{kr}_f g\ f_i[t], \{i, 20, \text{max}, 4\}] - \text{Sum}[\text{kfb}_i\ b_i[t]\ a_4[t], \{i, 4, 76, 4\}]$

$+ \text{Sum}[\text{krb}_i\ b_i[t], \{i, 8, 80, 4\}], b_4'[t] == \text{kf}_{ab}\ a_4[t] - \text{kr}_{ab}\ b_4[t] - \text{kfb}_4\ b_4[t]\ a_4[t] + \text{krb}_8\ b_8[t]$,

$b_8'[t] == \text{kfb}_4\ b_4[t]\ a_4[t] - \text{krb}_8\ b_8[t] - \text{kfb}_8\ b_8[t]\ a_4[t] + \text{krb}_{12}\ b_{12}[t]$,

$b_{12}'[t] == \text{kfb}_8\ b_8[t]\ a_4[t] - \text{krb}_{12}\ b_{12}[t] - \text{kfb}_{12}\ b_{12}[t]\ a_4[t] + \text{krb}_{16}\ b_{16}[t]$,

$b_{16}'[t] == \text{kfb}_{12}\ b_{12}[t]\ a_4[t] - \text{krb}_{16}\ b_{16}[t] - \text{kfb}_{16}\ b_{16}[t]\ a_4[t] + \text{krb}_{20}\ b_{20}[t] - \text{kf}_f\ b_{16}[t] + \text{kr}_f\ f_{16}[t]$,

Table[$b_i'[t] == \text{kfb}_{i-4}\ b_{i-4}[t]\ a_4[t] - \text{krb}_i\ b_i[t] - \text{kfb}_i\ b_i[t]\ a_4[t] + \text{krb}_{i+4}\ b_{i+4}[t], \{i, 20, 76, 4\}$],

$b_{80}'[t] == \text{kfb}_{76}\ b_{76}[t]\ a_4[t] - \text{krb}_{80}\ b_{80}[t]$,

$f_{16}'[t] == \text{kf}_f\ b_{16}[t] - \text{kr}_f\ f_{16}[t] - \text{kffg}_{16}\ f_{16}[t]\ a_4[t] + \text{kr}_f g\ f_{20}[t]$,

Table[$f_i'[t] == \text{kffg}_{i-4}\ f_{i-4}[t]\ a_4[t] - \text{kr}_f g\ f_i[t] - \text{kffg}_i\ f_i[t]\ a_4[t] + \text{kr}_f g\ f_{i+4}[t]$,

$\{i, 20, \text{max} - 4, 4\}], f_{\text{max}}'[t] == \text{kffg}_{\text{max}-4}\ f_{\text{max}-4}[t]\ a_4[t] - \text{kr}_f g\ f_{\text{max}}[t]$,

Table[$b_i[0] == 0, \{i, 4, 80, 4\}], a_1[0] == 53, a_2[0] == 0, a_4[0] == 0, \text{oa}_2[0] == 0$,

Table[$f_i[0] == 0, \{i, 16, \text{max}, 4\}]\}], \text{Flatten}[\{a_1, a_2, \text{oa}_2, a_4, \text{Table}[b_i, \{i, 4, 80, 4\}]$,

Table[$f_i, \{i, 16, \text{max}, 4\}]\}], \{t, 0, 100\}$];

FitFunction = Evaluate[$\text{Sum}[i^2\ a_i[t]\ e^{-\frac{1}{2}(\frac{\tau - 0.02 * i^{1/3}}{0.004})^2}, \{i, \{1, 2, 4\}\}]$

$+ \text{Sum}[i^2\ b_i[t]\ e^{-\frac{1}{2}(\frac{\tau - 0.02 * i^{1/3}}{0.004})^2}, \{i, 4, 80, 4\}] + 4\ \text{oa}_2[t]\ e^{-\frac{1}{2}(\frac{\tau - 0.02 * 2^{1/3}}{0.004})^2}$/.soln];

FitMatrix = Table[First[FitFunction], $\{t, 0, 28, 2\}, \{\tau, \text{Table}[10\text{^}\tau, \{\tau, -2, -1, 0.05\}]\}$];

$$\text{ListPlot3D[Table[(FitMatrix[[}i\text{]]} + 10^{-18})/(\text{Max[FitMatrix[[}i\text{]]]} + 10^{-18}), \{i, 1, 15\}],$$
$$\text{ColorFunction} \to \text{DarkRainbow}, \text{DataRange} \to \{\{\text{Log}[10, 0.01], \text{Log}[10, 0.1]\},$$
$$\{0, 28\}, \text{Automatic}\}]] \tag{6.1}$$

Function $ReservoirPoP$, Eq. 6.2, was used to plot the population evolution of monomers incorporated into protofibrils based on reservoir-nucleation model. The population of protofibrils on time point, $SeedDay$, was obtained and used as input $Seed$ in function $ReservoirPoP$. The $ReservoirPoPSeed$, Eq. 6.3, was used to plot the seeded kinetic profile for reservoir-nucleation model.

$$\text{ReservoirPoP } [\text{kfa}_{1\_}, \text{kra}_{2\_}, \text{kf}_{oa\_}, \text{kr}_{oa\_}, \text{kfa}_{2\_}, \text{kra}_{4\_}, \text{kf}_{ab\_}, \text{kr}_{ab\_}, \text{kfb}_{list\_}, \text{krb}_{list\_}, \text{kf}_{f\_},$$
$$\text{kr}_{f\_}, \text{kffg}_{list\_}, \text{kr}_{fg\_}, \text{max}_{\_}, \text{SeedDay}_{\_}]:=$$
$$\text{Module}[\{\text{soln}\}, \text{Table}[\text{kfb}_i = \text{kfb}_{list}[[i/4]], \{i, 4, 76, 4\}]; \text{Table}[\text{krb}_i = \text{krb}_{list}[[i/4 - 1]],$$
$$\{i, 8, 80, 4\}]; \text{Table}\,[\text{kffg}_i = \text{kffg}_{list}[[i/4 - 3]], \{i, 16, \text{max}, 4\}]\,;$$
$$\text{soln} = \text{NDSolve}[\text{Flatten}[\{a_1'[t] == -2\ \text{kfa}_1\ a_1[t]^2 + 2\ \text{kra}_2\ a_2[t],$$
$$a_2'[t] == \text{kfa}_1\ a_1[t]^2 - \text{kra}_2\ a_2[t] - \text{kf}_{oa}\ a_2[t] - \text{kfa}_2\ a_2[t]\ \text{oa}_2[t] + \text{kra}_4\ a_4[t] + \text{kr}_{oa}\ \text{oa}_2[t],$$
$$\text{oa}_2'[t] == \text{kf}_{oa}\ a_2[t] - \text{kfa}_2\ a_2[t]\ \text{oa}_2[t] + \text{kra}_4\ a_4[t] - \text{kr}_{oa}\ \text{oa}_2[t],$$
$$a_4'[t] == \text{kfa}_2\ a_2[t]\ \text{oa}_2[t] - \text{kra}_4\ a_4[t] - \text{kf}_{ab}\ a_4[t] + \text{kr}_{ab}\ b_4[t] - \text{Sum}[\text{kffg}_i\ f_i[t]\ a_4[t],$$
$$\{i, 16, \text{max} - 4, 4\}] + \text{Sum}[\text{kr}_f g\ f_i[t], \{i, 20, \text{max}, 4\}] - \text{Sum}[\text{kfb}_i\ b_i[t]\ a_4[t], \{i, 4, 76, 4\}]$$
$$+ \text{Sum}[\text{krb}_i\ b_i[t], \{i, 8, 80, 4\}], b_4'[t] == \text{kf}_{ab}\ a_4[t] - \text{kr}_{ab}\ b_4[t] - \text{kfb}_4\ b_4[t]\ a_4[t] + \text{krb}_8\ b_8[t],$$
$$b_8'[t] == \text{kfb}_4\ b_4[t]\ a_4[t] - \text{krb}_8\ b_8[t] - \text{kfb}_8\ b_8[t]\ a_4[t] + \text{krb}_{12}\ b_{12}[t],$$
$$b_{12}'[t] == \text{kfb}_8\ b_8[t]\ a_4[t] - \text{krb}_{12}\ b_{12}[t] - \text{kfb}_{12}\ b_{12}[t]\ a_4[t] + \text{krb}_{16}\ b_{16}[t],$$
$$b_{16}'[t] == \text{kfb}_{12}\ b_{12}[t]\ a_4[t] - \text{krb}_{16}\ b_{16}[t] - \text{kfb}_{16}\ b_{16}[t]\ a_4[t] + \text{krb}_{20}\ b_{20}[t]$$
$$- \text{kf}_f\ b_{16}[t] + \text{kr}_f\ f_{16}[t], \text{Table}[b_i'[t] == \text{kfb}_{i-4}\ b_{i-4}[t]\ a_4[t] - \text{krb}_i\ b_i[t] - \text{kfb}_i\ b_i[t]\ a_4[t]$$
$$+ \text{krb}_{i+4}\ b_{i+4}[t], \{i, 20, 76, 4\}], b_{80}'[t] == \text{kfb}_{76}\ b_{76}[t]\ a_4[t] - \text{krb}_{80}\ b_{80}[t],$$

$$
\begin{aligned}
&f'_{16}[t] == \mathrm{kf}_f\ b_{16}[t] - \mathrm{kr}_f\ f_{16}[t] - \mathrm{kffg}_{16}\ f_{16}[t]a_4[t] + \mathrm{kr}_f g\ f_{20}[t], \mathrm{Table}[f'_i[t] == \\
&\mathrm{kffg}_{i-4}\ f_{i-4}[t]\ a_4[t] - \mathrm{kr}_f g\ f_i[t] - \mathrm{kffg}_i\ f_i[t]\ a_4[t] + \mathrm{kr}_f g\ f_{i+4}[t], \{i, 20, \max -4, 4\}], \\
&f'_{\max}[t] == \mathrm{kffg}_{\max -4}\ f_{\max -4}[t]\ a_4[t] - \mathrm{kr}_f g\ f_{\max}[t], \\
&\mathrm{Table}[b_i[0] == 0, \{i, 4, 80, 4\}], a_1[0] == 53, a_2[0] == 0, a_4[0] == 0, \mathrm{oa}_2[0] == 0, \\
&\mathrm{Table}[f_i[0] == 0, \{i, 16, \max, 4\}]\}], \mathrm{Flatten}[\{a_1, a_2, \mathrm{oa}_2, a_4, \mathrm{Table}[b_i, \{i, 4, 80, 4\}], \\
&\mathrm{Table}[f_i, \{i, 16, \max, 4\}]\}], \{t, 0, 100\}]; \\
&\mathrm{SeedPop} = \mathrm{Flatten}[\mathrm{Evaluate}[\mathrm{Table}[f_i\ [\mathrm{SeedDay}], \{i, 16, \max, 4\}]/.\mathrm{soln}]]; \\
&\mathrm{Plot}[\mathrm{Evaluate}[\mathrm{Sum}[i\ f_i[t], \{i, 16, \max, 4\}]/.\mathrm{soln}], \{t, 0, 100\}, \\
&\mathrm{PlotRange} \to \{0, \mathrm{All}\}]]
\end{aligned}
\tag{6.2}
$$

$$
\begin{aligned}
&\mathrm{ReservoirPopSeed}\ [\mathrm{kfa}_{1\_}, \mathrm{kra}_{2\_}, \mathrm{kf}_{oa\_}, \mathrm{kr}_{oa\_}, \mathrm{kfa}_{2\_}, \mathrm{kra}_{4\_}, \mathrm{kf}_{ab\_}, \mathrm{kr}_{ab\_}, \mathrm{kfb}_{list\_}, \mathrm{krb}_{list\_}, \\
&\qquad \mathrm{kf}_{f\_}, \mathrm{kr}_{f\_}, \mathrm{kffg}_{list\_}, \mathrm{kr}_f g_{\_}, \max_{\_}, \mathrm{Seed}_{\_}]:= \\
&\mathrm{Module}[\{\mathrm{soln}\}, \mathrm{Table}[\mathrm{kfb}_i = \mathrm{kfb}_{list}[[i/4]], \{i, 4, 76, 4\}]; \\
&\mathrm{Table}[\mathrm{krb}_i = \mathrm{krb}_{list}[[i/4 - 1]], \{i, 8, 80, 4\}]; \\
&\mathrm{Table}\,[\mathrm{kffg}_i = \mathrm{kffg}_{list}[[i/4 - 3]], \{i, 16, \max, 4\}]\,; \\
&\mathrm{soln} = \mathrm{NDSolve}[\mathrm{Flatten}[\{a'_1[t] == -2\ \mathrm{kfa}_1\ a_1[t]^2 + 2\ \mathrm{kra}_2\ a_2[t], \\
&a'_2[t] == \mathrm{kfa}_1\ a_1[t]^2 - \mathrm{kra}_2\ a_2[t] - \mathrm{kf}_{oa}\ a_2[t] - \mathrm{kfa}_2\ a_2[t]\ \mathrm{oa}_2[t] + \mathrm{kra}_4\ a_4[t] \\
&+ \mathrm{kr}_{oa}\ \mathrm{oa}_2[t], \mathrm{oa}'_2[t] == \mathrm{kf}_{oa}\ a_2[t] - \mathrm{kfa}_2\ a_2[t]\ \mathrm{oa}_2[t] + \mathrm{kra}_4\ a_4[t] - \mathrm{kr}_{oa}\ \mathrm{oa}_2[t], \\
&a'_4[t] == \mathrm{kfa}_2\ a_2[t]\ \mathrm{oa}_2[t] - \mathrm{kra}_4\ a_4[t] - \mathrm{kf}_{ab}\ a_4[t] + \mathrm{kr}_{ab}\ b_4[t] \\
&- \mathrm{Sum}[\mathrm{kffg}_i\ f_i[t]\ a_4[t], \{i, 16, \max -4, 4\}] + \mathrm{Sum}[\mathrm{kr}_f g\ f_i[t], \{i, 20, \max, 4\}] \\
&- \mathrm{Sum}[\mathrm{kfb}_i\ b_i[t]\ a_4[t], \{i, 4, 76, 4\}] + \mathrm{Sum}[\mathrm{krb}_i\ b_i[t], \{i, 8, 80, 4\}], \\
&b'_4[t] == \mathrm{kf}_{ab}\ a_4[t] - \mathrm{kr}_{ab}\ b_4[t] - \mathrm{kfb}_4\ b_4[t]\ a_4[t] + \mathrm{krb}_8\ b_8[t], \\
&b'_8[t] == \mathrm{kfb}_4\ b_4[t]\ a_4[t] - \mathrm{krb}_8\ b_8[t] - \mathrm{kfb}_8\ b_8[t]\ a_4[t] + \mathrm{krb}_{12}\ b_{12}[t], \\
&b'_{12}[t] == \mathrm{kfb}_8\ b_8[t]\ a_4[t] - \mathrm{krb}_{12}\ b_{12}[t] - \mathrm{kfb}_{12}\ b_{12}[t]\ a_4[t] + \mathrm{krb}_{16}\ b_{16}[t], \\
&b'_{16}[t] == \mathrm{kfb}_{12}\ b_{12}[t]\ a_4[t] - \mathrm{krb}_{16}\ b_{16}[t] - \mathrm{kfb}_{16}\ b_{16}[t]\ a_4[t] + \mathrm{krb}_{20}\ b_{20}[t]
\end{aligned}
$$

$$
\begin{aligned}
&-\mathrm{kf}_f\ b_{16}[t] + \mathrm{kr}_f\ f_{16}[t], \mathrm{Table}[b_i'[t] == \mathrm{kfb}_{i-4}\ b_{i-4}[t]\ a_4[t] - \mathrm{krb}_i\ b_i[t] - \mathrm{kfb}_i\ b_i[t]\ a_4[t] \\
&+ \mathrm{krb}_{i+4}\ b_{i+4}[t], \{i, 20, 76, 4\}], b_{80}'[t] == \mathrm{kfb}_{76}\ b_{76}[t]\ a_4[t] - \mathrm{krb}_{80}\ b_{80}[t], \\
&f_{16}'[t] == \mathrm{kf}_f\ b_{16}[t] - \mathrm{kr}_f\ f_{16}[t] - \mathrm{kffg}_{16}\ f_{16}[t]\ a_4[t] + \mathrm{kr}_f g\ f_{20}[t], \\
&\mathrm{Table}[f_i'[t] == \mathrm{kffg}_{i-4}\ f_{i-4}[t]\ a_4[t] - \mathrm{kr}_f g\ f_i[t] - \mathrm{kffg}_i\ f_i[t]\ a_4[t] + \mathrm{kr}_f g\ f_{i+4}[t], \\
&\{i, 20, \max -4, 4\}], f_{\max}'[t] == \mathrm{kffg}_{\max -4}\ f_{\max -4}[t]\ a_4[t] - \mathrm{kr}_f g\ f_{\max}[t], \\
&\mathrm{Table}[b_i[0] == 0, \{i, 4, 80, 4\}], a_1[0] == 53, a_2[0] == 0, a_4[0] == 0, \mathrm{oa}_2[0] == 0, \\
&\mathrm{Table}[f_i[0] == \mathrm{Seed}[[(i-12)/4]], \{i, 16, \max, 4\}]\}], \mathrm{Flatten}[\{a_1, a_2, \mathrm{oa}_2, a_4, \\
&\mathrm{Table}[b_i, \{i, 4, 80, 4\}], \mathrm{Table}[f_i, \{i, 16, \max, 4\}]\}], \{t, 0, 300\}]; \\
&\mathrm{Plot}[\mathrm{Evaluate}[\mathrm{Sum}[i f_i[t], \{i, 16, \max, 4\}]/.\mathrm{soln}] - \mathrm{Sum}[(4i+12) * \mathrm{Seed}[[i]], \{i, 60\}], \\
&\{t, 0, 100\}, \mathrm{PlotRange} \to \{0, \mathrm{All}\}]] \qquad (6.3)
\end{aligned}
$$

Function *NucPol*, Eq. 6.4, was used to plot the population evolution of monomers incorporated into protofibrils to show the aggregation progression, based on nucleated-polymerization model. Meanwhile, the population of protofibrils, *SeedPoP*, on time point *SeedDay* was obtained, to be used as input *Seed* in function *NucPolSeed*. The *NucPolSeed*, Eq 6.5, was used to plot the seeded profile for nucleated-polymerization model.

$$
\begin{aligned}
&A_1 + A_1 \underset{kr_a}{\overset{kfa_1}{\rightleftharpoons}} A_2 \\
&A_2 + A_1 \underset{kr_a}{\overset{kfa_2}{\rightleftharpoons}} A_3 \\
&\vdots \\
&A_{15} + A_1 \underset{kr_{af}}{\overset{kf_{af}}{\rightleftharpoons}} F_{16} \\
&F_{16} + A_1 \underset{kr_f}{\overset{kff_{16}}{\rightleftharpoons}} F_{17} \\
&\vdots \\
&F_{251} + A_1 \underset{kr_f}{\overset{kff_{251}}{\rightleftharpoons}} F_{252}
\end{aligned}
$$

SAMPLE SCHEME FOR NUCLEATED POLYMERIZATION MODEL

NucPol [$\text{kfa}_{list\_}$, $\text{kr}_{a\_}$, $\text{kf}_{af\_}$, $\text{kr}_{af\_}$, $\text{kff}_{list\_}$, $\text{kr}_{f\_}$, $\text{max}_\_$, $\text{SeedDay}_\_$]:=

Module[{soln}, Table[$\text{kfa}_i = \text{kfa}_{list}[[i]]$, $\{i, 1, 15\}$]; Table[$\text{kff}_i = \text{kff}_{list}[[i - 15]]$,

$\{i, 16, \max -1\}$]; soln = NDSolve[Flatten[$\{a_1'[t] == -2\ \text{kfa}_1\ a_1[t]^2 + 2\ \text{kra}\ a_2[t] -$

Sum[$\text{kfa}_i\ a_i[t]\ a_1[t]$, $\{i, 2, 15\}$] + Sum[$\text{kra}\ a_j[t]$, $\{j, 3, 16\}$] − Sum[$\text{kff}_i\ f_i[t]\ a_1[t]$,

$\{i, 16, \max -1\}$] + Sum[$\text{kr}_f\ f_i[t]$, $\{i, 17, \max\}$], Table[$a_i'[t] == \text{kfa}_{i-1}\ a_1[t]\ a_{i-1}[t]-$

$\text{kra}\ a_i[t] - \text{kfa}_i\ a_i[t]\ a_1[t] + \text{kra}\ a_{i+1}[t]$, $\{i, 2, 15\}$], $a_{16}'[t] == \text{kfa}_{15}\ a_1[t]\ a_{15}[t]-$

$\text{kra}\ a_{16}[t] - \text{kf}_{af}\ a_{16}[t] + \text{kr}_{af}\ f_{16}[t]$, $f_{16}'[t] == \text{kf}_{af}\ a_{16}[t] - \text{kr}_{af}\ f_{16}[t]-$

$\text{kff}_{16}\ f_{16}[t]\ a_1[t] + \text{krf}\ f_{17}[t]$, Table[$f_i'[t] == \text{kff}_{i-1}\ a_1[t]\ f_{i-1}[t] - \text{kr}_f\ f_i[t]-$

$\text{kff}_i\ f_i[t]\ a_1[t] + \text{kr}_f\ f_{i+1}[t]$, $\{i, 17, \max -1\}$],

$f_{\max}'[t] == \text{kff}_{\max -1}\ f_{\max -1}[t]\ a_1[t] - \text{kr}_f\ f_{\max}[t], a_1[0] == 53$,

Table[$a_i[0] == 0$, $\{i, 2, 16\}$], Table[$f_i[0] == 0$, $\{i, 16, \max\}$]}],

Flatten[{Table[a_i, $\{i, 1, 16\}$], Table[f_i, $\{i, 16, \max\}$]}], $\{t, 0, 300\}$];

SeedPop = Flatten[Evaluate[Table[f_i[SeedDay], $\{i, 16, \max\}$]/.soln]];

Plot[Evaluate[Sum[$i\ f_i[t]$, $\{i, 16, \max\}$]/.soln], $\{t, 0, 100\}$, PlotRange → {0, All}]] (6.4)

NucPolSeed [$\text{kfa}_{list\_}$, $\text{kra}_\_$, $\text{kff}_{list\_}$, $\text{krf}_\_$, $\text{max}_\_$, $\text{Seed}_\_$]:=Module[{soln},

Table[$\text{kfa}_i = \text{kfa}_{list}[[i]]$, $\{i, 1, 15\}$]; Table[$\text{kff}_i = \text{kff}_{list}[[i - 15]]$, $\{i, 16, \max -1\}$];

soln = NDSolve[Flatten[$\{a_1'[t] == -2\ \text{kfa}_1\ a_1[t]^2 + 2\ \text{kra}\ a_2[t]-$

Sum[$\text{kfa}_i\ a_i[t]\ a_1[t]$, $\{i, 2, 15\}$] + Sum[$\text{kra}\ a_j[t]$, $\{j, 3, 16\}$] − Sum[$\text{kff}_i\ f_i[t]\ a_1[t]$,

$\{i, 16, \max -1\}$] + Sum[$\text{kr}_f\ f_i[t]$, $\{i, 17, \max\}$], Table[$a_i'[t] == \text{kfa}_{i-1}\ a_1[t]\ a_{i-1}[t]-$

$\text{kra}\ a_i[t] - \text{kfa}_i\ a_i[t]\ a_1[t] + \text{kra}\ a_{i+1}[t]$, $\{i, 2, 15\}$], $a_{16}'[t] == \text{kfa}_{15}\ a_1[t]\ a_{15}[t] - \text{kra}\ a_{16}[t]$

$- \text{kf}_{af}\ a_{16}[t] + \text{kr}_{af}\ f_{16}[t]$, $f_{16}'[t] == \text{kf}_{af}\ a_{16}[t] - \text{kr}_{af}\ f_{16}[t]-$

$\text{kff}_{16}\ f_{16}[t]\ a_1[t] + \text{krf}\ f_{17}[t]$, Table[$f_i'[t] == \text{kff}_{i-1}\ a_1[t]\ f_{i-1}[t] - \text{kr}_f\ f_i[t]-$

$$\text{kff}_i\ f_i[t]\ a_1[t] + \text{kr}_f\ f_{i+1}[t], \{i, 17, \max -1\}], f'_{\max}[t] == \text{kff}_{\max -1}\ f_{\max -1}[t]\ a_1[t] -$$
$$\text{kr}_f\ f_{\max}[t], a_1[0] == 53, \text{Table}[f_i[0] == \text{Seed}[[i - 15]], \{i, 16, \max\}]\}],$$
$$\text{Flatten}[\{\text{Table}[a_i, \{i, 1, 15\}], \text{Table}[f_i, \{i, 16, \max\}]\}], \{t, 0, 300\}];$$
$$\text{Plot}[\text{Evaluate}[\text{Sum}[i\ f_i[t], \{i, 16, \max\}]/.\text{soln}] - \text{Sum}[(i + 15) * \text{Seed}[[i]], \{i, \max -15\}],$$
$$\{t, 0, 100\}, \text{PlotRange} \to \{0, \text{All}\}]] \tag{6.5}$$

The following functions were used to plot the amyloidogenic free-energy landscape presented in Chapter 2. The free-energy of monomer was arbitrarily assigned to 0 kJ/mol. The rest of energetics were calculated relatively based on the simulated rate coefficients in Chapter 2. The parameter *SeaLevel* is an arbitrary value assigned for the visualization.

a[y_]:=Switch [$y, 1, 0, 1.5, 64.036, 2, -2.032$, _, SeaLevel];

aob[y_]:=If [$y == 2, 57.374$, SeaLevel];

ao[y_]:=Switch [$y, 2, -6.472, 3, 52.934, 4, -13.134$, _, SeaLevel];

abb[y_]:=If [$y == 4, 48.961$, SeaLevel];

b[y_]:=Switch [$y, 4, -6.181, 6, 55.914, 8, -3.475, 10, 58.620, 12, -0.804, 14, 61.291,$
$16, 1.816, 18, 63.911, 20, 4.385, 22, 66.480, 24, 6.908, 26, 69.003, 28, 9.387, 30,$
$71.482, 32, 11.826, 34, 73.921, 36, 14.228, 38, 76.323, 40, 16.596$, _, SeaLevel];

bfb[y_]:=If [$y == 16, 80.286$, SeaLevel];

f[y_]:=Switch [$y, 16, -8.156, 18, 44.156, 20, -10.212, 22, 42.010, 24, -12.288, 26,$
$40.024, 28, -14.343, 30, 37.969, 32, -16.364, 34, 35.948, 36, -18.345, 38, 33.967,$
$40, -20.286, 42, 32.026, 44, -22.189, 46, 30.123, 48, -24.054, 50, 28.258, 52,$
$-25.884, 54, 26.428, 56, -27.682, 58, 24.630, 60, -29.448, 62, 22.864, 64, -31.186,$
$66, 21.127, 68, -32.896, 70, 19.416, 72, -36.241$, _, SeaLevel];

$$\text{yvals} = \text{Join}[\text{Table}[y, \{y, \{0.5, 1, 1.5, 2, 3\}\}], \text{Table}[j, \{j, 4, 62, 2\}]]; \text{SeaLevel} = 120;$$
$$\text{xvals} = \text{Table}[x, \{x, 0.5, 4.5, 0.5\}]; \tag{6.6}$$

$$\begin{aligned}&\text{Landscape} = \text{Table}[\text{Which}[x == 1, a[\text{yvals}[[\text{ny}]]], x == 1.5, \text{aob}[\text{yvals}[[\text{ny}]]],\\ &x == 2, \text{ao}[\text{yvals}[[\text{ny}]]], x == 2.5, \text{abb}[\text{yvals}[[\text{ny}]]], x == 3, b[\text{yvals}[[\text{ny}]]], x == 3.5,\\ &\text{bfb}[\text{yvals}[[\text{ny}]]], x == 4, f[\text{yvals}[[\text{ny}]]], \text{Or}\ [x == 4.5, x == 0.5], \text{SeaLevel}],\\ &\{x, \text{Reverse}[\text{xvals}]\}, \{\text{ny}, 1, 35\}]\end{aligned} \tag{6.7}$$

$$\begin{aligned}\text{ColorSchemeEng} = (&\text{Blend}[\{\{-36.2, \text{Black}\}, \{-9, \text{Blue}\}, \{-5, \text{Darker}[\text{Green}, 0.5]\},\\ &\{5, \text{Darker}[\text{Yellow}, 0.2]\}, \{10, \text{Yellow}\}, \{30, \text{Brown}\},\\ &\{80, \text{Lighter}[\text{Brown}, 1/2]\}\}, \#1]\&)\end{aligned} \tag{6.8}$$

$$\begin{aligned}&\text{EngLandscape} =\\ &\text{ListPlot3D}[\text{Landscape}, \text{Mesh} \to \{\{-40, -20, -10, 0, 20, 40, 60, 80, 100\}\},\\ &\text{MeshStyle} \to \{\text{Thin}\}, \text{MeshFunctions} \to \{\#3\&\}, \text{ColorFunctionScaling} \to \text{False},\\ &\text{ColorFunction} \to \text{Function}[\{x, y, z\}, \text{ColorSchemeEng}[z]], \text{SphericalRegion} \to \text{False},\\ &\text{BoxRatios} \to \{24, 12, 1.5\}, \text{ClippingStyle} \to \text{None}, \text{PlotRange} \to \{\text{All}, \text{All}, \{\text{All}, 100\}\},\\ &\text{ImageSize} \to 460, \text{Axes} \to \{\text{True}, \text{True}, \text{False}\}, \text{ViewPoint} \to \{-0.86, -2.1, 2.5\},\\ &\text{ViewVertical} \to \{0, 0, 1\}, \text{InterpolationOrder} \to 5, \text{Axes} \to \text{True}, \text{PlotStyle} \to \text{Opacity}[1],\\ &\text{Boxed} \to \text{True}, \text{FaceGrids} \to \{\{\{0, 0, -1\}, \{\text{Table}[n, \{n, 2, 40, 2\}], \text{Table}[n, \{n, 2, 8, 2\}]\}\}\}\\ &\text{Ticks} \to \{\text{Table}[\{n, \text{If}[n < 6, n/2, (n/2 - 2) * 4]\}, \{n, 2, 40, 2\}],\\ &\{\{8, A\}, \{6, \text{Ao}\}, \{4, B\}, \{2, F\}\}\}]\end{aligned} \tag{6.9}$$

Curriculum Vita

Xianglan He

Education

2012 Ph.D. Chemistry, Rutgers, The State University of New Jersey, Piscataway, NJ

2003 B.S. Chemistry, Lanzhou University, Lanzhou, China

Employment

2004-2011 Teaching/Graduate Assistant, Department of Chemistry and Chemical Biology, Rutgers, The State University of New Jersey, Piscataway, NJ

Publications

2012 **He, Xianglan**; Talaga, David. Mechanism of characteristic thioflavin T fluorescence upon binding to α-Synuclein amyloid fibrils. *in preparation*

2011 Pronchik, Jeremy; **He, Xianglan**; Giurleo, Jason. In vitro formation of amyloid from α-Synuclein is dominated by reactions at hydrophobic interfaces. *Journal of the American Chemical Society* (2010) 132(28), 9797-9803.

2010 **He, Xianglan**; Giurleo, Jason.; Talaga, David. Role of small oligomers on the amyloidogenic free-energy landscape. *Journal of Molecular Biology* (2010) 395(1), 134-154

2008 Giurleo, Jason; **He, Xianglan**; Talaga, David. β-Lactoglobulin assembles into amyloid through sequential aggregated intermediates. *Journal of Molecular Biology* (2008), 381(5), 1332-1348